2020

# A Search For Multi-Charged Heavy Stable Charged Particles in Run 2 Data from the Large Hadron Collider

Thomas Jacob Murphy

THE FLORIDA STATE UNIVERSITY
COLLEGE OF ARTS AND SCIENCES

# A SEARCH FOR MULTI-CHARGED HEAVY STABLE CHARGED PARTICLES IN RUN TWO DATA FROM THE LARGE HADRON COLLIDER

By

THOMAS JACOB MURPHY

A Thesis submitted to the
Department of Physics
in partial fulfillment of the requirements for graduation with
Honors in the Major

Degree Awarded:
Spring, 2020

The members of the Defense Committee approve the thesis of Thomas Jacob Murphy Defended on April 20th, 2020

Dr. Todd Adams
Thesis Director

Dr. Jerry Magnan
Outside Committee Member

Dr. Simon Capstick
Committee Member

# Contents

# List of Figures

# List of Tables

## Abstract

Several models of Beyond the Standard Model physics include the existence of particles characterized by being massive, long lived, and have a charge, Q, greater than that of an electron $e$. This search utilizes data produced from the Compact Muon Solenoid at the Large Hadron Collider, in Run 2 with $\sqrt{s}$ =13 TeV. The signal of these particles is identified by their slow moving, highly ionizing signature. Time of flight and ionization energy loss measurements are made by the muon system and inner tracker respectively. This search aims to study expected cross section limits for 2e, stop quarks, gluinos, GMSB stau lepton production, and pair production of stau leptons.

# Acknowledgement

I would like to thank Dr. Todd Adams for the countless hours of instruction and guidance for nearly two years on matters in high energy physics to my continuing my education in graduate school. I could not have asked for a better advisor.

An additional thanks to of my committee members, Drs Simon Capstick and Jerry Magnan, who have both helped me mature as a young scientist and explore the world of particle physics and applied mathematics.

Finally, a special thank you goes out to all the other professors that have stimulated my interest in physics and encouraged me to pursue a career in physics.

# 1 Introduction

Throughout the entirety of our scientific endeavors as humans, we have been motivated by a desire to understand the smallest constituents of the universe. The first records of such discussions go back as far as 400 BCE, with the coinage of the term "atomos" meaning indivisible [1]. A more accurate picture of the universe is one constructed of particles that interact to form complicated structures. The mathematical framework for such particles is called the Standard Model (SM) of particle physics.

The SM has passed rigorous testing from numerous experiments from the Large Hadron Collider (LHC), providing an experimental foundation that can support the theoretical calculations. Despite the success of the model, it is by no means a perfect theory. In fact, the standard model can only explain a small fraction of the energy we see in the universe. The rest is composed of dark energy and dark matter. Even before the advent of these discoveries, we required an extension to the current theory to explain the other shortcomings of the SM. Theories that extend the SM are collectively called Beyond the Standard Model (BSM) theories. Some of these models predict the existence of new particles, like multi-Charged Heavy Stable Charged Particles (MHSCPs) and Heavy Stable Charged Particles (HSCPs). Throughout the rest of the paper I will discuss my search for MHSCPs.

# 2 Beyond The Standard Model

To understand the physics that might extend the standard model, we must first discuss the standard model.

The standard model is a theoretical framework that describes the world from a particle physics perspective. It describes the constituents of all matter that we interact with day to day. This model divides into two different particle classifications, those with integer spins (i.e. 0,1,2,3...) and those with half integer spins (1/2, 3/2, 5/2...). Particles with half integer spins are called fermions. Further, we can divide the group of fermions in the SM into leptons and quarks. These particles are the constituents of matter. Particles with integer spins are called bosons. It should be noted that the SM only includes vector and scalar bosons. Further it only includes spinor fermions. Fig. 1 is a pictorial representation of the standard model [2].

## 2.1 Quantum Numbers

When considering the interactions between ordinary matter we must also consider the various quantum numbers that are associated with each particle. For example, electric charge and color (which generically, is the quantum number associated with the strong charge) need to be considered when investigating the interactions of quarks. In addition to the normal matter that we see from day to day, there also exists anti-matter particles, which have the opposite quantum numbers as their counterparts.

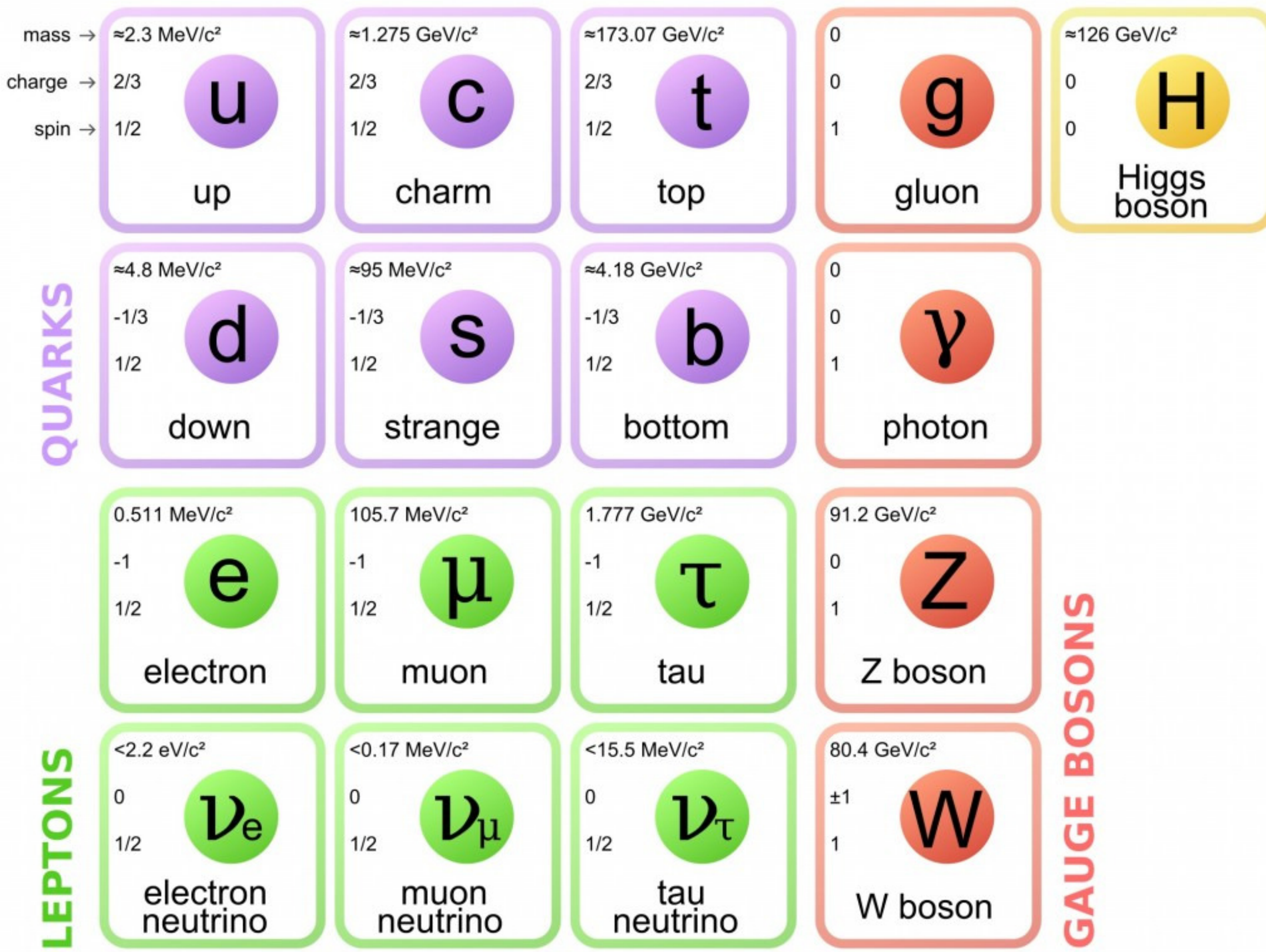


Figure 1: A pictorial representation of the Standard Model.

The conservation of these quantum numbers forms the foundation to understanding particle physics. Furthermore, it allows us to understand specific properties of particles such as stability. For example, the stability of the electron can be described as a consequence of the conservation of electric charge, while the decay of the muon can be predicted by the conservation of lepton and electric charges. But we also require that the decays satisfy the conservation of relativistic (four) momentum.

## 2.2 HSCPs and mHSCPs

If we are to consider the idea of quantum numbers beyond what we know now, it might permit the existence of new particles beyond the standard model. These new particles then have the ability to fill in some of the gaps within the SM. One such number that could exist is R-Parity [3], defined below:

$$R_{parity} = (-1)^{3B-L+2S} \tag{1}$$

where $B$ is the baryon number, $L$ is the lepton number, and $S$ is the spin of the particle. The theory of supersymmetry (SUSY) is what places the constraint on the R-parity. One consequence of this equation is it makes the SUSY partner particle have odd R-parity and even R-parity for the SM particles. When R-parity is conserved, one important consequence is that the lightest supersymmetrical particle is stable, commonly refereed to as the Lightest SUSY particle, or LSP. This example shows how extensions of the SM may address its shortcomings as the LSP might be a candidate to explain dark matter.

Muons traveling at roughly the speed of light take more than twenty nanoseconds to reach the system that specializes in the tracking of the muons. As a result of the slower velocity of HSCPs, the sensitivity of the analysis requires HSCPs to have lifetimes longer than the time it takes for a muon to reach the detectors. As such, this search is most sensitive to particles with lifetimes on the order of magnitude of milliseconds to microseconds. One such theoretical explanation for longer lived HSCPs are R-Hadrons. Simply put, R-hadrons are bound states with SUSY particles within them. They are held together by the strong force [4].

There exist different types of HSCPs. In this paper, the analysis will focus on two different types of HSCPs, the first of which hadron-like HSCPs. These particles interact via the strong force. Due to their colored nature, they will hadronize, creating mesons, baryons, or glueballs. These are the aforementioned R-hadrons. Such particles are made of SM partons and one heavy exotic parton. In most of the models that describe how these particles interact with detectors, it is assumed that the exotic constituent is merely a spectator, as such it can serve as a reservoir for kinetic energy. However, in comparison to the total energy of the interactions with the detectors, the kinetic energy is relatively small. As such, we predict that the energy deposited into the detector as it passes through is small, which means that R-hadrons are highly penetrating. These particles will have a similar signature to muons moving through the detector. However due to their large mass, HSCPs will be moving much slower than their standard model counterparts.

In addition to hadron-like HSCPs, we also have lepton-like HSCPs. These particles interact via electromagnetic and weak forces, but not the strong interaction. One such example are Q-balls [5]. Q-balls can be built out of a variety of different supersymmetric quarks, supersymmetric leptons, and the Higgs Scalar. It is thought that the least massive of these particles could be observed by a detector several meters in size (like the CMS detector).

# 3 The Experiment

This search for HSCPs utilized data from the Compact Muon Solenoid (CMS) detector of the LHC. The LHC consists of two counter rotating beams of protons. These beams are then directed to intersection points, at which the beams interact, producing particles that then travel through the detectors. Recording the kinetic energy, momentum, and position of these particles as they traverse the different parts of the detector allows us to reconstruct the interactions and identify the different products.

## 3.1 The Large Hadron Collider

The data used in this search recorded during Run 2 data at the LHC [6]. These data were produced with center of mass energies of 13 TeV. The beams contain bunches of particles on the order of 100 billion protons. Each beam contains up to 2244 of these bunches, and collides them every 25 nanoseconds.

The LHC utilizes a combination of large superconducting magnets and more traditional electromagnets, to steer the beams in a ring that is 27 km in circumference. The superconducting magnets are cooled using liquid helium to 1.9 K. Dipole magnets are used to keep the beam circulating in the ring and quadrupole magnets are used to focus the beam [7].

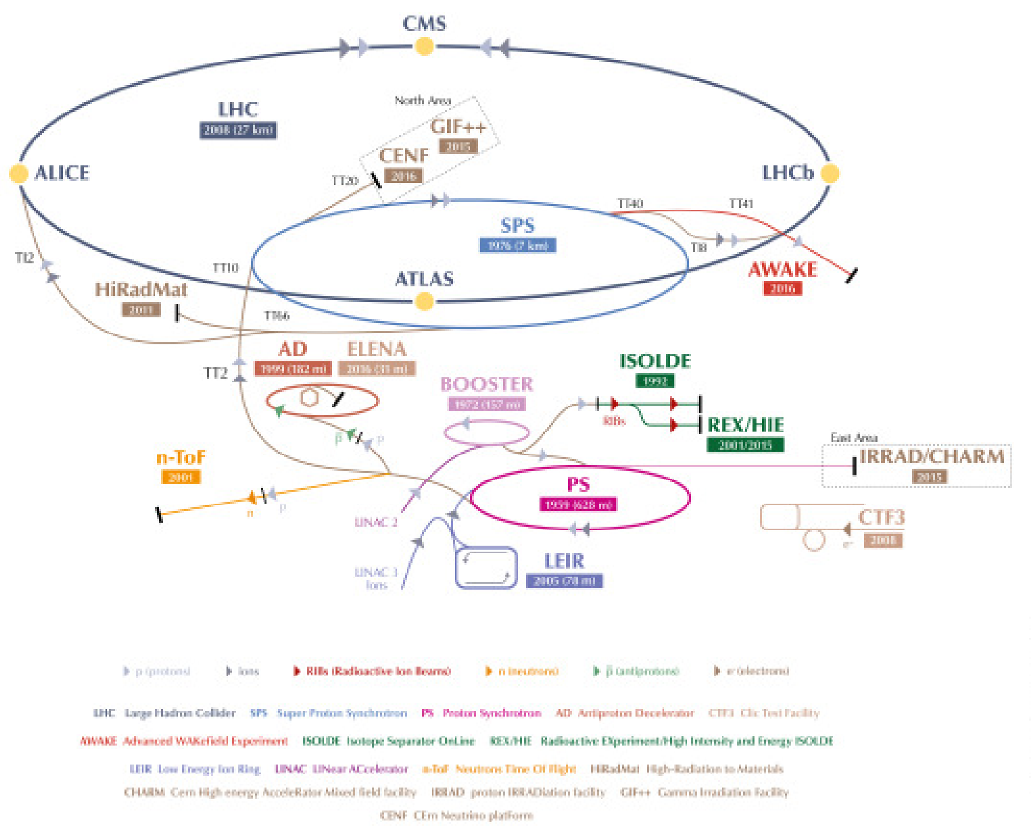


Figure 2: A detailed view of the CERN accelerator complex [8].

Figure 2 depicts the layout of the CERN accelerator complex, which is more complicated than a single ring that accelerates the protons.. As you can see the image of a single ring that accelerates the proton beam is a bit naive. However, for the purposes of this paper we only are concerned with region in which the center of mass energy is 13 TeV (this energy level is found only in the larger ring). A more concise depiction of the main ring is shown in Fig. 3 [9].

## 3.2 The Compact Muon Solenoid Detector

The CMS detector is 21 meters long by 15 meters high by 15 meters wide and made of several layers, each of which provide a different method for the study of the collisions. The diversity of which, allows the CMS experiment to study a large number of different particles. The CMS detector has four different parts: the tracker is designed to measure the momentum of the particles whilst interacting with them as little as possible; the electromagnetic calorimeter is meant to stop electrons and photons and measure their energies; the hadron calorimeter accomplishes a similar task, but for hadrons instead of electrons and photons. These three components are all located inside a large solenoid magnet that bends the paths of any charged particle. The muon detector is only penetrated by muons and neutrinos. However the muon detector is not sensitive to neutrinos because they pass through the entire detector undetected, but are rather inferred by reconstructing the missing momentum in the collisions.

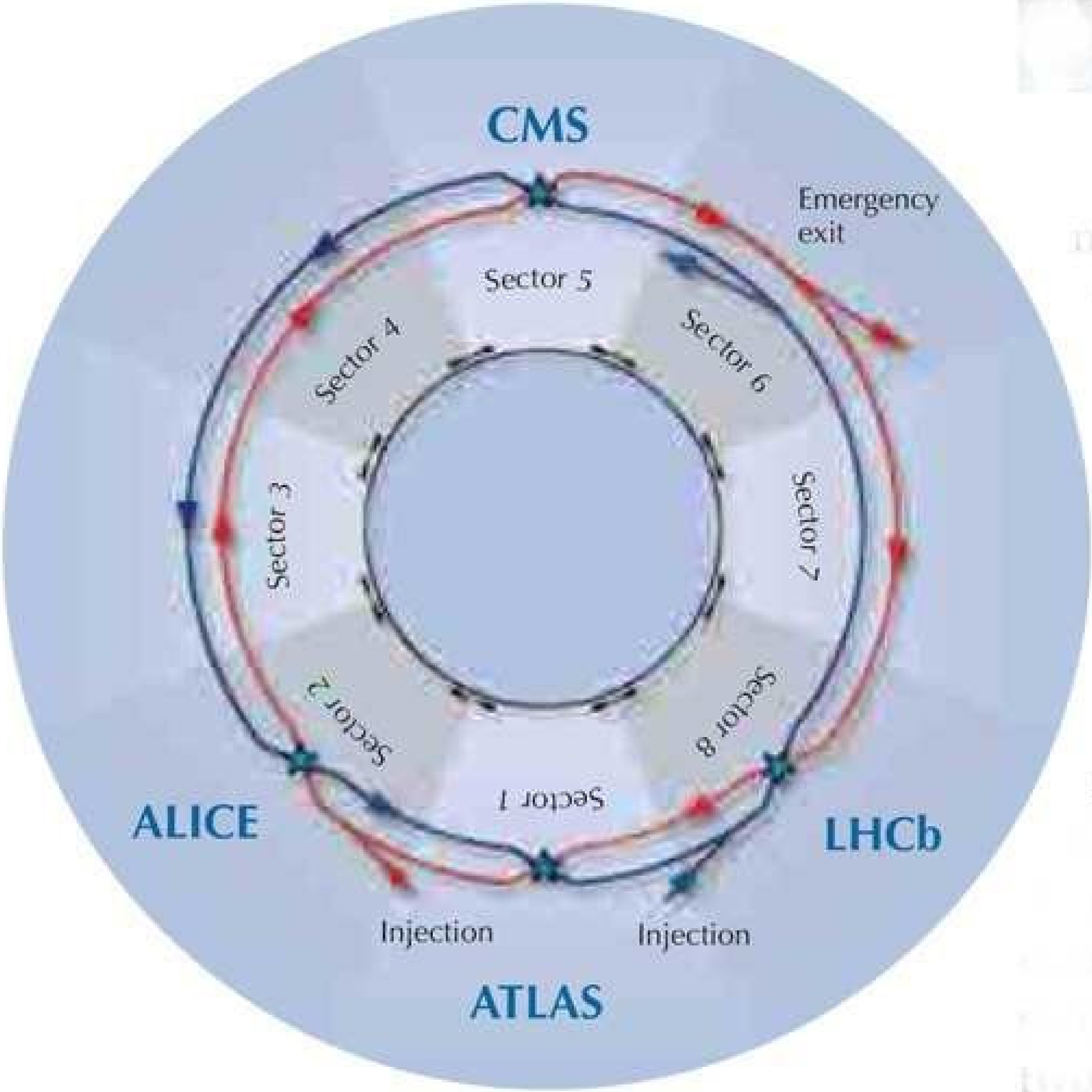


Figure 3: A simplified view of the LHC main ring

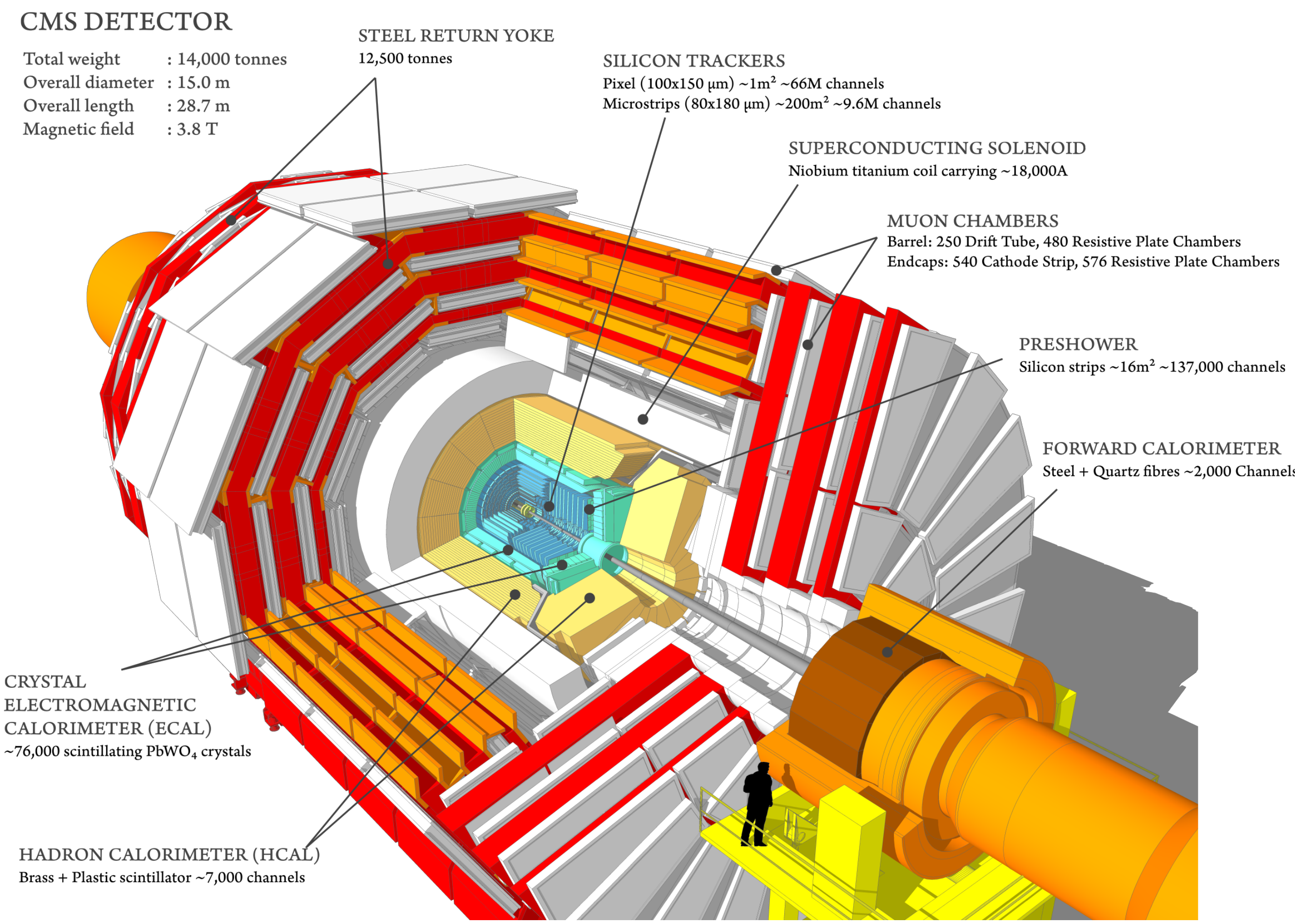


Figure 4: Diagram of the Compact Muon Solenoid Detector [10].

### 3.2.1 Coordinate System

The CMS experiment uses a coordinate system relevant to the nature of the interactions.

To gain an intuition of the physical interpretation of the coordinate system, we must first orient the Cartesian coordinate system on the experimental setup. So we let the X axis point from the nominal interaction point to the center of the main LHC ring. We construct the Y axis from a vector normal to the plane in which the LHC ring lies which points away from the earth. Consequently, the Z axis lies in the beam line, and points in the counter clockwise direction.

Now we define the azimuthal angle $\phi$, as the angle in the XY plane, formed from the x axis to the radial component r, projected into the plane. The radial component describes the distance from the Z axis. The angle $\theta$ is measured from the positive Z axis.

Now that a quantitative model for the coordinate system has been established, a more precise definition for the pseudorapidity, $\eta$, is required [11]:

$$\eta = -\ln\left(\tan\frac{\theta}{2}\right)$$

Pseudorapidity, $\eta$, is a measure of the angle from the beam line, and is designed in such a way that it is invariant under a Lorentz boost along the axis parallel to the beam. Further, equal cuts in $\eta$ correspond to a linear distribution of events that pass through a region of the detector [11].

### 3.2.2 The Tracker Detector

Particles produced in the collisions first pass through the tracker. The tracker must be accurate yet lightweight as to not cause scattering of the particles. In addition, the components need to be made out of something that can resist the intense radiation produced from the collisions. One solution, that is currently in use, is the use of an array of small

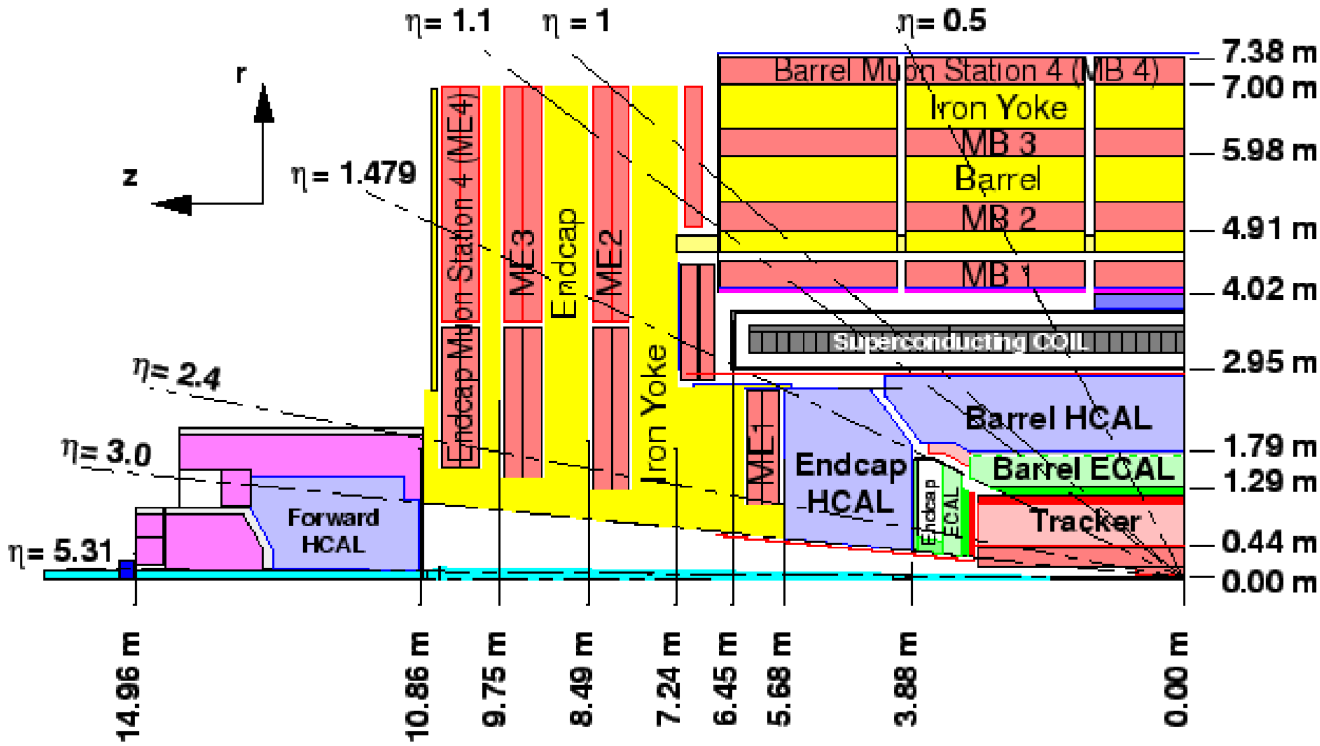


Figure 5: Diagram of the Compact Muon Solenoid Detector as seen from a longitudinal perspective. This diagram includes a visualization of the coordinate system. [12]

silicon sensors that each provide a measurement, which can reveal the paths and momentums of the various charged particles coming out of the collisions.

Silicon is very suitable for this stage of the tracker as it responds very quickly to the particles. As a result, we are able to keep up with the bombardment of particles coming from the proton collisions. As a charged particle penetrates one of the sensors, it knocks electrons from the atoms. Within the applied electric field these electrons move, giving a small electric pulse. This pulse is then amplified using Analog Pipeline Voltage (APV25) chips.

The Tracker is composed of two different parts. The inner tracker is closer to the beam line and is made out of silicon pixels. These pixels are small (100 by 150 micrometers) in an attempt to reduce the amount of radiation exposure of each element, while also providing a greater resolution to the tracker. Due to the even more dramatic amounts of radiation associated with being located closer to the interaction site, the inner tracker can be extracted and have pixels replaced when they become too damaged. The outer tracker is made of strip trackers that function in much of the same way.

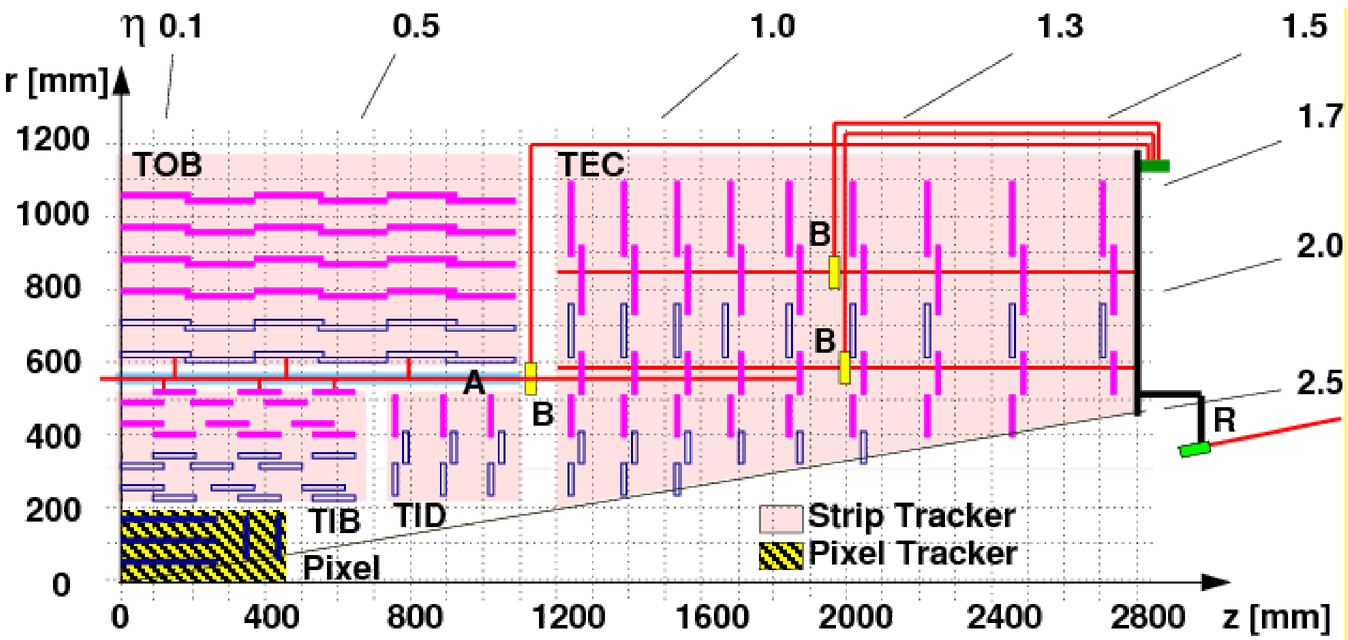


Figure 6: Schematic view of one quarter of the silicon tracker in the r-z plane. The positions of the pixel modules are indicated within the hatched area. At larger radii within the lightly shaded areas, solid rectangles represent single strip modules, while hollow rectangles indicate pairs of strip modules mounted back-to-back with a relative stereo angle. [13]

The inner tracker contains about 65 million sensors. These pixels are arranged in four different concentric cylinders around the beam line. This array of sensors allows us to identify a charged particle at multiple positions as it passes through the detector, allowing us to deduce the trajectory of the particle.

After particles pass through the pixel layers of the tracker, they then travel through ten layers of silicon strip sensors that extend to a distance of one hundred thirty centimeters from the beam line. Within the outer tracker, there are three different sub-systems: The Tracker Inner Barrel (TIB), the Tracker Outer Barrel (TOB), and the Tracker End Caps (TEC). In the barrel sections, the strip detectors form concentric cylinders with each individual strip parallel to the beam line. This allows us to detect particles in the plane perpendicular to the direction of the strip. In this case it is the $r\phi$ direction. Similarly, on the end caps the strips are orientated radially giving us coverage in the $z\phi$ direction. Thus we can combine the data of the barrel and the end caps to acquire the position of the particles. The different sub-sections can be seen in Figs. 6 and 7.

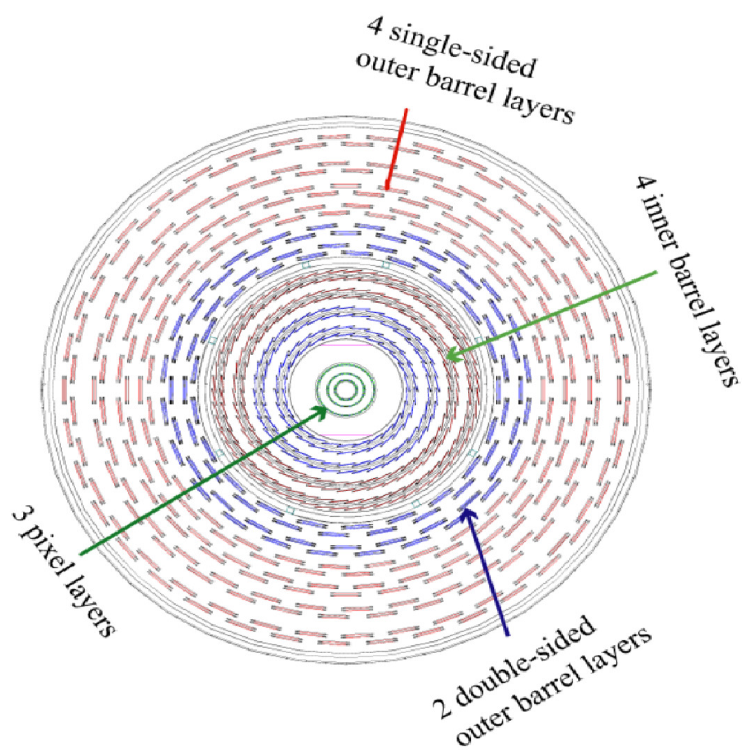


Figure 7: The tracker layers as seen from a plane perpendicular to the beam line [14]

When searching for HSCPs, the tracker provides us with vital information about the energy lost to ionization. As the particles pass through the silicon they create electron hole pairs, the excitation of electrons that produces a current that we can then measure (see The Tracker Detector). This current is then sent to the Analog to Digital Converter (ADC) where the current is converted to ADC counts. Due to the 8 bit nature of the the ADC forces it to take a value between 0 and 255, this number allows the experiment to reduce the amount of space used to store the data. As a reference the background noise in the detector ranges from about 4.5 to 8.5 ADC counts. A minimum ionizing particle will have an energy loss of approximately 3 MeV per centimeter, corresponding to 300 ADC counts per millimeter. The nonlinearity in the relationship between the deposited energy and the ADC counts serves as a limit to the effective measurable range of energies [15]. In addition, the last two bits of the ADC counts serves as an overflow. Bit 254 is reserved for energy loss between 254 and 1024 counts, while any count greater than that will be stored in the 255th bit. This is known as the saturation effect [16]

When a particle passes through one of the silicon sensors it will deposit most of its energy in either one or two of the strips on the sensors. The latter case happens when the particle travels through the edge of one of the detectors. During offline reconstruction, we group the strips into clusters using the strips with a signal to noise ratio greater than 3 as the seeds, then the neighboring strips with a signal to noise ratio greater than 2 are included in the cluster.

Energy deposited in the seed strips will tend to be shared over the adjacent strips as a result of crosstalk effects in the detectors. Experimental evidence suggests that the sharing of this signal occurs by a factor of $10^{-n}$, where n refers to the number of detectors from the seed detector. For example, if n = 1 that is referring to an adjacent detector [17]. To avoid the conflating fluctuations in the background with a viable SM or HSCP signature; the analysis requires that the total signal size of the cluster must be 5 times larger than the square root of the Root Mean Squared (RMS) noise squared of the constituent strips in the given cluster.

Once the cluster passes all of the criteria, we can define some of the characteristics of the particle. The position of the cluster is calculated to be the centroid of the ADC counts in the different strips. The number of strips in the cluster defines the cluster size. The total energy loss, $\frac{\Delta E}{\Delta x}$ is defined by the cluster charge ($\Delta E$) divided by the path length ($\Delta x$). Where the path length, $\Delta x$ is defined by $\Delta x = L/\cos\theta$, while $L$, describes the thickness of the module, and $\theta$ is the angle between the normal of the given strip module and the given track [17], more information on the tracker detector can be found in Refs. [18] and [19].

### 3.2.3 Electromagnetic Calorimeter (ECAL)

The Electromagnetic Calorimeter is composed of a crystal-based scintillating calorimeter, which forms a barrel section (EB) and two end caps (EE) that enclose the tracker. The coverage of the pseudorapidity extends to $|\eta| < 2.5$, with the primary function of measuring the energy of electrons, positrons, and photons. The ECAL uses a total of 68524 lead tungstate ($PbWO_4$) crystals as the scintillators [18]. Lead tungstate crystals were chosen to ensure compactness of the detector with a radiation length of 0.85 centimeters and have a Moliere radius of about 2.19 centimeters [18]. These precautions provide a greater resistance to the radiation commensurate with the nature of experiment, allowing the detector to have a longer lifetime. The ECAL, the tracker system, and the solenoid magnet are used to reconstruct the momentum of charged particles, with a higher sensitivity to electrons and photons than other SM particles [19].

### 3.2.4 Hadron Calorimeter (HCAL)

The HCAL is meant to measure the energy and direction of hadrons. In the context of the search for exotic particles it can be used to identify the missing transverse energy [20]. The HCAL is a sampling calorimeter consisting of alternating layers of brass and/or steel absorber, and plastic scintillators.

The HCAL consists of four different components, the barrel (HB), the endcap (HE), the outer (HO), and the forward (HF) calorimeters. These components result in a coverage of $|\eta| < 5.3$ [20]. Due to the relative frequency at which hadrons breach the confines of the HCAL the solenoid itself and the outer segment of the HCAL doubles as an absorber.

### 3.2.5 Muon System

Unlike the rest of the detector, the muon system is not surrounded by the solenoid. However, there is still a magnetic field that permeates the system and is retained by the utilization of iron plates. As such, it is possible to make a time of flight measurement for particles such as muons or HSCPs in the muon system.

This is crucial to the analysis, as muons, like HSCPs are minimal ionizing and will likely pass through the ECAL and HCAL. While the momentum signatures of muons and HSCPs are not readily apparent, their time of flight signatures are distinct. As such, making the momentum measurement in the muon system is a vital step in this analysis [21].

The muon system records the time at which the particle arrives as well as the position of the particles by using data collected by the Drift Tubes. As depicted in Fig. 8, the muon system is made of three gaseous detector components: the Drift Tube chambers (DT), Cathode Strip Chambers (CSC), and the Resistive Plate Chambers (RPC) [21]. While the RPC and CSC are important in the context of the CMS experiment as a whole, their importance is overshadowed by the role the DT plays in this analysis. When compared to muons which move at nearly the speed of light, HSCPs move relatively slowly. As such, we would expect the arrival times for HSCPs to be after that of the muons. Thus the analysis can use the time of flight information to assist in the identification of HSCP candidates.

The drift tube system is located within the barrel of the detector, where neutron induced background is low, the return magnetic field is relatively uniform, and the muon rates are low. Each tube is 4 centimeters wide, and contains a stretched wire within a gaseous volume. A cross sectional diagram of a drift tube is depicted below. To avoid the edge effects and increase the accuracy of the drift tubes, they are staggered such that the edge of one tube is directly above the middle of another.

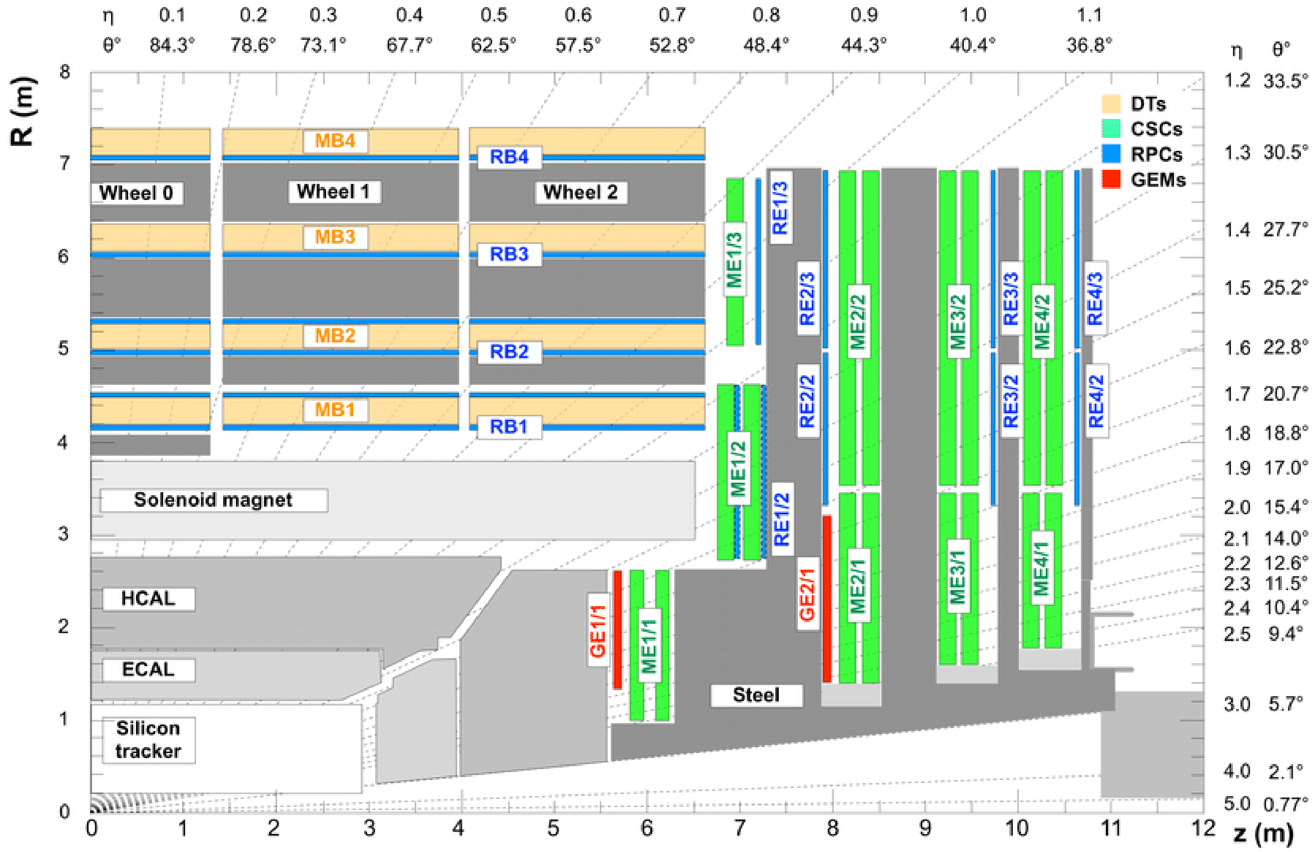


Figure 8: Quadrant of the CMS detector showing the present muon system including RPCs, DTs and CSCs. The proposed locations for the GEM detectors in the inner endcap stations are indicated by the red boxes [22].

As charged particles traverse the gaseous medium of the drift tubes, they ionize the confined gas, knocking electrons off their associated atoms. These electrons are then accelerated by an electric field to a positively charged wire within the tube. We can then reconstruct the two-dimensional position by combing signal amplitudes from multiple tube wires. In addition, information regarding the arrival time can be found if the drift velocity of electrons in the gas is known. Thus, we are able to determine both the trajectory and the time of flight within the muon system.

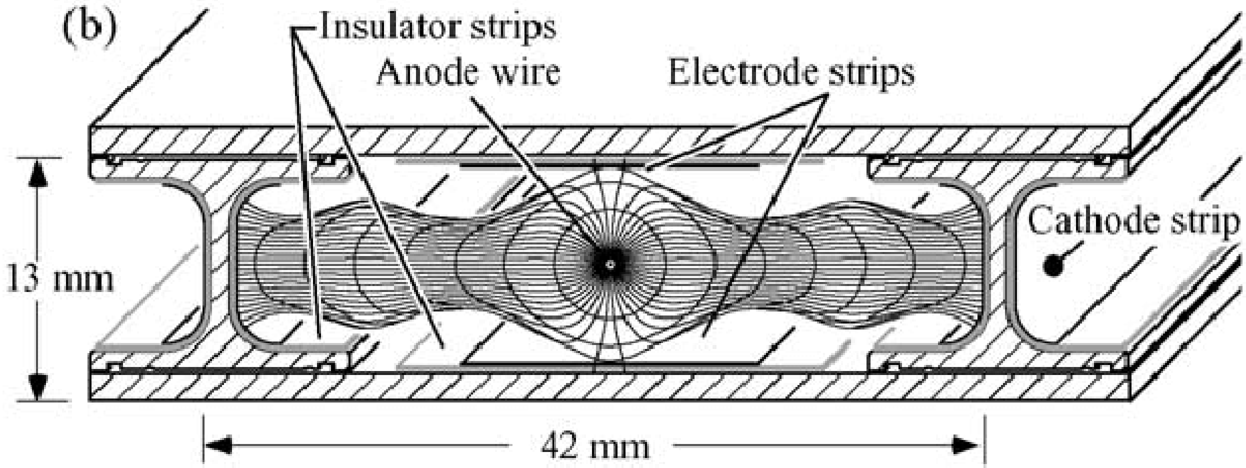


Figure 9: Cross section of a drift tube used in the muon system of the CMS detector [23].

# 4 Search Variables

In this search for HSCPs we use time of flight and ionization energy deposition information to find HSCP candidates. This analysis utilizes a discriminator to distinguish these candidates from SM signals.

## 4.1 Momentum

The reconstruction code for the CMS experiment calculates momentum using the curvature of the particles as it travels through the detector. The reconstruction code assumes that the particle is singly charged (that is to say $|Q| = 1e$). The method to determine momentum can be seen below:

$$\vec{F}_{EM} = q(\vec{E} + \vec{v} \times \vec{B}) \tag{2}$$

$$|\vec{F}_{EM}| = qvB\sin(\theta) \tag{3}$$

$$|\vec{F}_{EM}| = qvB \tag{4}$$

where $\vec{F}_{EM}$ is the electro-magnetic force acting on the particles as they pass through the detector, $q$ is the charge of the particle ($Q$ as described before), $\vec{E}$ is the electric field inside the detector which is zero, $\vec{v}$ is the velocity of the particle, $\vec{B}$ is the magnetic field inside the detector, and $\theta$ is the angle between the magnetic field and the velocity of the particle.

Setting Eq. 4 equal to the centripetal force will give us an expression for the momentum of the particle.

$$qvB = m\frac{v^2}{r} \tag{5}$$

$$qB = \frac{p}{r} \tag{6}$$

$$p = qrB \tag{7}$$

where $r$ is radius of the trajectory and $p$ is the magnitude of the momentum. As you can see from Eq. 7 the momentum of the particle scales linearly with the charge therefore we expect to see a momentum that is multiplied by a factor of the inverse of the charge when analyzing the momenta of multiply charged particles.

## 4.2 The Discriminator

As mentioned before we use a discriminator to differentiate between HSCP signatures and SM background using energy loss in the silicon tracker. A discriminator is a way of measuring the difference between empirical and observed probability distribution functions (PDF). In this search, the PDF of the minimum ionizing particle (MIP) is assumed to be known. More specifically, in this search the discriminator serves as a way to compare the set of $\frac{\Delta E}{\Delta x}$ measurements to the MIP PDF.

It becomes advantageous to have this variable be sensitive to particles with ionization much higher than that of a minimally ionizing particle. Moreover, this measurement should be resistant to the effects of saturation (see The Tracker Detector). In this search our primary discriminator is the Asymmetric Smirnov-Cramer-Von Mises ($I_{as}$), which is modification to the Smirnov-Cramer-Von Mises ($I_h$). The asymmetric version is important because it eliminates the sensitivity to deviations from the MIP hypothesis [24] [25] [26]. Eliminating that sensitivity is especially important in the search for mHSCPs. $I_{as}$ is defined as follows:

$$I_{as} = \frac{3}{N} \times \left( \frac{1}{12N} + \sum_{j=1}^{N} \left[ P_j \times \left( P_j - \frac{2j-1}{2N} \right)^2 \right] \right) \tag{8}$$

where N is the number of $\frac{\Delta E}{\Delta x}$ measurements taken, and $P_j$ is the probability that the $J^{th}$ measurement of the MIP would be equal to or less than $\frac{\Delta E}{\Delta x}$.

## 4.3 Ionization Energy Deposition

As a result of their increased charge, mHSCPs will ionize more intensely. This corresponds to an increase in energy deposition as they pass through the silicon tracker. The average rate of energy loss by moderately relativistic charged heavy particles is given by the Bethe-Bloch equation [27]:

$$-\left\langle \frac{\Delta E}{\Delta x} \right\rangle = 4\pi N_A r_e^2 m_e c^2 z^2 \frac{Z}{A} \frac{1}{\beta^2} \left[ \frac{1}{2} ln \frac{2 m_e c^2 \beta^2 \gamma^2 T_m a x}{I^2} - \beta^2 - \frac{\delta(\beta\gamma)}{2} \right] \times Q^2 \tag{9}$$

where $N_A$ is Avogadro's number, $m_e$ is the mass of an electron, $r_e$ is the classical electron radius, c is the speed of light in a vacuum, z is the electric charge of the particle (in $\frac{e}{3}$), Z is the absorber atomic number, A is the absorber mass number, $\beta$ is the ratio of the particle's speed to the speed of light ($c$), $\gamma$ is the Lorentz factor $\gamma = \frac{1}{\sqrt{1-\beta^2}}$, $T_{max}$ is the maximum kinetic energy that can be imparted onto a free electron in a single collision, $I$ is the average excitation potential, $\delta(\beta\gamma)$ is Fermi's density correction, and $Q$ is the electric charge of the particle in units of $e$.

Qualitatively, energy loss reaches a minimum at relativistic speed ($\beta\gamma \approx 2$). Beyond this point, energy loss is roughly constant, until the effects of radiation dominate. At non-relativistic speeds, $0.1 < \beta\gamma < 2$, energy loss is proportional to $\frac{1}{\beta^2}$. Finally, the energy loss is all proportional to the square of the charge of the particle.

As a result of the complicated nature of ionization energy deposition, large fluctuations in individual $\frac{\Delta E}{\Delta x}$ measurements have been observed [28]. These fluctuations tend to follow a Landau distribution for charged particles in a thin medium [27]. Thus it is appropriate to utilize an estimator that describes the most probable energy loss for the tracker of interest. While there are many ways to define such a value, in this search we use the harmonic mean, $I_h$.

$$I_h = \left( \frac{1}{N} \sum_{j=1}^{N} \left( \frac{\Delta E}{\Delta x} \right)_j^k \right)^{\frac{1}{k}} \tag{10}$$

where $k = -2$, which serves as a means of suppressing higher individual values of $\frac{\Delta E}{\Delta x}$. This has the effect of more easily distinguishing SM particles with a higher than normal fluctuation in $\frac{\Delta E}{\Delta x}$ from HSCPs and mHSCPs, both of which would be characterized by several large individual $\frac{\Delta E}{\Delta x}$ measurements. The difference between $I_{as}$ and $I_h$ arises from the $P_j$ multiplying the squared term in the summation when calculating $I_{as}$. Practically, this corresponds to smaller values for the discriminator in standard model simulations ($I_{as} < 0.4$). Whereas, the mHSCP simulations typically have a discriminator with values ranging up to 1. This difference is how the incompatibility with the MIP hypothesis is expressed.

## 4.4 Time Of Flight

As a result of the larger mass, HSCPs and mHSCPs will, for a given momentum, tend to travel slower than SM particles. Thus, time of flight (TOF) information can be used to narrow down the possible HSCP candidates. As previously mentioned in section 3.2.5, drift tubes located in the muon system calculate the TOF information using the known propagation times for electrons within the ionized gas contained in the tubes.

### 4.4.1 Drift Tube Time Measurements

Once a charged particle passes through a DT, the gas becomes ionized. Under the influence of the electric field between the anode and the cathode inside the DT, electrons are accelerated to the center most anode wire. The electrons moving to the central wire transmit the amplitude and time information to the readout instruments. This means there are four independent events that effect the time of flight calculation: the time of flight of SM particles from the interaction point to the muon system ($t_c$), the time it takes for the electrons to drift whilst in the tube (this quantity is known from the calibration of the muon system [29]), the time for the prorogation of the signal along the central wire ($t_w$), and an off-time correction for delayed particles ($\delta_t$) (see section 3.2.5).

The staggered pattern in conjunction with the information provided by $t_w$ and $t_c$ allow us to construct a coarse trajectory of the particle. We can then refine this trajectory by iterating over the $\delta_t$ to match the measured timing of the DT cells. Starting with $\delta_t \approx 0$ (which corresponds to $\beta \approx 1$) the delay in arrival of the particle results in shifting the calculated position of the particle closer to the edge of the DT. Positive values for $\delta_t$ will shift the position of the particle closer to the wire, while negative values will shift the position towards the edge. The iterations are finished once an appropriate time delay is found, one that has the different DT aligned. This is what allows us to find the inverse $\beta$ (TOF) of the particle.

### 4.4.2 Inverse $\beta$

Physically, $\delta_t$ is the equal to the temporal difference between SM particle (with speed $c$) and a particle moving with speed $\beta c$, from the interaction site to a given drift tube. Letting the distance from the interaction point to the drift tube be $L$ we can write $\delta_t$ as:

$$\delta_t = \frac{L}{\beta c} - \frac{L}{c} \tag{11}$$

Rearranging to solve for inverse $\beta$ yields;

$$\frac{1}{\beta} = 1 + \frac{c\delta_t}{L} \tag{12}$$

We can now calculate a weighted average of inverse $\beta$ over the different layers of the muon system. The weight for the $i^{th}$ component, given by:

$$w_i = \frac{n-2}{n}\frac{L_i^2}{\sigma_{DT}^2} \tag{13}$$

where $n$ is the number of measurements in the DT chamber used to constrain $\delta_t$ and $\sigma_{DT}^2 = 3ns$ is the time resolution of the DTs. The factor of $\frac{n-2}{n}$ accounts for the fact that $\delta_t$

values are computed using two parameters of a straight line, determined from the same n measurements.

# 5 Multi-Charged HSCP Analysis

The multi-charged HSCP analysis searches for mHSCPs observed in the tracker as well as the muon system. Characterized by their lower speed and higher ionization compared to SM particles, these particles are identified by their time of flight measurements in the muon system and their ionization energy loss within the inner tracker. Each of the different signal samples used in the analysis are generated with PYTHIA version 6 [30]. The behavior of the particles as they propagate through the detector was simulated using GEANT4 framework [31]. More information about the behavior of these particles can be found in chapter 4.

## 5.1 Data Selection

The muon system and tracker provide the $\frac{\Delta E}{\Delta x}$ and TOF measurements, respectively. The first step in the offline selection process is to pair the reconstructed tracker path with the appropriate path in the muon system. The resulting pair is known as the global muon. In order to produce reliable results, conditions are imposed on the tracks before it is deemed a global muon. One such requirement is that it must have at least six $\frac{\Delta E}{\Delta x}$ measurements in the strip detector, where the number of measurements corresponds to the number of strip and pixel measurements minus the number of cluster cleared events. The multitude of required measurements allows us to get a reliable calculation of $\left\langle \frac{\Delta E}{\Delta x} \right\rangle$. In addition, there need to be at least eight $\frac{1}{\beta}$ measurements made within the muon systems. Six of which (or more) need to exclusively come from either the DTs or the CSCs. This has the effect of producing a reliable estimate of the $\left\langle \frac{1}{\beta} \right\rangle$ measurement. The average must be greater than 1.075, which implies a particle not moving at near light speeds (in contrast to the assumptions made with SM particles). The measurement is also required to have an uncertainty of less than 15 percent, to further increase the reliability of the measurements. Requirements on quality and $\chi^2/NDF$ are also applied to further the reliability of the results. The quality of a track determines how pure that track is, with a value of two corresponding to a perfect track with the limit of greater than one being required for global muons. A $\chi^2/NDF$ limit of no more than five and a relative error cut on the transverse momentum measurements ($\sigma_{p_t}/p_t$) of no more than twenty five percent are also applied.

Limits on the pseudorapidity of the offline selection are constrained by the geometric boundry of the muon system, i.e., $|\eta| < 2.1$. The global muon track must have a minimum of eight degrees of freedom. Limits are also placed on the number of hits recorded in the tracker, requiring at least eight hits in the inner tracker, with a minimum of two being exclusively in a pixel detector. Eighty percent of the silicon layers between the first and last measurement should have a measurement of that track. Further, the global muon track must not be detected a distance of 0.5 centimeters or more in the transverse (xy) or beam (z) directions from the associated primary vertex.

A minimum was placed on the $\frac{\Delta E}{\Delta x}$ estimator that is below the average ionization energy deposition of a near speed of light, SM particle (3 MeV/cm). Increasing this minimum would have the effect of reducing the number of SM MIPs stored without having an effect on highly ionizing mHSCPs. Note, if you ncreased it enough it will have an effect on HSCPs .

Tracker isolation is used in this analysis. The tracker isolation is defined as the sum of the transverse momentum from all tracks (with the exception of candidate track) within the cone of $\Delta R = \sqrt{\Delta\Phi^2 + \Delta\eta^2} < 0.5$ along the candidate track direction, and is restricted to values less than 50 GeV. On the other hand, calorimeter isolation is not utilized in the multiply charged analysis. The calorimeter isolation is defined as the ratio of summed HCAL and ECAL energies within the cone $\Delta R = \sqrt{\Delta\Phi^2 + \Delta\eta^2} < 0.5$ along the direction of the global muon track momentum.

## 5.2 Background Prediction

As a result of the imperfections in simulations, the mHSCP analysis utilizes a data driven approach to predict the SM background. This has the effect of mitigating the potential uncertainties which are inherent to simulation. This approach is predicated on the idea that there may exist variables that are uncorrelated for SM background, but are correlated for mHSCP signal effectively meaning that we can use the number of events in one region of phase space (i.e. the background region) to predict the number of expected events in another region (i.e. signal region), this allows us to predict the number of SM candidates. In this analysis, the regions are defined by the cuts on $\frac{1}{\beta}$ and $I_{as}$. Other searches for mHSCPs have shown the lack of correlation between $\frac{1}{\beta}$ and $I_{as}$ [25] [32].

We can determine the number of SM particles with large $\frac{1}{\beta}$ and large $I_{as}$ by scaling the number of SM particles with large $\frac{1}{\beta}$ and small $I_{as}$ or vice versa. Imposing cuts on $\frac{1}{\beta}$ and $I_{as}$, forces data candidates into four regions of the $\frac{1}{\beta}$-$I_{as}$ phase space: A, B, C, and D, as seen in Fig 10.

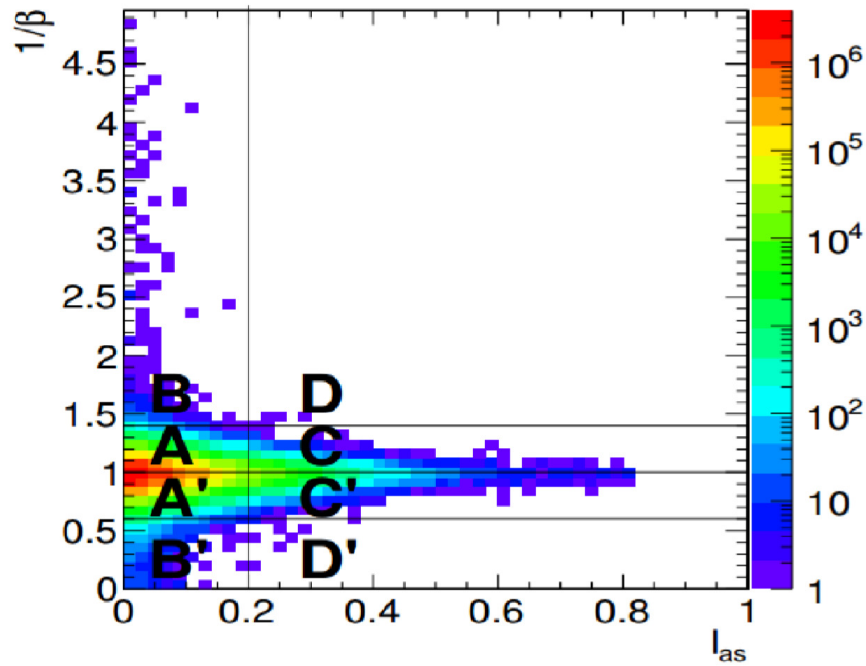


Figure 10: The distribution of 1/beta versus $I_{as}$ in phase space. The regions labeled A, B, and C are used for the background estimate on region D. Note this particular phase space was used in another analysis, operating at a lower center of mass energy ($\sqrt{s}$ =7 TeV) [25]

Region A is the region of phase space in which the data candidates pass neither the selection value for $\frac{1}{\beta}$ nor the selection value of $I_{as}$. Region B corresponds to the region of phase space in which the data candidates pass the selection value for $\frac{1}{\beta}$, but fail on the selection value of $I_{as}$. Region C is the region of phase space in which the data candidates pass the selection value for $I_{as}$, but fail on the selection value of $\frac{1}{\beta}$. Region D corresponds to the region of phase space in which the data candidates pass both the selection value of $\frac{1}{\beta}$ and the selection value of $I_{as}$, and is the region in which, tentatively, the mHSCP signal might reside. As for regions A', B', C', and D', these are useful in testing the background estimate. Each of the primed regions have no signal and can be used to compare our expectations.

However, these have not been used in this analysis.

As a consequence of the lack of correlation between $\frac{1}{\beta}$ and $I_{as}$ in standard model particles, the ratio of events in regions A and B of the phase space is the same as the ratio of the events in region C and D of the phase space. In other words;

$$\frac{N_A}{N_B} = \frac{N_C}{N_D} \tag{14}$$

where $N_A$ is the number of events in region A of the phase space (likewise for the other regions). Using the different number of events in the A,B, and C regions, a background estimate for the number of events in region D ($N_D$) can be calculated.

$$N_D = \frac{N_B N_C}{N_A} \tag{15}$$

The statistical uncertainty on the number of events in region D is:

$$\sigma_{N_D} = \sqrt{\left(\frac{N_B N_C}{N_A^2}\right)^2 N_A + \left(\frac{N_B}{N_A}\right)^2 N_C + \left(\frac{N_C}{N_A}\right)^2 N_B} \tag{16}$$

The number of observed candidates in region D of the phase space can then be compared to the prediction. If the number of observed events in the D region is significantly greater than the prediction, this could be indicative of the presence of mHSCPs. However, this analysis focuses solely on the calculation of the expected cross section limit and does not do this.

This background prediction from the data is combined with the signal efficiencies from the simulations to yield an expected cross section limit. The cross section represents the probability that when two particles collide a specific process will occur. A cross section limit shows which cross sections are excluded based on the dataset available. The expected cross section limit shows what cross section limit would be produced if the data agree with the prediction. This analysis focuses on testing the expected cross sectional limits for different signals.

The Drell-Yan signal occurs when a quark and anti-quark annihilate, produce a virtual photon that decays into two leptons. The Drell-Yan like signal used in this analysis replaces the two leptons with HSCPs. Both the GMStau and PPStau signals are different processes that produce stau particles (the superpartner version of the tau particle). The GMStau signal refers to gauge mediated symmetry breaking that produces stau particles. The PPStau signal refers to the pair production of stau particles. The gluino refers to the superpartner of the gluon. The stop refers to the superpartner of the top quark. Specifically this analysis looks at a Drell-Yan (DY) like signal for charges Q=1e and Q=2e each with masses of 200, 800, 1400, and 2600 $GeV/c^2$. This analysis also analyzes GMStau and PPStau signals for masses of 200, 651, 1029, and 1409 $GeV/c^2$. Additionally, this analysis uses Gluino signals with a mass fraction of 10 percent and Stop signals of masses 200, 800, 1400, 2000, and 2600 $GeV/c^2$. MHSCP signals considered in this analysis include Drell-Yan, GMStau, PPStau, Gluino, and Stop.

# 6 Results

The final selection for this analysis uses the $\frac{1}{\beta}$ and $I_{as}$ variables. This analysis studies the optimization of these variables by iterating over various values within the ranges of $1.025 \leq \frac{1}{\beta} \leq 1.46$ and $0.025 \leq I_{as} \leq 0.55$ with a particular emphasis on larger values of $I_{as}$. The expected cross section limits on mHSCP production are studied to find the best final selection values.

As an example of the type of results the analysis gets, Figure 11 shows the expected cross section limits as a function of both $\frac{1}{\beta}$ and $I_{as}$. The "best" expected cross section limit is the limit that has the lowest value for a given signal. In the Drell-Yan signal with a mass of 200 $GeV/c^2$ and charge Q=1e, the best expected cross section limit is $2.4436 \times 10^{-4}$ $pb$ and is produced by selections of $\frac{1}{\beta} = 1.350$ and $I_{as} = 0.400$. Note that the values for all the expected cross section limits are given in picobarns ($pb$). Tables containing all the data collected in this analysis are found in appendix A.

The optimal selection criteria yielding the lowest expected cross section limit can vary depending on the sample being studied. One way to optimize the selection is to choose the selection criteria that gives the best expected cross section limit for each sample/mass combination. This would mean the analysis of a GMStau signal with mass of 1409 $GeV/c^2$ would use a selection of $\frac{1}{\beta} = 1.350$ and $I_{as} = 0.450$ (Fig. 12). While the analysis on a Drell-Yan signal with mass of 1400 $GeV/c^2$ and a charge of Q=2e would use a selection of

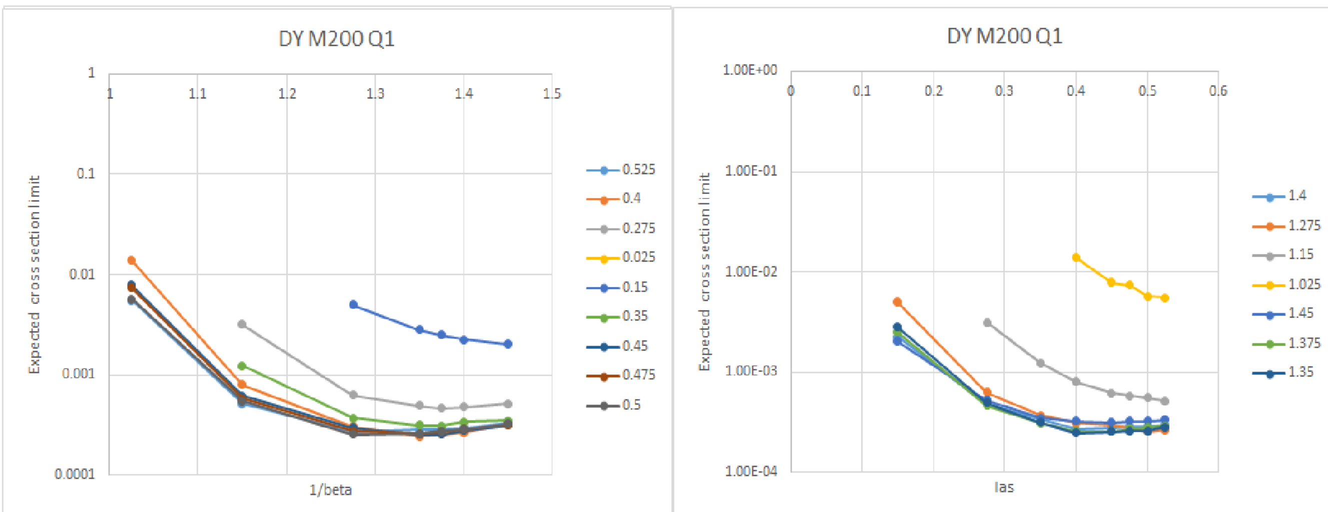


Figure 11: (left) Expected cross section limit as a function of $\frac{1}{\beta}$ for different $I_{as}$ selection values for a Drell-Yan sample with a mass of 200 $GeV/c^2$ and charge of 1e. (right) Expected cross section limit as a function of $I_{as}$ for different $\frac{1}{\beta}$ selection values for the same sample.

$\frac{1}{\beta}$ = 1.275 and $I_{as}$ = 0.525 (Fig.13). However, optimizing an analysis on one signal at a time is rather inefficient. It would be more useful to find a selection that would work for a large number of signals/masses. Table 1 shows the lowest expected cross section limits and the corresponding selection criteria for each signal/mass combination considered in this analysis. Selecting the criteria that produces the greatest number of lowest limits yields selection criteria of $\frac{1}{\beta} = 1.275$ and $I_{as} = 0.500$.

This changes if instead of looking for one value of $\frac{1}{\beta}$ and $I_{as}$ that produces the best expected cross sectional limit, the best selections are found by first looking for the $I_{as}$ that produces the best expected cross section limit more frequently than any other selection of $I_{as}$ then finding the $\frac{1}{\beta}$ that most frequently produces the best expected cross sectional limit given the aforementioned $I_{as}$. This would imply the best limit would be produced by $I_{as} = 0.400$ and $\frac{1}{\beta} = 1.350$. Inversely, if we first establish the optimal $\frac{1}{\beta}$ then the optimal $I_{as}$ this would imply the best limit would be produced by $\frac{1}{\beta} = 1.275$ and $I_{as} = 0.500$. Both of these results can also be found from Table 1.

Alternatively, the optimal selections could correspond to the selections that are best for an analysis containing different signal types with the same mass. As depicted in Fig. 14, that would mean for the mass of 200 $GeV/c^2$ the selection yielding the best expected cross sectional limit would be $\frac{1}{\beta} = 1.275$ and $I_{as} = 0.525$.

As seen in Table 1 the cuts that produce the best expected cross sectional limit tend to vary

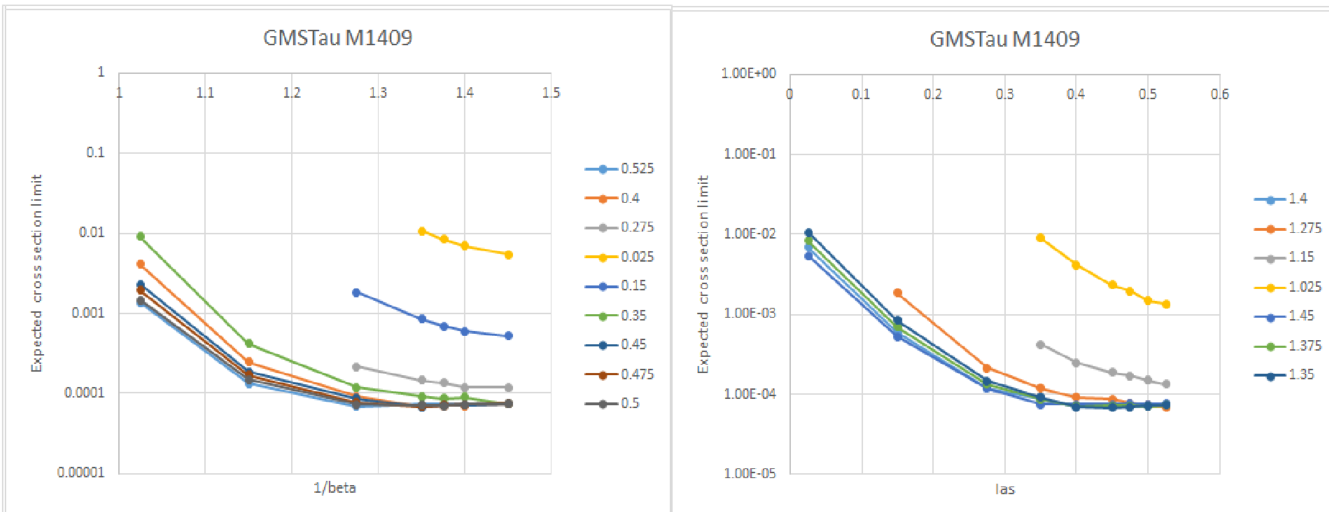


Figure 12: (left) Expected cross section limit as a function of $\frac{1}{\beta}$ for different $I_{as}$ selection values for a GMStau sample with a mass of 1409 $GeV/c^2$. (right) Expected cross section limit as a function of $I_{as}$ for different $\frac{1}{\beta}$ selection values for the same sample. Note, this signal is special in the sense that it produced the lowest expected cross section limit for any sample.

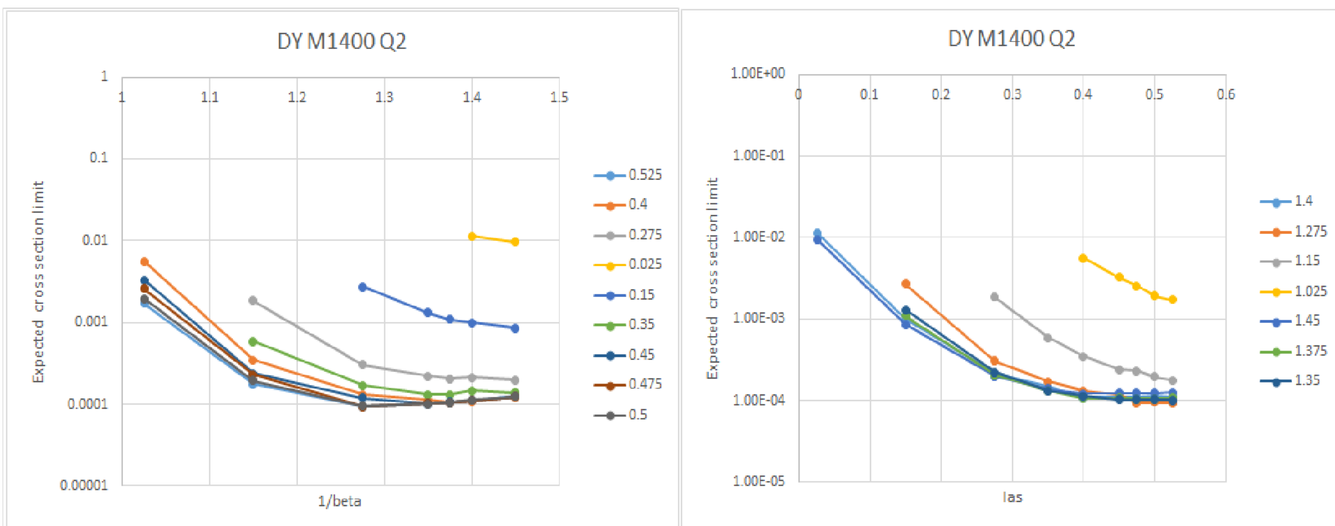


Figure 13: (left) Expected cross section limit as a function of $\frac{1}{\beta}$ for different $I_{as}$ selection values for a Drell-Yan sample with a mass of 1400 $GeV/c^2$ and charge of 2e. (right) Expected cross section limit as a function of $I_{as}$ for different $\frac{1}{\beta}$ selection values for the same sample.

| | | | | | | |
|---|---|---|---|---|---|---|
| GMStau M1409 | 0.450 1.350 | 6.78464E-05 | | DY M200 Q2 | 0.525 1.275 | 2.08148E-04 |
| GMStau M1029 | 0.400 1.375 | 7.26128E-05 | | Stop M1400 | 0.500 1.275 | 2.09756E-04 |
| GMStau M651 | 0.500 1.275 | 8.24998E-05 | | GMStau M200 | 0.400 1.375 | 2.16231E-04 |
| PPStau M1409 | 0.400 1.350 | 8.96788E-05 | | Stop M2600 | 0.400 1.350 | 2.17568E-04 |
| DY M1400 Q2 | 0.525 1.275 | 9.35381E-05 | | Gluino M1400 f10 | 0.500 1.275 | 2.38551E-04 |
| DY M800 Q2 | 0.500 1.275 | 9.70726E-05 | | Gluino M2000 f10 | 0.400 1.350 | 2.43630E-04 |
| PPStau M1029 | 0.475 1.275 | 1.00385E-04 | | DY M200 Q1 | 0.400 1.350 | 2.44361E-04 |
| DY M800 Q1 | 0.475 1.275 | 1.22030E-04 | | Stop M800 | 0.500 1.275 | 2.53780E-04 |
| PPStau M651 | 0.400 1.350 | 1.28233E-04 | | PPStau M200 | 0.450 1.350 | 2.97593E-04 |
| DY M1400 Q1 | 0.400 1.375 | 1.25248E-04 | | Gluino M2600 f10 | 0.400 1.400 | 3.06977E-04 |
| DY M2600 Q1 | 0.475 1.350 | 1.67253E-04 | | Gluino M800 f10 | 0.450 1.350 | 3.25355E-04 |
| DY M2600 Q2 | 0.400 1.375 | 1.75852E-04 | | Stop M200 | 0.500 1.275 | 5.14367E-04 |
| Stop M2000 | 0.500 1.275 | 1.90408E-04 | | Gluino M200 f10 | 0.500 1.275 | 9.76670E-04 |

Table 1: The smallest expected cross section limit for each signal with the corresponding $I_{as}$ and $\frac{1}{\beta}$. The left column shows the signal type followed by the mass of the signal and any other parameters that help define the signal, Q refers to the charge in units of an electron and f refers to the mass percentage for the gluino signals. The middle column shows the $I_{as}$ value followed by the $\frac{1}{\beta}$ value. The right hand column shows the value of the expected cross section limit. Note that the table is organized by smallest to largest expected cross section limits.

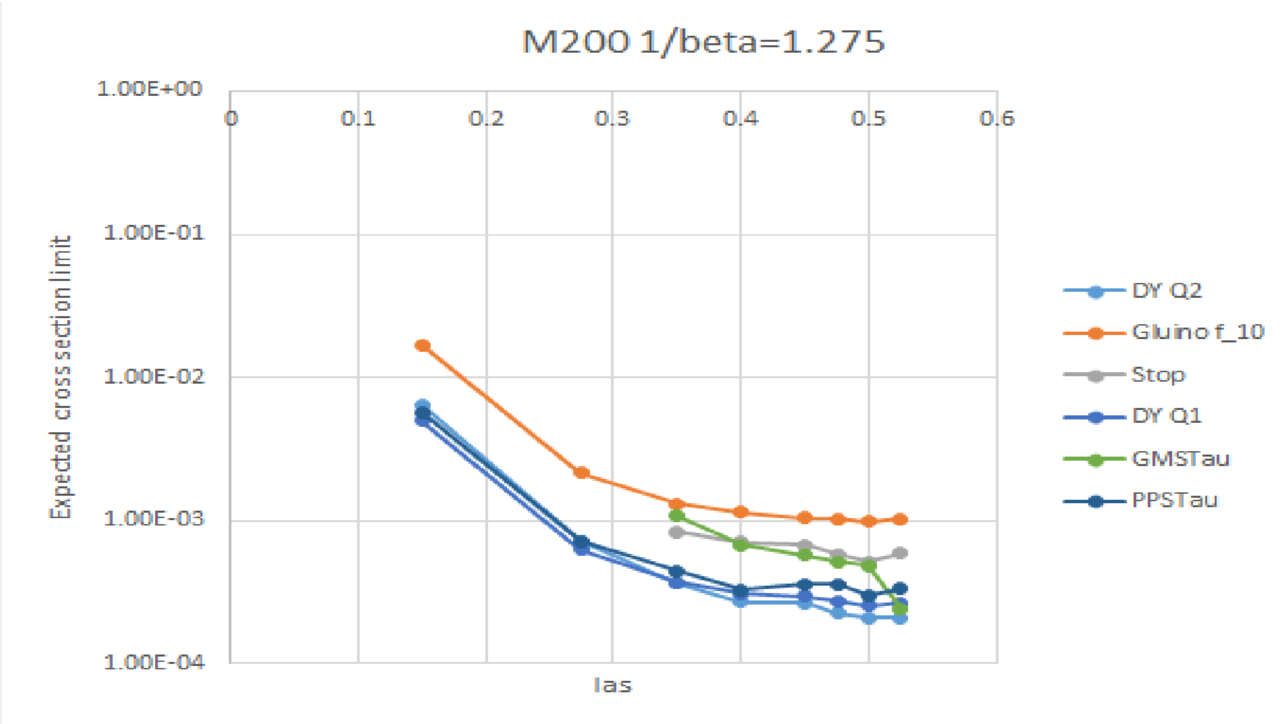


Figure 14: The expected cross sectional limit as a function of $I_{as}$ selection for different signal types, all with a mass of 200 $GeV/c^2$. Each of the different lines corresponds to different signal types with $\frac{1}{\beta} = 1.275$ selection. Note that the graphs with other $\frac{1}{\beta}$ values can be found in appendix B.

wildly depending on how you decide to choose it. Previous expected cross sectional limit optimization algorithms had similar problems. This difficulty arises from the clustering of data points around the lowest expected cross section limit of a given signal.

Another way to determine the best selection is to look at the selections that produce the lowest ten percent of the expected cross sectional limits. By placing less emphasis on the exact minimum and instead focusing on multiple values near the minimum, the optimal selections will be found using data that more accurately describes the behavior of expected cross section limit. In theory this should give us a result that can be applied more generally. If the optimal set of cuts is now defined as the cuts that produce the largest number of expected cross sectional limits in the best 10 % (of the expected cross sectional limits) for each signal type, then it seems that cuts of $\frac{1}{\beta} = 1.275$ and $I_{as} = 0.500$ consistently produce limits on the expected cross section limit in the lowest 10%, with 22 out of 26 signal/mass combinations having expected cross section limits falling in the lowest 10% for these selections (see Table 2). While this isn't a perfect value for every single signal type, it does give an expected cross sectional limit value very close to the mean for the majority of the signals used in this analysis (see Tables 2-6). The median difference between the highest and lowest expected cross sectional limits is 18.80 % and the distribution has a standard deviation of 17.57 %.

A close look at the data reveals that for two of the four signal/masses that the cut $\frac{1}{\beta} = 1.275$ and $I_{as} = 0.500$ fails, the corresponding signal types are for PPStau and GMStau. Applying the method previously mentioned but only on the PPStau and GMStau signal types shows an optimal expected cross section limit that is produced with selections of $\frac{1}{\beta} = 1.350$ and $I_{as} = 0.450$.

| DY M200 Q1 | DY M800 Q1 | DY M1400 Q1 | DY M2600 Q1 |
|---|---|---|---|
| 0.400 1.375 | 0.400 1.375 | 0.400 1.400 | 0.450 1.350 |
| 2.55319E-04 | 1.27421E-04 | 1.26619E-04 | 1.68554E-04 |
| 0.400 1.350 | 0.475 1.350 | 0.400 1.375 | 0.475 1.375 |
| 2.44361E-04 | 1.26455E-04 | 1.25248E-04 | 1.68727E-04 |
| 0.450 1.375 | 0.475 1.275 | 0.450 1.350 | 0.475 1.350 |
| 2.55555E-04 | 1.22030E-04 | 1.27073E-04 | 1.67253E-04 |
| 0.450 1.350 | 0.500 1.275 | 0.475 1.350 | 0.500 1.275 |
| 2.54250E-04 | 1.27783E-04 | 1.26488E-04 | 1.67919E-04 |
| 0.500 1.275 | 0.525 1.150 | 0.525 1.150 | 0.525 1.150 |
| 2.55041E-04 | 1.08988E-04 | 1.07056E-04 | 1.24143E-04 |

Table 2: This table shows the lowest 5 (10 percent of the data) expected cross sectional limit values for the Drell Yan signal with a charge of Q=1e. The first row shows the signal type, mass, and charge. The second row shows the $I_{as}$ and $\frac{1}{\beta}$ for the expected cross section limit shown on the line below that, this pattern is repeated.

| DY M200 Q2 | DY M800 Q2 | DY M1400 Q2 | DY M2600 Q2 |
|---|---|---|---|
| 0.475 1.275 | 0.450 1.350 | 0.475 1.275 | 0.400 1.375 |
| 2.23681E-04 | 1.11131E-04 | 9.42766E-05 | 1.75852E-04 |
| 0.500 1.275 | 0.500 1.275 | 0.500 1.275 | 0.475 1.350 |
| 2.09082E-04 | 9.70726E-05 | 9.54363E-05 | 1.83718E-04 |
| 0.500 1.025 | 0.525 1.350 | 0.525 1.350 | 0.500 1.400 |
| 2.13492E-04 | 1.12589E-04 | 1.00501E-04 | 1.84866E-04 |
| 0.525 1.275 | 0.525 1.275 | 0.525 1.275 | 0.525 1.275 |
| 2.08148E-04 | 1.00126E-04 | 9.35381E-05 | 1.82659E-04 |
| 0.525 1.150 | 0.525 1.150 | 0.525 1.150 | 0.525 1.150 |
| 2.31175E-04 | 8.46284E-05 | 7.44992E-05 | 1.03048E-04 |

Table 3: This table shows the lowest 5 (10 percent of the data) cross sectional values for the Drell Yan signal with a charge of Q=2e. The first row shows the signal type, mass, and charge. The second row shows the $I_{as}$ and $\frac{1}{\beta}$ for the expected cross section limit shown on the line below that, this pattern is repeated.

| | GMStau M200 | GMStau M651 | GMStau M1029 | GMStau M1409 |
|---|---|---|---|---|
| $1^{st}$ selection | 0.400 1.375 | 0.450 1.375 | 0.400 1.375 | 0.400 1.350 |
| $1^{st}$ limit | 2.16231E-04 | 8.46120E-05 | 7.26128E-05 | 6.95720E-05 |
| $2^{nd}$ selection | 0.450 1.350 | 0.450 1.350 | 0.450 1.350 | 0.450 1.350 |
| $2^{nd}$ limit | 2.20468E-04 | 8.29178E-05 | 7.27567E-05 | 6.78464E-05 |
| $3^{rd}$ selection | 0.475 1.350 | 0.475 1.350 | 0.500 1.275 | 0.475 1.350 |
| $3^{rd}$ limit | 2.23240E-04 | 8.38972E-05 | 7.42608E-05 | 6.88227E-05 |
| $4^{th}$ selection | 0.500 1.350 | 0.500 1.275 | 0.525 1.275 | 0.525 1.275 |
| $4^{th}$ limit | 2.26759E-04 | 8.24998E-05 | 7.38977E-05 | 6.88513E-05 |
| $5^{th}$ selection | 0.500 1.275 | 0.525 1.150 | 0.525 1.150 | 0.525 1.150 |
| $5^{th}$ limit | 2.25020E-04 | 7.90851E-05 | 5.49780E-05 | 5.47575E-05 |

Table 4: This table shows the lowest 5 (10 percent of the data) cross sectional values for the GMStau. The first row shows the Signal type, mass, and charge. The second row shows the $I_{as}$ and $\frac{1}{\beta}$ for the expected cross section limit shown on the line below that, this pattern is repeated.

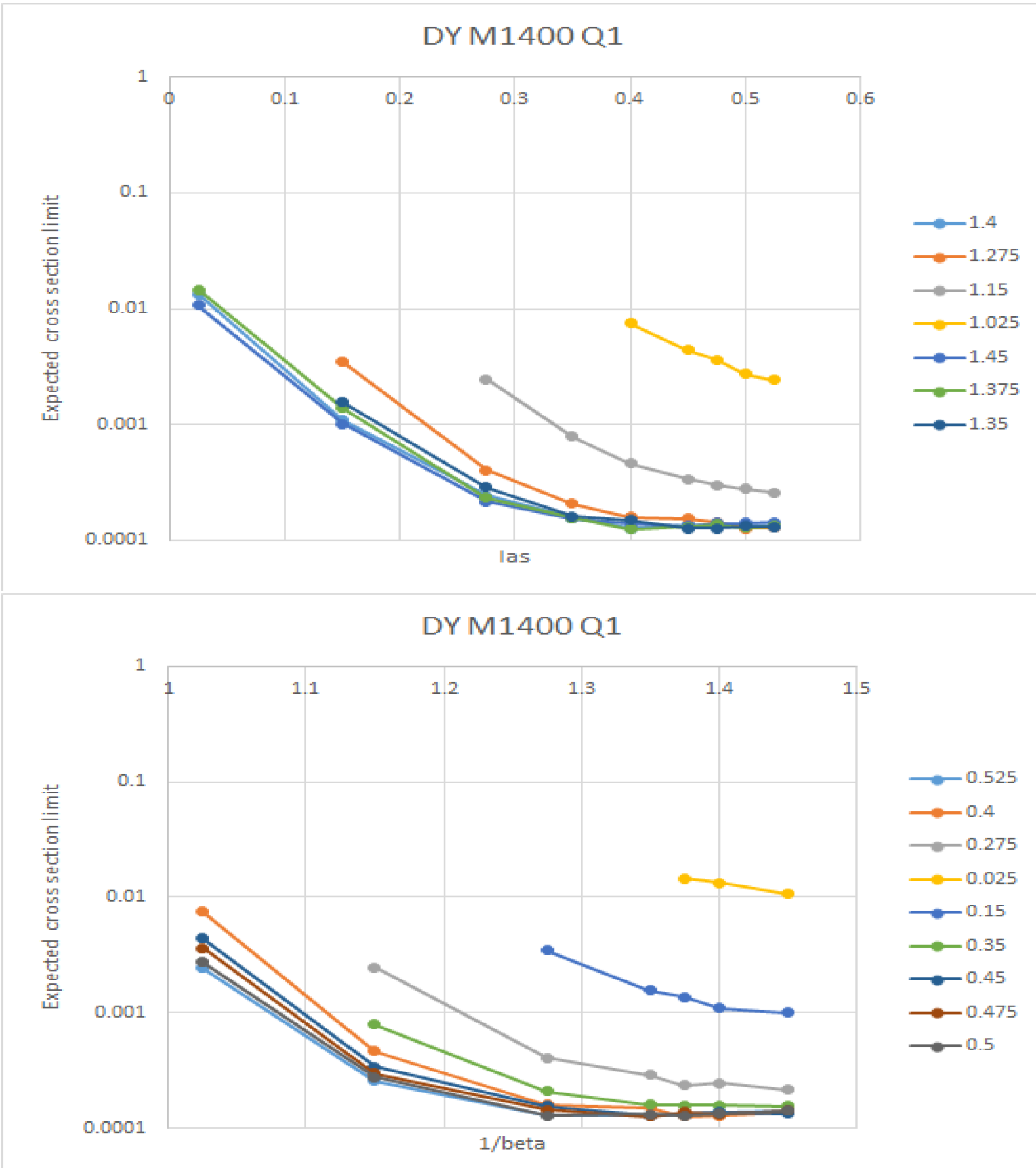


Figure 15: The first plot is a semi-log plot of the expected cross sectional limit as it varies with different cuts of $I_{as}$. where each of the different lines correspond to the different cuts in $\frac{1}{\beta}$. The second plot is a plot of the expected cross section limits versus $\frac{1}{\beta}$ and each line is for different $I_{as}$. Each plot is for a Drell-Yan signal of mass 1400 $GeV/c^2$ and charge $Q = 1e$

| | Gluino M200 f10 | Gluino M800 f10 | Gluino M1400 f10 | Gluino M2000 f10 | Gluino M2600 f10 |
|---|---|---|---|---|---|
| $1^{st}$ selection | 0.400 1.350 | 0.450 1.350 | 0.450 1.375 | 0.400 1.375 | 0.400 1.400 |
| $1^{st}$ limit | 1.01281E-03 | 3.25355E-04 | 2.40747E-04 | 2.53699E-04 | 3.06977E-04 |
| $2^{nd}$ selection | 0.450 1.350 | 0.475 1.350 | 0.475 1.350 | 0.400 1.350 | 0.475 1.350 |
| $2^{nd}$ limit | 9.77860E-04 | 3.32026E-04 | 2.44267E-04 | 2.43630E-04 | 3.12975E-04 |
| $3^{rd}$ selection | 0.475 1.275 | 0.500 1.275 | 0.500 1.275 | 0.450 1.375 | 0.500 1.375 |
| $3^{rd}$ limit | 1.02188E-03 | 3.25362E-04 | 2.38551E-04 | 2.63214E-04 | 3.14150E-04 |
| $4^{th}$ selection | 0.500 1.275 | 0.525 1.275 | 0.525 1.275 | 0.475 1.350 | 0.525 1.400 |
| $4^{th}$ limit | 9.76670E-04 | 3.39447E-04 | 2.41036E-04 | 2.61375E-04 | 3.10954E-04 |
| $5^{th}$ selection | 0.525 1.275 | 0.525 1.150 | 0.525 1.150 | 0.525 1.150 | 0.525 1.275 |
| $5^{th}$ limit | 1.02734E-03 | 3.26631E-04 | 2.05447E-04 | 2.25073E-04 | 3.08764E-04 |

Table 5: This table shows the lowest 5 (10 percent of the data) cross sectional values for the Drell Yan signal with a charge of Q=1e. The first row shows the Signal type, mass, and charge. The second row shows the $I_{as}$ and $\frac{1}{\beta}$ for the expected cross section limit shown on the line below that, this pattern is repeated.

Applying this same method to the remaining signal types, the optimal cross section is produced by the cuts $\frac{1}{\beta} = 1.275$ and $I_{as} = 0.500$. However, if we further divide this up into different masses, the optimal mass shifts to cuts of $\frac{1}{\beta} = 1.275$ and $I_{as} = 0.525$ for heavier masses of 2600 $GeV/c^2$. This is most likely a result of statistical fluctuations and the tightly packed cross section values.

| | PPStau M200 | PPStau M651 | PPStau M1029 | PPStau M1409 |
|---|---|---|---|---|
| $1^{st}$ selection | 0.400 1.375 | 0.400 1.375 | 0.400 1.375 | 0.400 1.375 |
| $1^{st}$ limit | 3.04936E-04 | 1.40095E-04 | 1.08294E-04 | 8.96991E-05 |
| $2^{nd}$ selection | 0.450 1.350 | 0.400 1.350 | 0.450 1.375 | 0.400 1.350 |
| $2^{nd}$ limit | 2.97593E-04 | 1.28233E-04 | 1.06338E-04 | 8.96788E-05 |
| $3^{rd}$ selection | 0.475 1.350 | 0.450 1.350 | 0.450 1.350 | 0.450 1.350 |
| $3^{rd}$ limit | 3.13726E-04 | 1.35949E-04 | 1.07917E-04 | 9.00439E-05 |
| $4^{th}$ selection | 0.500 1.350 | 0.475 1.350 | 0.475 1.275 | 0.475 1.350 |
| $4^{th}$ limit | 3.15972E-04 | 1.40639E-04 | 1.00385E-04 | 9.25885E-05 |
| $5^{th}$ selection | 0.500 1.275 | 0.500 1.275 | 0.525 1.150 | 0.525 1.150 |
| $5^{th}$ limit | 2.97777E-04 | 1.40091E-04 | 1.04578E-04 | 7.72650E-05 |

Table 6: This table shows the lowest 5 (10 percent of the data) cross sectional values for the Drell Yan signal with a charge of Q=1e. The first row shows the Signal type, mass, and charge. The second row shows the $I_{as}$ and $\frac{1}{\beta}$ for the expected cross section limit shown on the line below that, this pattern is repeated.

| | Stop M200 | Stop M800 | Stop M1400 | Stop M2000 | Stop M2600 |
|---|---|---|---|---|---|
| $1^{st}$ selection | 0.450 1.350 | 0.400 1.350 | 0.400 1.350 | 0.400 1.350 | 0.400 1.350 |
| $1^{st}$ limit | 6.56E-04 | 2.90E-04 | 2.19E-04 | 1.98E-04 | 2.18E-04 |
| $2^{nd}$ selection | 0.450 1.275 | 0.475 1.275 | 0.450 1.350 | 0.475 1.350 | 0.450 1.350 |
| $2^{nd}$ limit | 6.75E-04 | 2.78E-04 | 2.20E-04 | 2.06E-04 | 2.27E-04 |
| $3^{rd}$ selection | 0.475 1.275 | 0.500 1.275 | 0.500 1.275 | 0.500 1.275 | 0.500 1.275 |
| $3^{rd}$ limit | 5.82E-04 | 2.54E-04 | 2.10E-04 | 1.90E-04 | 2.29E-04 |
| $4^{th}$ selection | 0.500 1.275 | 0.525 1.275 | 0.525 1.275 | 0.525 1.275 | 0.525 1.275 |
| $4^{th}$ limit | 5.14E-04 | 2.77E-04 | 2.14E-04 | 2.05E-04 | 2.29E-04 |
| $5^{th}$ selection | 0.525 1.275 | 0.525 1.150 | 0.525 1.150 | 0.525 1.150 | 0.525 1.150 |
| $5^{th}$ limit | 5.87E-04 | 2.28E-04 | 1.84E-04 | 1.46E-04 | 1.55E-04 |

Table 7: This table shows the lowest 5 (10 percent of the data) cross sectional values for the Drell Yan signal with a charge of Q=1e. The first row shows the Signal type, mass, and charge. The second row shows the $I_{as}$ and $\frac{1}{\beta}$ for the expected cross section limit shown on the line below that, this pattern is repeated.

# 7 Conclusions

The optimal selection to use will vary with the definition of the optimal cross section. However, the results from this search show that for most scenarios selection of $\frac{1}{\beta} = 1.275$ and $I_{as} = 0.500$ will produce consistent results that are applicable in a several different signal types at several different masses. With this said this analysis did overlook lower values of $I_{as}$ and $\frac{1}{\beta}$. So while this decision was a result of the trends seen before in all the data points on the cross sections, it might be useful to run on every iteration in the range for $I_{as}$ and $\frac{1}{\beta}$. Further, the curves for $I_{as}$ values of 0.025, 0.150, 0.275, and potentially 0.350 seem to not reach a clear minimum. As such, it might be useful to extend the range of values on $\frac{1}{\beta}$ to include a more realistic representation of their behavior. An extension of the ranges for $\frac{1}{\beta}$ of 1.025, 1.15, and perhaps 1.275 could also provide more clarity. In addition, it might be interesting to look smaller cuts on $I_{as}$ and $\frac{1}{\beta}$. Especially for $\frac{1}{\beta} = 1.025$, considering the precipitous drop in cross section at $I_{as} = 0.500$.

# A Tables

This appendix contains all the data tables for the cross section, each table corresponds to a different signal type. Blank spaces in the tables correspond to points where there wasn't enough data to produce a reliable cross section limit.

Tables 1-8 will be for Drell-Yan signals, Table 9 - 12 will be for GMStau signals, Tables 13 - 17 will be for Gluino signals, Tables 18 - 21 will be for PPStau signals, and Tables 22 - 26 will be for Stop signals. Note that all of the expected cross section limits are given in picobarns.

| DY 200 Q1 | | | | | | | |
|---|---|---|---|---|---|---|---|
| $I_a s/\frac{1}{\beta}$ | 1.450 | 1.400 | 1.375 | 1.350 | 1.275 | 1.150 | 1.025 |
| 0.025 | | | | | | | |
| 0.150 | 2.03050E-03 | 2.24886E-03 | 2.48760E-03 | 2.82886E-03 | 4.96244E-03 | | |
| 0.275 | 5.19057E-04 | 4.75388E-04 | 4.65068E-04 | 4.92102E-04 | 6.23167E-04 | 3.14446E-03 | |
| 0.350 | 3.50417E-04 | 3.38863E-04 | 3.09374E-04 | 3.13178E-04 | 3.68679E-04 | 1.23273E-03 | |
| 0.400 | 3.21926E-04 | 2.66713E-04 | 2.55319E-04 | 2.44361E-04 | 3.06475E-04 | 7.96413E-04 | 1.37693E-02 |
| 0.450 | 3.14993E-04 | 2.79617E-04 | 2.55555E-04 | 2.54250E-04 | 2.93559E-04 | 6.14811E-04 | 7.84429E-03 |
| 0.475 | 3.21064E-04 | 2.85934E-04 | 2.68801E-04 | 2.56770E-04 | 2.72314E-04 | 5.81591E-04 | 7.33228E-03 |
| 0.500 | 3.22368E-04 | 2.85607E-04 | 2.75573E-04 | 2.58253E-04 | 2.55041E-04 | 5.51135E-04 | 5.68356E-03 |
| 0.525 | 3.30267E-04 | 2.95976E-04 | 2.88435E-04 | 2.82645E-04 | 2.66689E-04 | 5.13055E-04 | 5.51551E-03 |

Table 8: This table contains the expected cross section limits produced using a Drell-Yan simulation where the mass is 200 $GeV/c^2$ and the charge Q=1e. $I_{as}$ values are given in the left most column and the $\frac{1}{\beta}$ values are given on the first full row.

| DY 200 Q2 | | | | | | | |
|---|---|---|---|---|---|---|---|
| $I_a s/\frac{1}{\beta}$ | 1.450 | 1.400 | 1.375 | 1.350 | 1.275 | 1.150 | 1.025 |
| 0.025 | | | | | | | |
| 0.150 | 2.87580E-03 | 3.08055E-03 | 3.41940E-03 | 3.58413E-03 | 6.42629E-03 | | |
| 0.275 | 5.95870E-04 | 6.48978E-04 | 6.03277E-04 | 5.87080E-04 | 7.15219E-04 | 2.56510E-03 | |
| 0.350 | 4.71961E-04 | 4.20298E-04 | 3.69638E-04 | 3.60568E-04 | 3.65784E-04 | 8.06050E-04 | 1.15107E-02 |
| 0.400 | 4.19187E-04 | 3.46126E-04 | 3.03376E-04 | 2.87443E-04 | 2.70694E-04 | 4.65294E-04 | 5.20935E-03 |
| 0.450 | 4.03816E-04 | 3.47791E-04 | 2.99809E-04 | 2.68323E-04 | 2.64828E-04 | 3.21523E-04 | 2.83226E-03 |
| 0.475 | 4.10994E-04 | 3.45266E-04 | 2.99623E-04 | 2.64641E-04 | 2.23681E-04 | 2.96428E-04 | 2.25673E-03 |
| 0.500 | 4.23589E-04 | 3.38515E-04 | 3.01320E-04 | 2.62755E-04 | 2.09082E-04 | 2.66859E-04 | 1.83212E-03 |
| 0.525 | 4.05233E-04 | 3.42162E-04 | 3.03295E-04 | 2.64736E-04 | 2.08148E-04 | 2.39557E-04 | 1.56917E-03 |

Table 9: This table contains the expected cross section limits produced using a Drell-Yan simulation where the mass is 200 $GeV/c^2$ and the charge Q=2e. $I_{as}$ values are given in the left most column and the $\frac{1}{\beta}$ values are given on the first full row.

| DY 800 Q1 | | | | | | | |
|---|---|---|---|---|---|---|---|
| $I_a s/\frac{1}{\beta}$ | 1.450 | 1.400 | 1.375 | 1.350 | 1.275 | 1.150 | 1.025 |
| 0.025 | 1.17448E-02 | 1.37474E-02 | 1.52901E-02 | | | | |
| 0.150 | 1.09233E-03 | 1.19947E-03 | 1.29542E-03 | 1.52203E-03 | 2.94967E-03 | | |
| 0.275 | 2.40983E-04 | 2.27046E-04 | 2.40563E-04 | 2.57306E-04 | 3.50807E-04 | 2.10499E-03 | |
| 0.350 | 2.03048E-04 | 1.64806E-04 | 1.57607E-04 | 1.58182E-04 | 1.89315E-04 | 7.06296E-04 | 1.54510E-02 |
| 0.400 | 1.48505E-04 | 1.37050E-04 | 1.27421E-04 | 1.28891E-04 | 1.54325E-04 | 4.36645E-04 | 7.32256E-03 |
| 0.450 | 1.56418E-04 | 1.30445E-04 | 1.34631E-04 | 1.29594E-04 | 1.49972E-04 | 3.29536E-04 | 4.11821E-03 |
| 0.475 | 1.53868E-04 | 1.37501E-04 | 1.38096E-04 | 1.26455E-04 | 1.22030E-04 | 2.60213E-04 | 3.49546E-03 |
| 0.500 | 1.57717E-04 | 1.37265E-04 | 1.30931E-04 | 1.36528E-04 | 1.27783E-04 | 2.75615E-04 | 2.72801E-03 |
| 0.525 | 1.56534E-04 | 1.46751E-04 | 1.40811E-04 | 1.35478E-04 | 1.40700E-04 | 2.67613E-04 | 2.54331E-03 |

Table 10: This table contains the expected cross section limits produced using a Drell-Yan simulation where the mass is 800 $GeV/c^2$ and the charge Q=1e. $I_{as}$ values are given in the left most column and the $\frac{1}{\beta}$ values are given on the first full row.

| DY 800 Q2 | | | | | | | |
|---|---|---|---|---|---|---|---|
| $I_as/\frac{1}{\beta}$ | 1.450 | 1.400 | 1.375 | 1.350 | 1.275 | 1.150 | 1.025 |
| 0.025 | 1.14646E-02 | 1.32132E-02 | 1.53278E-02 | 1.71628E-02 | | | |
| 0.150 | 1.11727E-03 | 1.10083E-03 | 1.30219E-03 | 1.46699E-03 | 2.84136E-03 | | |
| 0.275 | 2.44688E-04 | 2.38027E-04 | 2.44671E-04 | 2.43985E-04 | 3.16397E-04 | 1.61845E-03 | |
| 0.350 | 1.67981E-04 | 1.62171E-04 | 1.56940E-04 | 1.56668E-04 | 1.67305E-04 | 5.25836E-04 | 1.07281E-02 |
| 0.400 | 1.52592E-04 | 1.33546E-04 | 1.32941E-04 | 1.18672E-04 | 1.54549E-04 | 3.12116E-04 | 4.75054E-03 |
| 0.450 | 1.49089E-04 | 1.23263E-04 | 1.20752E-04 | 1.11131E-04 | 1.24499E-04 | 2.13297E-04 | 2.63633E-03 |
| 0.475 | 1.41057E-04 | 1.25810E-04 | 1.21025E-04 | 1.13036E-04 | 1.14972E-04 | 1.88248E-04 | 2.15521E-03 |
| 0.500 | 1.51520E-04 | 1.30403E-04 | 1.26151E-04 | 1.18173E-04 | 9.70726E-05 | 1.72442E-04 | 1.62234E-03 |
| 0.525 | 1.51504E-04 | 1.22303E-04 | 1.22151E-04 | 1.12589E-04 | 1.00126E-04 | 1.59517E-04 | 1.40162E-03 |

Table 11: This table contains the expected cross section limits produced using a Drell-Yan simulation where the mass is 800 $GeV/c^2$ and the charge Q=2e. $I_{as}$ values are given in the left most column and the $\frac{1}{\beta}$ values are given on the first full row.

| DY M1400 Q1 | | | | | | | |
|---|---|---|---|---|---|---|---|
| $I_as/\frac{1}{\beta}$ | 1.450 | 1.400 | 1.375 | 1.350 | 1.275 | 1.150 | 1.025 |
| 0.025 | 1.07243E-02 | 1.33777E-02 | 1.46172E-02 | | | | |
| 0.150 | 1.00500E-03 | 1.08835E-03 | 1.37249E-03 | 1.56560E-03 | 3.45057E-03 | | |
| 0.275 | 2.14840E-04 | 2.43103E-04 | 2.34357E-04 | 2.85967E-04 | 4.05366E-04 | 2.46212E-03 | |
| 0.350 | 1.54663E-04 | 1.56520E-04 | 1.55861E-04 | 1.59610E-04 | 2.08069E-04 | 7.82907E-04 | |
| 0.400 | 1.37715E-04 | 1.26619E-04 | 1.25248E-04 | 1.50025E-04 | 1.58707E-04 | 4.63812E-04 | 7.43692E-03 |
| 0.450 | 1.33489E-04 | 1.36495E-04 | 1.30886E-04 | 1.27073E-04 | 1.54754E-04 | 3.38993E-04 | 4.39784E-03 |
| 0.475 | 1.41621E-04 | 1.31651E-04 | 1.36320E-04 | 1.26488E-04 | 1.43116E-04 | 2.98498E-04 | 3.61180E-03 |
| 0.500 | 1.40672E-04 | 1.33254E-04 | 1.28066E-04 | 1.32009E-04 | 1.27377E-04 | 2.76302E-04 | 2.74156E-03 |
| 0.525 | 1.41826E-04 | 1.35552E-04 | 1.32820E-04 | 1.29783E-04 | 1.28852E-04 | 2.56434E-04 | 2.41804E-03 |

Table 12: This table contains the expected cross section limits produced using a Drell-Yan simulation where the mass is 1400 $GeV/c^2$ and the charge Q=1e. $I_{as}$ values are given in the left most column and the $\frac{1}{\beta}$ values are given on the first full row.

| DY 1400 Q2 | | | | | | | |
|---|---|---|---|---|---|---|---|
| $I_as/\frac{1}{\beta}$ | 1.450 | 1.400 | 1.375 | 1.350 | 1.275 | 1.150 | 1.025 |
| 0.025 | 9.56529E-03 | 1.15145E-02 | | | | | |
| 0.150 | 8.57371E-04 | 1.00339E-03 | 1.10091E-03 | 1.31029E-03 | 2.71827E-03 | | |
| 0.275 | 1.96637E-04 | 2.13567E-04 | 2.04785E-04 | 2.21040E-04 | 3.04435E-04 | 1.86487E-03 | |
| 0.350 | 1.38679E-04 | 1.48012E-04 | 1.30540E-04 | 1.31451E-04 | 1.69979E-04 | 5.91624E-04 | |
| 0.400 | 1.22473E-04 | 1.09426E-04 | 1.07324E-04 | 1.11944E-04 | 1.30263E-04 | 3.50529E-04 | 5.63483E-03 |
| 0.450 | 1.23696E-04 | 1.11453E-04 | 1.07115E-04 | 1.02806E-04 | 1.19424E-04 | 2.38880E-04 | 3.28707E-03 |
| 0.475 | 1.25067E-04 | 1.11123E-04 | 1.05368E-04 | 1.02280E-04 | 9.42766E-05 | 2.30089E-04 | 2.57481E-03 |
| 0.500 | 1.23424E-04 | 1.12999E-04 | 1.04258E-04 | 1.01822E-04 | 9.54363E-05 | 1.95983E-04 | 1.94424E-03 |
| 0.525 | 1.26720E-04 | 1.11714E-04 | 1.06144E-04 | 1.00501E-04 | 9.35381E-05 | 1.75749E-04 | 1.72422E-03 |

Table 13: This table contains the expected cross section limits produced using a Drell-Yan simulation where the mass is 1400 $GeV/c^2$ and the charge Q=2e. $I_{as}$ values are given in the left most column and the $\frac{1}{\beta}$ values are given on the first full row.

| DY 2600 Q1 | | | | | | | |
|---|---|---|---|---|---|---|---|
| $I_as/\frac{1}{\beta}$ | 1.450 | 1.400 | 1.375 | 1.350 | 1.275 | 1.150 | 1.025 |
| 0.025 | 1.18725E-02 | 2.88728E-02 | | | | | |
| 0.150 | 1.27410E-03 | 1.56623E-03 | 1.83186E-03 | 2.22407E-03 | 5.17546E-03 | | |
| 0.275 | 3.00023E-04 | 3.17859E-04 | 3.38032E-04 | 3.77199E-04 | 5.73154E-04 | 3.66481E-03 | |
| 0.350 | 1.98898E-04 | 2.15480E-04 | 2.20043E-04 | 2.26211E-04 | 3.03483E-04 | 1.07351E-03 | |
| 0.400 | 1.81742E-04 | 1.71514E-04 | 1.70256E-04 | 1.88242E-04 | 2.09746E-04 | 6.61170E-04 | 1.09820E-02 |
| 0.450 | 1.75113E-04 | 1.76308E-04 | 1.76215E-04 | 1.68554E-04 | 2.18290E-04 | 4.55656E-04 | 6.31255E-03 |
| 0.475 | 1.74920E-04 | 1.72784E-04 | 1.68727E-04 | 1.67253E-04 | 1.98076E-04 | 4.15863E-04 | 5.11446E-03 |
| 0.500 | 1.83273E-04 | 1.72913E-04 | 1.70012E-04 | 1.71440E-04 | 1.67919E-04 | 3.85902E-04 | 3.85475E-03 |
| 0.525 | 1.77970E-04 | 1.80482E-04 | 1.73098E-04 | 1.74820E-04 | 1.71885E-04 | 3.52038E-04 | 3.43367E-03 |

Table 14: This table contains the expected cross section limits produced using a Drell-Yan simulation where the mass is 2600 $GeV/c^2$ and the charge Q=1e. $I_{as}$ values are given in the left most column and the $\frac{1}{\beta}$ values are given on the first full row.

| DY 2600 Q2 | | | | | | | |
|---|---|---|---|---|---|---|---|
| $I_as/\frac{1}{\beta}$ | 1.450 | 1.400 | 1.375 | 1.350 | 1.275 | 1.150 | 1.025 |
| 0.025 | 2.85622E-02 | | | | | | |
| 0.150 | 1.37090E-03 | 1.58813E-03 | 2.02136E-03 | 2.47888E-03 | 5.40093E-03 | | |
| 0.275 | | 3.44209E-04 | 3.80788E-04 | 4.14534E-04 | 6.25009E-04 | 4.11747E-03 | |
| 0.350 | 2.29449E-04 | 2.44113E-04 | 2.35371E-04 | 2.51371E-04 | 3.30315E-04 | 1.19890E-03 | |
| 0.400 | 1.97826E-04 | 1.94321E-04 | 1.75852E-04 | 2.13990E-04 | 2.58923E-04 | 7.29201E-04 | 1.23794E-02 |
| 0.450 | 2.05885E-04 | 1.90633E-04 | 1.89803E-04 | 1.90442E-04 | 2.43233E-04 | 5.22221E-04 | 6.68001E-03 |
| 0.475 | 1.95116E-04 | 1.89121E-04 | 1.92725E-04 | 1.83718E-04 | 1.96281E-04 | 4.62491E-04 | 5.28564E-03 |
| 0.500 | 1.93117E-04 | 1.84866E-04 | 1.91531E-04 | 1.90057E-04 | 1.89084E-04 | 3.96916E-04 | 4.14255E-03 |
| 0.525 | 2.00463E-04 | 1.97712E-04 | 1.89742E-04 | 1.95512E-04 | 1.82659E-04 | 3.75924E-04 | 3.75809E-03 |

Table 15: This table contains the expected cross section limits produced using a Drell-Yan simulation where the mass is 2600 $GeV/c^2$ and the charge Q=2e. $I_{as}$ values are given in the left most column and the $\frac{1}{\beta}$ values are given on the first full row.

| GMStau 200 | | | | | | | |
|---|---|---|---|---|---|---|---|
| $I_as/\frac{1}{\beta}$ | 1.450 | 1.400 | 1.375 | 1.350 | 1.275 | 1.150 | 1.025 |
| 0.025 | | | | | | | |
| 0.150 | 1.48746E-03 | 1.96269E-03 | 2.11330E-03 | 2.47477E-03 | 4.30527E-03 | | |
| 0.275 | 4.12930E-04 | 4.07337E-04 | 4.14067E-04 | 4.09431E-04 | 5.60256E-04 | | |
| 0.350 | 2.82596E-04 | 2.81937E-04 | 2.65504E-04 | 2.62984E-04 | 3.18959E-04 | 1.07009E-03 | |
| 0.400 | 2.52018E-04 | 2.28391E-04 | 2.16231E-04 | 2.40428E-04 | 2.67716E-04 | 6.77986E-04 | 1.17018E-02 |
| 0.450 | 2.53539E-04 | 2.37262E-04 | 2.27684E-04 | 2.20468E-04 | 2.49117E-04 | 5.71136E-04 | 7.26138E-03 |
| 0.475 | 2.59068E-04 | 2.39829E-04 | 2.29360E-04 | 2.23240E-04 | 2.92151E-04 | 5.15627E-04 | 6.18462E-03 |
| 0.500 | 2.55691E-04 | 2.44808E-04 | 2.39039E-04 | 2.26759E-04 | 2.25020E-04 | 4.87261E-04 | 4.98379E-03 |
| 0.525 | 2.69033E-04 | 2.56197E-04 | 2.35635E-04 | 2.45515E-04 | 2.41673E-04 | 4.65081E-04 | 4.69204E-03 |

Table 16: This table contains the expected cross section limits produced using a GMStau simulation where the mass is 200 $GeV/c^2$. $I_{as}$ values are given in the left most column and the $\frac{1}{\beta}$ values are given on the first full row.

| GMStau 651 | | | | | | | |
|---|---|---|---|---|---|---|---|
| $I_a s/\frac{1}{\beta}$ | 1.450 | 1.400 | 1.375 | 1.350 | 1.275 | 1.150 | 1.025 |
| 0.025 | 7.06145E-03 | 8.26083E-03 | 1.03230E-02 | 1.17147E-02 | | | |
| 0.150 | 6.73657E-04 | 7.67557E-04 | 8.77176E-04 | 9.73444E-04 | 2.14111E-03 | | |
| 0.275 | 1.64823E-04 | 1.59833E-04 | 1.57507E-04 | 1.63954E-04 | 2.35933E-04 | | |
| 0.350 | 1.04299E-04 | 9.79807E-05 | 9.40987E-05 | 8.76142E-05 | 1.17400E-04 | 4.23372E-04 | 8.47616E-03 |
| 0.400 | 9.99792E-05 | 8.56878E-05 | 8.50060E-05 | 8.94028E-05 | 1.06920E-04 | 2.88566E-04 | 4.67395E-03 |
| 0.450 | 9.51643E-05 | 9.10495E-05 | 8.46120E-05 | 8.29178E-05 | 1.03108E-04 | 1.99091E-04 | 2.81139E-03 |
| 0.475 | 9.86339E-05 | 8.70082E-05 | 8.57726E-05 | 8.38972E-05 | 8.52855E-05 | 1.95653E-04 | 2.37164E-03 |
| 0.500 | 9.75141E-05 | 9.15699E-05 | 8.95167E-05 | 8.57089E-05 | 8.24998E-05 | 1.78981E-04 | 1.84341E-03 |
| 0.525 | 9.84856E-05 | 9.37798E-05 | 8.96362E-05 | 8.78177E-05 | 8.50420E-05 | 1.63337E-04 | 1.66084E-03 |

Table 17: This table contains the expected cross section limits produced using a GMStau simulation where the mass is 651 $GeV/c^2$. $I_{as}$ values are given in the left most column and the $\frac{1}{\beta}$ values are given on the first full row.

| GMStau 1029 | | | | | | | |
|---|---|---|---|---|---|---|---|
| $I_as/\frac{1}{\beta}$ | 1.450 | 1.400 | 1.375 | 1.350 | 1.275 | 1.150 | 1.025 |
| 0.025 | 5.91049E-03 | 7.69336E-03 | 8.88479E-03 | 1.11175E-02 | | | |
| 0.150 | 5.94467E-04 | 6.50616E-04 | 7.42334E-04 | 8.82709E-04 | 1.83502E-03 | | |
| 0.275 | 1.33009E-04 | 1.46075E-04 | 1.34444E-04 | 1.52253E-04 | 2.10792E-04 | | |
| 0.350 | 1.04299E-04 | 9.79807E-05 | 9.40987E-05 | 8.76142E-05 | 1.17400E-04 | 4.23372E-04 | 8.47616E-03 |
| 0.400 | 8.42295E-05 | 7.55988E-05 | 7.26128E-05 | 8.19315E-05 | 8.96247E-05 | 2.51872E-04 | 4.38080E-03 |
| 0.450 | 8.26007E-05 | 7.63628E-05 | 7.45159E-05 | 7.27567E-05 | 8.83393E-05 | 1.81411E-04 | 2.46123E-03 |
| 0.475 | 8.22202E-05 | 7.71139E-05 | 7.66327E-05 | 7.49021E-05 | 8.71585E-05 | 1.77753E-04 | 1.94423E-03 |
| 0.500 | 8.66880E-05 | 8.03183E-05 | 7.82314E-05 | 7.63709E-05 | 7.42608E-05 | 1.59183E-04 | 1.62294E-03 |
| 0.525 | 8.45582E-05 | 8.40113E-05 | 8.05858E-05 | 7.80683E-05 | 7.38977E-05 | 1.38171E-04 | 1.44519E-03 |

Table 18: This table contains the expected cross section limits produced using a GMStau simulation where the mass is 1029 $GeV/c^2$. $I_{as}$ values are given in the left most column and the $\frac{1}{\beta}$ values are given on the first full row.

| GMStau 1409 | | | | | | | |
|---|---|---|---|---|---|---|---|
| $I_as/\frac{1}{\beta}$ | 1.450 | 1.400 | 1.375 | 1.350 | 1.275 | 1.150 | 1.025 |
| 0.025 | 5.43501E-03 | 6.98104E-03 | 8.41208E-03 | 1.07240E-02 | | | |
| 0.150 | 5.22458E-04 | 6.01615E-04 | 6.99906E-04 | 8.46439E-04 | 1.84088E-03 | | |
| 0.275 | 1.19883E-04 | 1.19057E-04 | 1.34519E-04 | 1.46090E-04 | 2.15493E-04 | | |
| 0.350 | 7.46910E-05 | 8.90994E-05 | 8.70394E-05 | 9.14575E-05 | 1.18839E-04 | 4.21837E-04 | 9.04154E-03 |
| 0.400 | 7.45737E-05 | 7.00711E-05 | 7.05338E-05 | 6.95720E-05 | 9.11979E-05 | 2.48451E-04 | 4.13371E-03 |
| 0.450 | 7.51502E-05 | 7.21023E-05 | 7.16007E-05 | 6.78464E-05 | 8.60109E-05 | 1.85695E-04 | 2.32360E-03 |
| 0.475 | 7.57760E-05 | 7.25486E-05 | 7.23280E-05 | 6.88227E-05 | 7.76606E-05 | 1.69816E-04 | 1.94726E-03 |
| 0.500 | 7.45052E-05 | 7.35921E-05 | 7.01445E-05 | 7.23163E-05 | 7.27204E-05 | 1.49243E-04 | 1.47098E-03 |
| 0.525 | 7.57103E-05 | 7.33663E-05 | 7.29481E-05 | 7.30764E-05 | 6.88513E-05 | 1.34060E-04 | 1.35385E-03 |

Table 19: This table contains the expected cross section limits produced using a GMStau simulation where the mass is 1409 $GeV/c^2$. $I_{as}$ values are given in the left most column and the $\frac{1}{\beta}$ values are given on the first full row.

| Gluino 200 | | | | | | | |
|---|---|---|---|---|---|---|---|
| $I_a s/\frac{1}{\beta}$ | 1.450 | 1.400 | 1.375 | 1.350 | 1.275 | 1.150 | 1.025 |
| 0.025 | 9.79546E-02 | 1.03161E-01 | 1.17191E-01 | 1.24894E-01 | | | |
| 0.150 | 8.91562E-03 | 8.84598E-03 | 9.37598E-03 | 9.98697E-03 | 1.69272E-02 | | |
| 0.275 | 2.12823E-03 | 1.88218E-03 | 1.97527E-03 | 1.78887E-03 | 2.13625E-03 | 1.04888E-02 | |
| 0.350 | 1.41711E-03 | 1.33863E-03 | 1.21634E-03 | 1.15745E-03 | 1.29797E-03 | 3.71857E-03 | 7.55548E-02 |
| 0.400 | 1.29346E-03 | 1.08987E-03 | 1.04723E-03 | 1.01281E-03 | 1.13380E-03 | 2.48231E-03 | 3.89727E-02 |
| 0.450 | 1.37838E-03 | 1.12179E-03 | 1.09869E-03 | 9.77860E-04 | 1.04368E-03 | 1.99869E-03 | 2.34485E-02 |
| 0.475 | 1.36525E-03 | 1.15050E-03 | 1.11869E-03 | 1.04969E-03 | 1.02188E-03 | 1.90646E-03 | 2.05254E-02 |
| 0.500 | 1.41111E-03 | 1.16460E-03 | 1.13482E-03 | 1.07511E-03 | 9.76670E-04 | 1.77106E-03 | 1.53731E-02 |
| 0.525 | 1.39583E-03 | 1.20237E-03 | 1.13954E-03 | 1.17000E-03 | 1.02734E-03 | 1.68228E-03 | 1.58021E-02 |

Table 20: This table contains the expected cross section limits produced using a Gluino simulation where the mass is 200 $GeV/c^2$. $I_{as}$ values are given in the left most column and the $\frac{1}{\beta}$ values are given on the first full row.

| Gluino 800 | | | | | | | |
|---|---|---|---|---|---|---|---|
| $I_as/\frac{1}{\beta}$ | 1.450 | 1.400 | 1.375 | 1.350 | 1.275 | 1.150 | 1.025 |
| 0.025 | | | | | | | |
| 0.150 | 2.83474E-03 | 3.14090E-03 | 3.42545E-03 | 3.87711E-03 | 7.24739E-03 | | |
| 0.275 | 6.27684E-04 | 6.31840E-04 | 6.47750E-04 | 6.55305E-04 | 8.45649E-04 | 5.00636E-03 | |
| 0.350 | 4.70995E-04 | 4.45820E-04 | 4.09313E-04 | 4.04333E-04 | 4.75867E-04 | 1.67391E-03 | |
| 0.400 | 3.79821E-04 | 3.47517E-04 | 3.42227E-04 | 3.45477E-04 | 3.91110E-04 | 9.97123E-04 | 1.71521E-02 |
| 0.450 | 4.12216E-04 | 3.60143E-04 | 3.40138E-04 | 3.25355E-04 | 3.86123E-04 | 8.10638E-04 | 1.04127E-02 |
| 0.475 | 4.05553E-04 | 3.61176E-04 | 3.52782E-04 | 3.32026E-04 | 3.39848E-04 | 7.35490E-04 | 8.60953E-03 |
| 0.500 | 4.13933E-04 | 3.83466E-04 | 3.63752E-04 | 3.48705E-04 | 3.25362E-04 | 6.88161E-04 | 6.79107E-03 |
| 0.525 | 4.19320E-04 | 3.87860E-04 | 3.72510E-04 | 3.66082E-04 | 3.39447E-04 | 6.41135E-04 | 5.89687E-03 |

Table 21: This table contains the expected cross section limits produced using a Gluino simulation where the mass is 800 $GeV/c^2$. $I_{as}$ values are given in the left most column and the $\frac{1}{\beta}$ values are given on the first full row.

| Gluino 1400 | | | | | | | |
|---|---|---|---|---|---|---|---|
| $I_a s/\frac{1}{\beta}$ | 1.450 | 1.400 | 1.375 | 1.350 | 1.275 | 1.150 | 1.025 |
| 0.025 | | | | | | | |
| 0.150 | 1.89550E-03 | 2.19461E-03 | 2.62034E-03 | 2.95735E-03 | 6.82844E-03 | | |
| 0.275 | 4.36882E-04 | 4.54460E-04 | 4.68872E-04 | 4.96933E-04 | 7.04857E-04 | 4.50037E-03 | |
| 0.350 | 2.60903E-04 | 3.08110E-04 | 3.03157E-04 | 3.16146E-04 | 3.90650E-04 | 1.43878E-03 | |
| 0.400 | 2.70983E-04 | 2.49980E-04 | 2.60774E-04 | 2.56122E-04 | 3.08954E-04 | 8.43422E-04 | 1.38984E-02 |
| 0.450 | 2.63624E-04 | 2.49877E-04 | 2.40747E-04 | 2.44571E-04 | 2.92151E-04 | 6.21511E-04 | 7.94884E-03 |
| 0.475 | 2.68793E-04 | 2.49675E-04 | 2.48079E-04 | 2.44267E-04 | 2.64099E-04 | 5.75161E-04 | 6.80446E-03 |
| 0.500 | 2.58049E-04 | 2.54275E-04 | 2.51198E-04 | 2.47623E-04 | 2.38551E-04 | 5.13374E-04 | 5.06305E-03 |
| 0.525 | 2.75107E-04 | 2.58418E-04 | 2.48100E-04 | 2.50889E-04 | 2.41036E-04 | 4.72209E-04 | 4.64833E-03 |

Table 22: This table contains the expected cross section limits produced using a Gluino simulation where the mass is 1400 $GeV/c^2$. $I_{as}$ values are given in the left most column and the $\frac{1}{\beta}$ values are given on the first full row.

| Gluino 2000 | | | | | | | |
|---|---|---|---|---|---|---|---|
| $I_as/\frac{1}{\beta}$ | 1.450 | 1.400 | 1.375 | 1.350 | 1.275 | 1.150 | 1.025 |
| 0.025 | | | | | | | |
| 0.150 | 2.07721E-03 | 2.43740E-03 | 2.87159E-03 | 3.37595E-03 | 7.52068E-03 | | |
| 0.275 | 4.44136E-04 | 4.95899E-04 | 5.28379E-04 | 5.66972E-04 | 7.98814E-04 | 5.23019E-03 | |
| 0.350 | 3.25453E-04 | 3.36503E-04 | 3.33738E-04 | 3.42107E-04 | 4.44261E-04 | 1.63923E-03 | |
| 0.400 | 2.86244E-04 | 2.75317E-04 | 2.53699E-04 | 2.43630E-04 | 3.59422E-04 | 9.61201E-04 | 1.57560E-02 |
| 0.450 | 2.97413E-04 | 2.74103E-04 | 2.63214E-04 | 2.64165E-04 | 3.28737E-04 | 7.21173E-04 | 9.07035E-03 |
| 0.475 | 2.88942E-04 | 2.70214E-04 | 2.68423E-04 | 2.61375E-04 | 2.75418E-04 | 6.14883E-04 | 7.80487E-03 |
| 0.500 | 2.87068E-04 | 2.74565E-04 | 2.72893E-04 | 2.70986E-04 | 2.70777E-04 | 5.81248E-04 | 5.66969E-03 |
| 0.525 | 2.80166E-04 | 2.76521E-04 | 2.82006E-04 | 2.68975E-04 | 2.63792E-04 | 5.08602E-04 | 5.04605E-03 |

Table 23: This table contains the expected cross section limits produced using a Gluino simulation where the mass is 2000 $GeV/c^2$. $I_{as}$ values are given in the left most column and the $\frac{1}{\beta}$ values are given on the first full row.

| Gluino 2600 | | | | | | | |
|---|---|---|---|---|---|---|---|
| $I_as/\frac{1}{\beta}$ | 1.450 | 1.400 | 1.375 | 1.350 | 1.275 | 1.150 | 1.025 |
| 0.025 | | | | | | | |
| 0.150 | 2.17536E-03 | 2.89964E-03 | 3.22805E-03 | 3.91942E-03 | 9.05702E-03 | | |
| 0.275 | 4.95990E-04 | 5.75284E-04 | 6.32840E-04 | 6.74991E-04 | 1.01684E-03 | 6.33633E-03 | |
| 0.350 | 3.85245E-04 | 3.26953E-04 | 3.90223E-04 | 4.11939E-04 | 5.62097E-04 | 2.02157E-03 | |
| 0.400 | 3.34477E-04 | 3.06977E-04 | 3.30000E-04 | 3.42033E-04 | 4.34632E-04 | 1.09720E-03 | |
| 0.450 | 3.22861E-04 | 3.24457E-04 | 3.23974E-04 | 3.20240E-04 | 3.89811E-04 | 8.77460E-04 | 1.10078E-02 |
| 0.475 | 3.38437E-04 | 3.21957E-04 | 3.18890E-04 | 3.12975E-04 | 3.68876E-04 | 7.68978E-04 | 9.12492E-03 |
| 0.500 | 3.37288E-04 | 3.33088E-04 | 3.14150E-04 | 3.26723E-04 | 3.36478E-04 | 6.58603E-04 | 6.62509E-03 |
| 0.525 | 3.32903E-04 | 3.10954E-04 | 3.27199E-04 | 3.23879E-04 | 3.08764E-04 | 6.50291E-04 | 6.20228E-03 |

Table 24: This table contains the expected cross section limits produced using a Gluino simulation where the mass is 2600 $GeV/c^2$. $I_{as}$ values are given in the left most column and the $\frac{1}{\beta}$ values are given on the first full row.

| PPStau 200 | | | | | | | |
|---|---|---|---|---|---|---|---|
| $I_a s/\frac{1}{\beta}$ | 1.450 | 1.400 | 1.375 | 1.350 | 1.275 | 1.150 | 1.025 |
| 0.025 | | | | | | | |
| 0.150 | 2.70527E-03 | 2.80464E-03 | 2.95471E-03 | 3.03744E-03 | 5.69686E-03 | | |
| 0.275 | 6.47796E-04 | 5.61789E-04 | 5.69847E-04 | 5.71466E-04 | 7.13176E-04 | 3.82439E-03 | |
| 0.350 | 3.96244E-04 | 3.97006E-04 | 3.82312E-04 | 3.82864E-04 | 4.39280E-04 | 1.43482E-03 | |
| 0.400 | 3.91110E-04 | 3.28050E-04 | 3.04936E-04 | 3.21498E-04 | 3.29661E-04 | 9.77000E-04 | 1.58088E-02 |
| 0.450 | 3.94863E-04 | 3.25978E-04 | 3.22001E-04 | 2.97593E-04 | 3.56716E-04 | 7.71477E-04 | 1.06732E-02 |
| 0.475 | 4.08276E-04 | 3.41047E-04 | 3.31668E-04 | 3.13726E-04 | 3.58597E-04 | 7.07996E-04 | 8.25269E-03 |
| 0.500 | 4.12839E-04 | 3.61128E-04 | 3.31165E-04 | 3.15972E-04 | 2.97777E-04 | 6.47387E-04 | 6.61435E-03 |
| 0.525 | 4.20644E-04 | 3.76358E-04 | 3.63639E-04 | 3.52591E-04 | 3.32284E-04 | 6.60916E-04 | 6.46332E-03 |

Table 25: This table contains the expected cross section limits produced using a PPStau simulation where the mass is 200 $GeV/c^2$. $I_{as}$ values are given in the left most column and the $\frac{1}{\beta}$ values are given on the first full row.

| PPStau 651 | | | | | | | |
|---|---|---|---|---|---|---|---|
| $I_as/\frac{1}{\beta}$ | 1.450 | 1.400 | 1.375 | 1.350 | 1.275 | 1.150 | 1.025 |
| 0.025 | 1.33232E-02 | 1.37095E-02 | 2.77200E-02 | | | | |
| 0.150 | 1.29726E-03 | 1.24191E-03 | 1.39686E-03 | 1.48298E-03 | 2.72360E-03 | | |
| 0.275 | 3.01401E-04 | 2.57842E-04 | 2.56230E-04 | 2.92151E-04 | 3.40872E-04 | 1.88409E-03 | |
| 0.350 | 1.85196E-04 | 1.81489E-04 | 1.62997E-04 | 1.68500E-04 | 1.92757E-04 | 7.17164E-04 | 1.62429E-02 |
| 0.400 | 1.86602E-04 | 1.46425E-04 | 1.40095E-04 | 1.28233E-04 | 1.49380E-04 | 4.37661E-04 | 7.24961E-03 |
| 0.450 | 1.85007E-04 | 1.51930E-04 | 1.41100E-04 | 1.35949E-04 | 1.64511E-04 | 3.40946E-04 | 4.44788E-03 |
| 0.475 | 1.89447E-04 | 1.58178E-04 | 1.48417E-04 | 1.40639E-04 | 1.49475E-04 | 3.31351E-04 | 3.80456E-03 |
| 0.500 | 1.91383E-04 | 1.60525E-04 | 1.53151E-04 | 1.45649E-04 | 1.40091E-04 | 3.01421E-04 | 3.06217E-03 |
| 0.525 | 1.92557E-04 | 1.67839E-04 | 1.52446E-04 | 1.56021E-04 | 1.47014E-04 | 2.95711E-04 | 2.87440E-03 |

Table 26: This table contains the expected cross section limits produced using a PPStau simulation where the mass is 651 $GeV/c^2$. $I_{as}$ values are given in the left most column and the $\frac{1}{\beta}$ values are given on the first full row.

| PPStau 1029 | | | | | | | |
|---|---|---|---|---|---|---|---|
| $I_a s/\frac{1}{\beta}$ | 1.450 | 1.400 | 1.375 | 1.350 | 1.275 | 1.150 | 1.025 |
| 0.025 | 9.41047E-03 | 1.09485E-02 | 1.17245E-02 | 1.46187E-02 | | | |
| 0.150 | 8.88885E-04 | 9.95661E-04 | 1.04133E-03 | 1.24984E-03 | 2.29563E-03 | | |
| 0.275 | 1.82477E-04 | 1.91514E-04 | 2.03171E-04 | 2.19972E-04 | 2.76960E-04 | 1.66194E-03 | |
| 0.350 | 1.42626E-04 | 1.43793E-04 | 1.29940E-04 | 1.35381E-04 | 1.54673E-04 | 5.43730E-04 | 1.19347E-02 |
| 0.400 | 1.33329E-04 | 1.15180E-04 | 1.08294E-04 | 1.08738E-04 | 1.29147E-04 | 3.58254E-04 | 5.80612E-03 |
| 0.450 | 1.28811E-04 | 1.15671E-04 | 1.06338E-04 | 1.07917E-04 | 1.26551E-04 | 2.66965E-04 | 3.47808E-03 |
| 0.475 | 1.29968E-04 | 1.14046E-04 | 1.09450E-04 | 1.10237E-04 | 1.00385E-04 | 2.47375E-04 | 2.91860E-03 |
| 0.500 | 1.34369E-04 | 1.21117E-04 | 1.15946E-04 | 1.12636E-04 | 1.09512E-04 | 2.29899E-04 | 2.29023E-03 |
| 0.525 | 1.35794E-04 | 1.20937E-04 | 1.16782E-04 | 1.15683E-04 | 1.16429E-04 | 2.15942E-04 | 2.15951E-03 |

Table 27: This table contains the expected cross section limits produced using a PPStau simulation where the mass is 1029 $GeV/c^2$. $I_{as}$ values are given in the left most column and the $\frac{1}{\beta}$ values are given on the first full row.

| PPStau 1409 | | | | | | | |
|---|---|---|---|---|---|---|---|
| $I_as/\frac{1}{\beta}$ | 1.450 | 1.400 | 1.375 | 1.350 | 1.275 | 1.150 | 1.025 |
| 0.025 | 7.97269E-03 | 9.35642E-03 | 1.04488E-02 | 1.20764E-02 | | | |
| 0.150 | 7.91061E-04 | 8.70122E-04 | 9.52043E-04 | 1.07820E-03 | 2.16186E-03 | | |
| 0.275 | 1.71908E-04 | 1.79922E-04 | 1.79225E-04 | 1.93224E-04 | 2.42862E-04 | 1.59498E-03 | |
| 0.350 | 1.23216E-04 | 1.20956E-04 | 1.14779E-04 | 1.15980E-04 | 1.41306E-04 | 5.22527E-04 | 1.12904E-02 |
| 0.400 | 1.06265E-04 | 9.71202E-05 | 8.96991E-05 | 8.96788E-05 | 1.11592E-04 | 3.20370E-04 | 5.26797E-03 |
| 0.450 | 1.08416E-04 | 9.83442E-05 | 9.42648E-05 | 9.00439E-05 | 1.11211E-04 | 2.36452E-04 | 3.03753E-03 |
| 0.475 | 1.09939E-04 | 1.01077E-04 | 9.45333E-05 | 9.25885E-05 | 9.97369E-05 | 2.20151E-04 | 2.45675E-03 |
| 0.500 | 1.10636E-04 | 1.01513E-04 | 9.85302E-05 | 9.57925E-05 | 9.36341E-05 | 2.01702E-04 | 2.00867E-03 |
| 0.525 | 1.11638E-04 | 1.04282E-04 | 9.98068E-05 | 9.50542E-05 | 9.55687E-05 | 1.91529E-04 | 1.81947E-03 |

Table 28: This table contains the expected cross section limits produced using a PPStau simulation where the mass is 1409 $GeV/c^2$. $I_{as}$ values are given in the left most column and the $\frac{1}{\beta}$ values are given on the first full row.

| Stop 200 | | | | | | | |
|---|---|---|---|---|---|---|---|
| $I_as/\frac{1}{\beta}$ | 1.450 | 1.400 | 1.375 | 1.350 | 1.275 | 1.150 | 1.025 |
| 0.025 | 6.99545E-02 | 7.41556E-02 | 8.38861E-02 | 9.09846E-02 | | | |
| 0.150 | 6.83830E-03 | 6.83215E-03 | 6.64036E-03 | 7.60922E-03 | | | |
| 0.275 | 1.51016E-03 | 1.37548E-03 | 1.23027E-03 | 1.31939E-03 | | 7.10054E-03 | |
| 0.350 | 1.06374E-03 | 9.69404E-04 | 8.57504E-04 | 8.50278E-04 | 8.26480E-04 | 2.40250E-03 | |
| 0.400 | 9.52258E-04 | 7.87727E-04 | 7.32443E-04 | 7.15590E-04 | 7.01469E-04 | 1.49238E-03 | |
| 0.450 | 9.76336E-04 | 7.96024E-04 | 7.26701E-04 | 6.55954E-04 | 6.75428E-04 | 1.04640E-03 | 1.08740E-02 |
| 0.475 | 9.59830E-04 | 8.06078E-04 | 7.39154E-04 | 6.77370E-04 | 5.82143E-04 | 1.00164E-03 | 8.93927E-03 |
| 0.500 | 9.93310E-04 | 8.13530E-04 | 7.38115E-04 | 6.85631E-04 | 5.14367E-04 | 8.50530E-04 | 6.83722E-03 |
| 0.525 | 1.02263E-03 | 8.19488E-04 | 7.80864E-04 | 7.00838E-04 | 5.86508E-04 | | 6.23340E-03 |

Table 29: This table contains the expected cross section limits produced using a Stop simulation where the mass is 200 $GeV/c^2$.

$I_{as}$ values are given in the left most column and the $\frac{1}{\beta}$ values are given on the first full row.

| | Stop 800 | | | | | | |
|---|---|---|---|---|---|---|---|
| $I_a s / \frac{1}{\beta}$ | 1.450 | 1.400 | 1.375 | 1.350 | 1.275 | 1.150 | 1.025 |
| 0.025 | | | 2.34076E-03 | | | | |
| 0.150 | 2.38588E-03 | 2.80938E-03 | 3.01962E-03 | 3.59967E-03 | 6.99706E-03 | | |
| 0.275 | 6.04998E-04 | 5.51293E-04 | 5.83546E-04 | 6.10667E-04 | 7.71749E-04 | 4.30211E-03 | |
| 0.350 | 4.03216E-04 | 4.06322E-04 | 3.59771E-04 | 3.90745E-04 | 4.42728E-04 | 1.39968E-03 | |
| 0.400 | 3.61308E-04 | 3.21141E-04 | 2.98370E-04 | 2.89661E-04 | 3.29447E-04 | 8.30868E-04 | 1.35771E-02 |
| 0.450 | 3.57949E-04 | 3.26868E-04 | 3.03613E-04 | 2.90789E-04 | 3.32148E-04 | 6.20592E-04 | 7.05932E-03 |
| 0.475 | 3.58193E-04 | 3.26745E-04 | 3.04184E-04 | 2.95310E-04 | 2.78029E-04 | 5.69357E-04 | 6.19454E-03 |
| 0.500 | 3.69294E-04 | 3.30350E-04 | 3.11413E-04 | 2.97939E-04 | 2.53780E-04 | 5.25957E-04 | 4.98667E-03 |
| 0.525 | 3.62287E-04 | 3.28221E-04 | 3.05947E-04 | 3.05544E-04 | 2.76973E-04 | 4.72440E-04 | 4.67441E-03 |

Table 30: This table contains the expected cross section limits produced using a Stop simulation where the mass is 800 $GeV/c^2$.

$I_{as}$ values are given in the left most column and the $\frac{1}{\beta}$ values are given on the first full row.

| Stop 1400 | | | | | | | |
|---|---|---|---|---|---|---|---|
| $I_a s/\frac{1}{\beta}$ | 1.450 | 1.400 | 1.375 | 1.350 | 1.275 | 1.150 | 1.025 |
| 0.025 | | | | | | | |
| 0.150 | 1.83949E-03 | 2.12799E-03 | 2.37132E-03 | 2.68661E-03 | 5.82689E-03 | | |
| 0.275 | 4.22634E-04 | 4.34790E-04 | 4.51131E-04 | 4.63360E-04 | 6.35555E-04 | 3.74263E-03 | |
| 0.350 | 2.78610E-04 | 2.98898E-04 | 2.92151E-04 | 2.92745E-04 | 3.46021E-04 | 1.19521E-03 | |
| 0.400 | 2.57402E-04 | 2.44052E-04 | 2.25145E-04 | 2.19033E-04 | 2.81863E-04 | 6.67991E-04 | 1.14517E-02 |
| 0.450 | 2.59193E-04 | 2.41316E-04 | 2.35914E-04 | 2.19863E-04 | 2.51935E-04 | 5.16180E-04 | 6.45283E-03 |
| 0.475 | 2.57958E-04 | 2.46603E-04 | 2.31587E-04 | 2.27982E-04 | 2.52408E-04 | 4.82912E-04 | 5.42994E-03 |
| 0.500 | 2.65202E-04 | 2.36484E-04 | 2.32764E-04 | 2.28756E-04 | 2.09756E-04 | 4.36660E-04 | 4.43584E-03 |
| 0.525 | 2.53126E-04 | 2.46768E-04 | 2.32457E-04 | 2.32077E-04 | 2.14055E-04 | 3.73412E-04 | 3.85179E-03 |

Table 31: This table contains the expected cross section limits produced using a Stop simulation where the mass is 1400 $GeV/c^2$.

$I_{as}$ values are given in the left most column and the $\frac{1}{\beta}$ values are given on the first full row.

| Stop 2000 | | | | | | | |
|---|---|---|---|---|---|---|---|
| $I_as/\frac{1}{\beta}$ | 1.450 | 1.400 | 1.375 | 1.350 | 1.275 | 1.150 | 1.025 |
| 0.025 | 2.89612E-02 | | | | | | |
| 0.150 | 1.60365E-03 | 1.93739E-03 | 2.07270E-03 | 2.60532E-03 | 5.50785E-03 | | |
| 0.275 | 4.14838E-04 | 3.86821E-04 | 4.10881E-04 | 4.39631E-04 | 6.17834E-04 | 3.85471E-03 | |
| 0.350 | 3.49225E-04 | 2.70502E-04 | 2.56814E-04 | 2.75371E-04 | 3.34846E-04 | 1.22030E-03 | |
| 0.400 | 2.21830E-04 | 2.08080E-04 | 2.06537E-04 | 1.97533E-04 | 2.60797E-04 | 7.36638E-04 | 1.21232E-02 |
| 0.450 | 2.25420E-04 | 2.22049E-04 | 2.06306E-04 | 2.07306E-04 | 2.43156E-04 | 5.12473E-04 | 6.71531E-03 |
| 0.475 | 2.29973E-04 | 2.19098E-04 | 2.06444E-04 | 2.05863E-04 | 2.23313E-04 | 4.88654E-04 | 5.48445E-03 |
| 0.500 | 2.31092E-04 | 2.31176E-04 | 2.07266E-04 | 2.08643E-04 | 1.90408E-04 | 4.14764E-04 | 4.02909E-03 |
| 0.525 | 2.34205E-04 | 2.16422E-04 | 2.13838E-04 | 2.13618E-04 | 2.04642E-04 | 3.92658E-04 | 3.81818E-03 |

Table 32: This table contains the expected cross section limits produced using a Stop simulation where the mass is 2000 $GeV/c^2$.

$I_{as}$ values are given in the left most column and the $\frac{1}{\beta}$ values are given on the first full row.

| Stop 2600 | | | | | | | |
|---|---|---|---|---|---|---|---|
| $I_as/\frac{1}{\beta}$ | 1.450 | 1.400 | 1.375 | 1.350 | 1.275 | 1.150 | 1.025 |
| 0.025 | 3.28237E-02 | | | | | | |
| 0.150 | 1.73198E-03 | 2.10171E-03 | 2.46759E-03 | 2.90064E-03 | 6.34181E-03 | | |
| 0.275 | 3.84564E-04 | 4.29268E-04 | 4.61868E-04 | 4.88503E-04 | 7.02089E-04 | 4.54711E-03 | |
| 0.350 | 2.93991E-04 | 2.84667E-04 | 2.66762E-04 | 3.00801E-04 | 3.92295E-04 | 1.39654E-03 | |
| 0.400 | 2.53797E-04 | 2.36657E-04 | 2.29767E-04 | 2.17568E-04 | 2.97969E-04 | 8.30197E-04 | 1.43355E-02 |
| 0.450 | 2.53547E-04 | 2.33614E-04 | 2.37520E-04 | 2.27427E-04 | 2.79712E-04 | 5.96808E-04 | 7.88271E-03 |
| 0.475 | 2.43781E-04 | 2.36925E-04 | 2.34219E-04 | 2.30064E-04 | 2.92151E-04 | 5.49678E-04 | 6.36072E-03 |
| 0.500 | 2.46078E-04 | 2.41186E-04 | 2.30115E-04 | 2.36502E-04 | 2.29162E-04 | 5.06744E-04 | 5.15062E-03 |
| 0.525 | 2.46293E-04 | 2.42153E-04 | 2.41737E-04 | 2.29824E-04 | 2.28640E-04 | 4.51234E-04 | 4.05756E-03 |

Table 33: This table contains the expected cross section limits produced using a Stop simulation where the mass is 2600 $GeV/c^2$.

$I_{as}$ values are given in the left most column and the $\frac{1}{\beta}$ values are given on the first full row.

# B Graphs

This appendix contains all of the plots generated by the data used in the analysis. The plots are grouped together by signal type.

## B.1 Drell-Yan Plots (Q=1e and Q=2e)

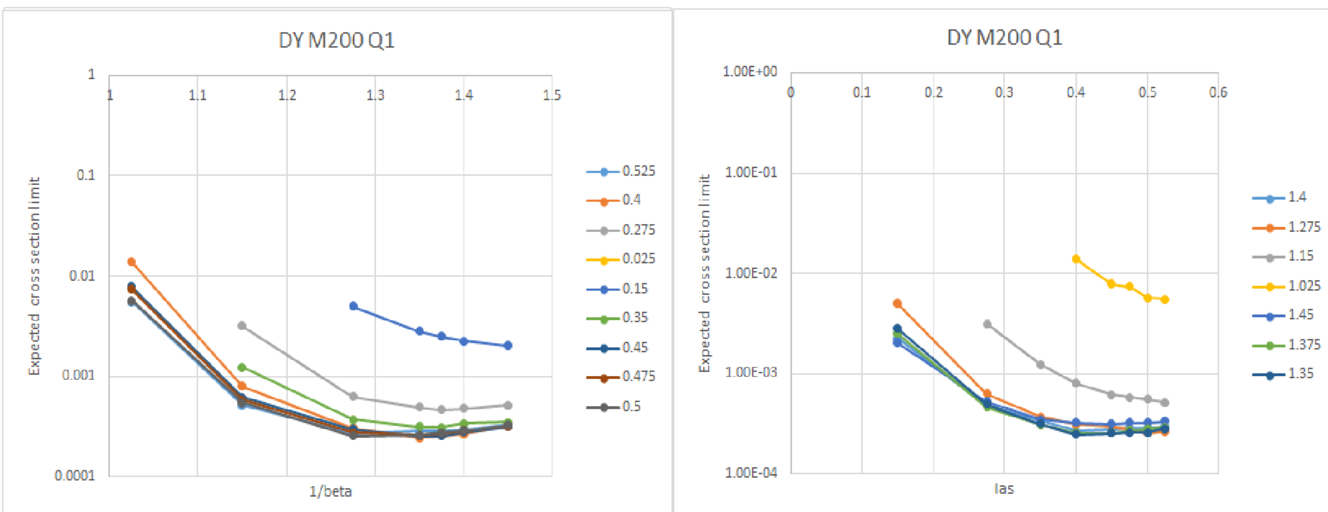


Figure 16: The plot on the right shows the expected cross section limits versus produced by different cuts of $I_{as}$ with the different lines corresponding to different values of $\frac{1}{\beta}$. The plot on the left shows the expected cross section at different $\frac{1}{\beta}$ with the different lines corresponding to different values of $I_{as}$ both for a Drell-Yan signal with mass of 200 $GeV/c^2$ and charge $Q = 1e$.

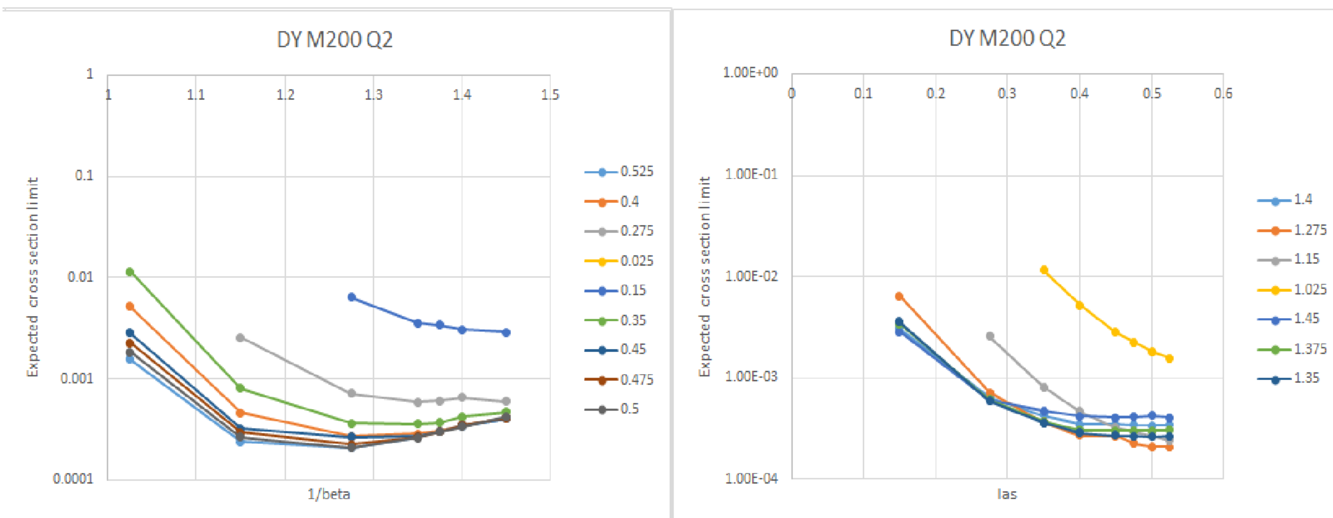


Figure 17: The plot on the right shows the expected cross section limits versus produced by different cuts of $I_{as}$ with the different lines corresponding to different values of $\frac{1}{\beta}$. The plot on the left shows the expected cross section at different $\frac{1}{\beta}$ with the different lines corresponding to different values of $I_{as}$ both for a Drell-Yan signal with mass of 200 $GeV/c^2$ and charge $Q = 2e$.

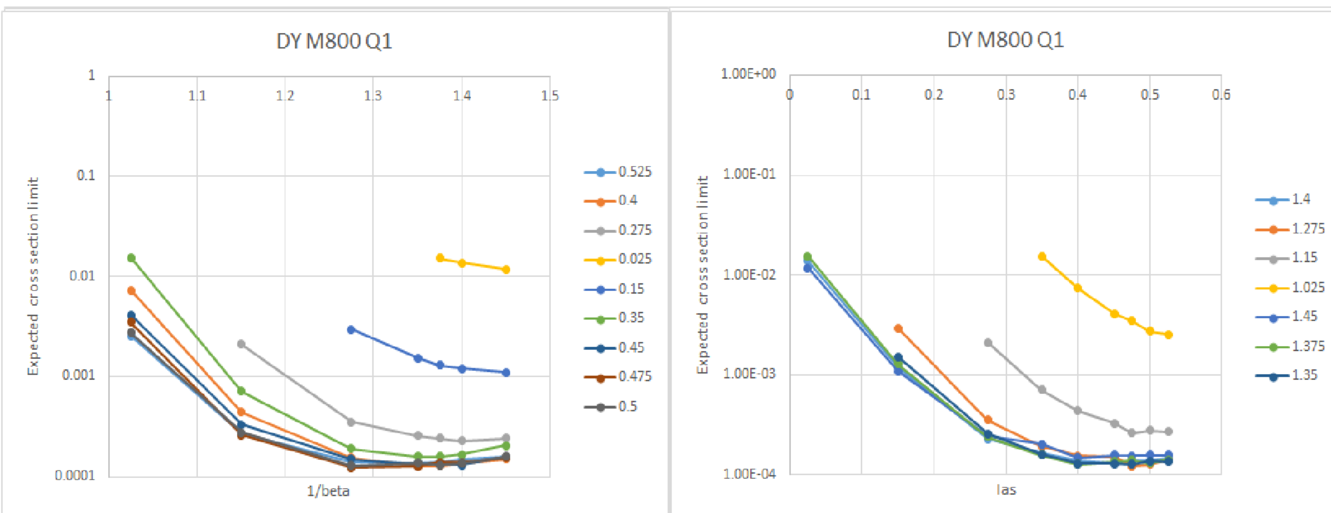


Figure 18: The plot on the right shows the expected cross section limits versus produced by different cuts of $I_{as}$ with the different lines corresponding to different values of $\frac{1}{\beta}$. The plot on the left shows the expected cross section at different $\frac{1}{\beta}$ with the different lines corresponding to different values of $I_{as}$ both for a Drell-Yan signal with mass of 800 $GeV/c^2$ and charge $Q = 1e$.

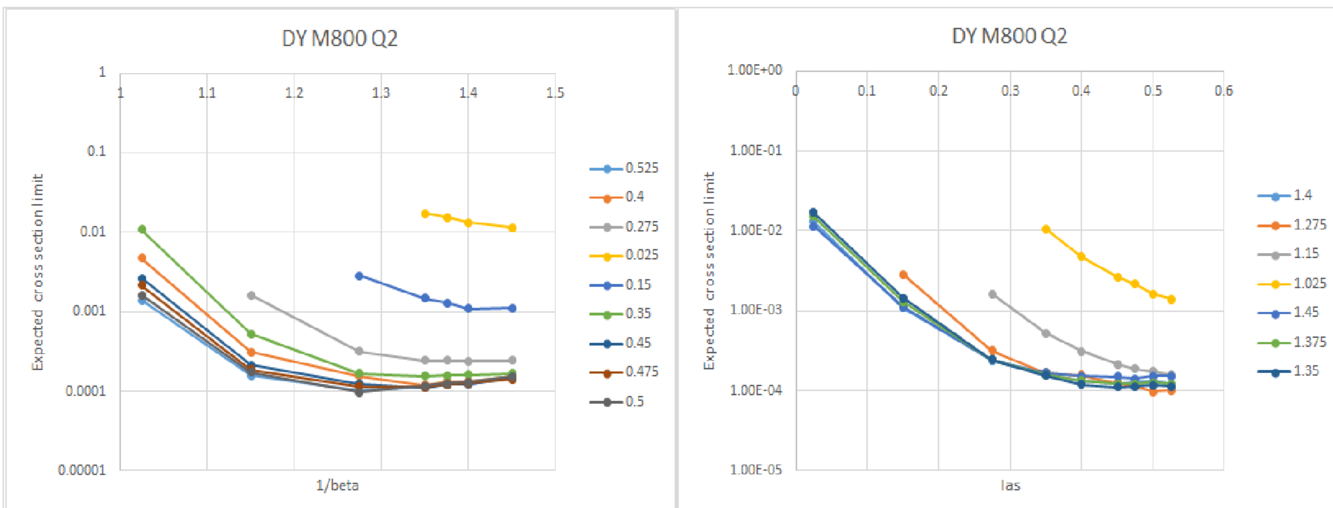


Figure 19: The plot on the right shows the expected cross section limits versus produced by different cuts of $I_{as}$ with the different lines corresponding to different values of $\frac{1}{\beta}$. The plot on the left shows the expected cross section at different $\frac{1}{\beta}$ with the different lines corresponding to different values of $I_{as}$ both for a Drell-Yan signal with mass of 800 $GeV/c^2$ and charge $Q = 2e$.

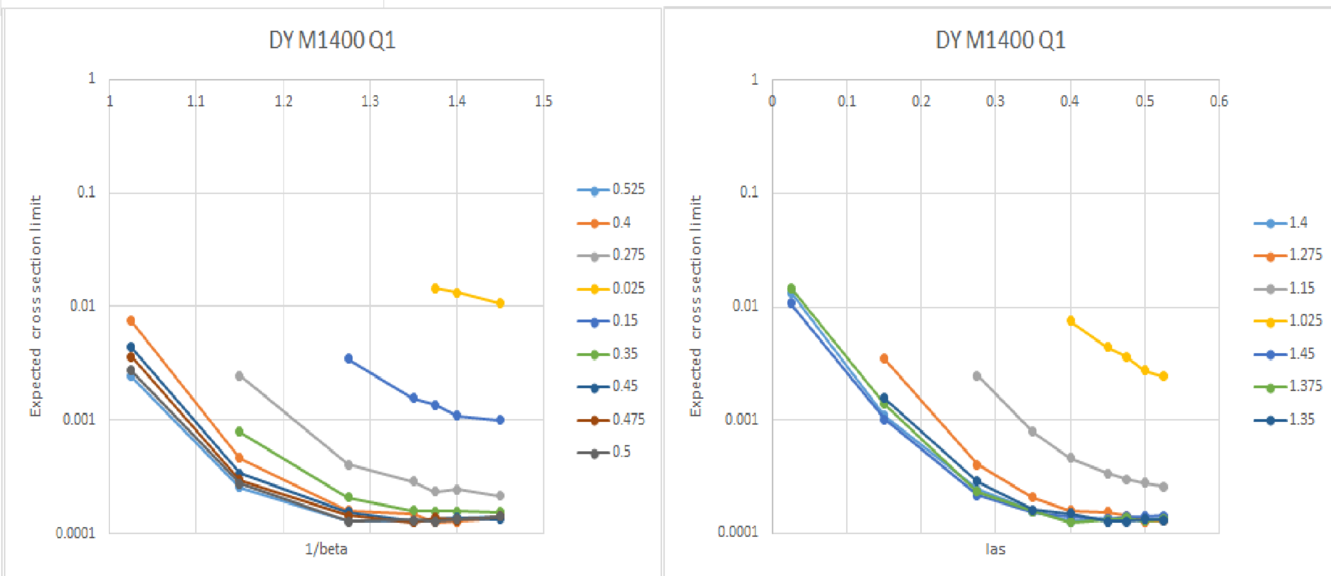


Figure 20: The plot on the right shows the expected cross section limits versus produced by different cuts of $I_{as}$ with the different lines corresponding to different values of $\frac{1}{\beta}$. The plot on the left shows the expected cross section at different $\frac{1}{\beta}$ with the different lines corresponding to different values of $I_{as}$ both for a Drell-Yan signal with mass of 1400 $GeV/c^2$ and charge $Q = 1e$.

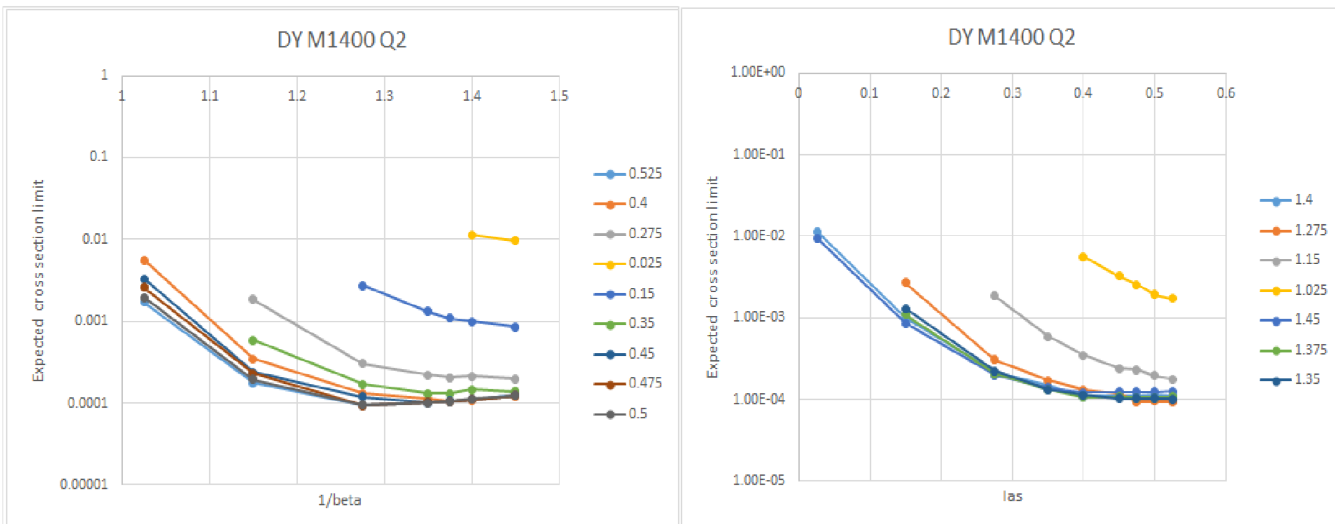


Figure 21: The plot on the right shows the expected cross section limits versus produced by different cuts of $I_{as}$ with the different lines corresponding to different values of $\frac{1}{\beta}$. The plot on the left shows the expected cross section at different $\frac{1}{\beta}$ with the different lines corresponding to different values of $I_{as}$ both for a Drell-Yan signal with mass of 1400 $GeV/c^2$ and charge $Q = 2e$.

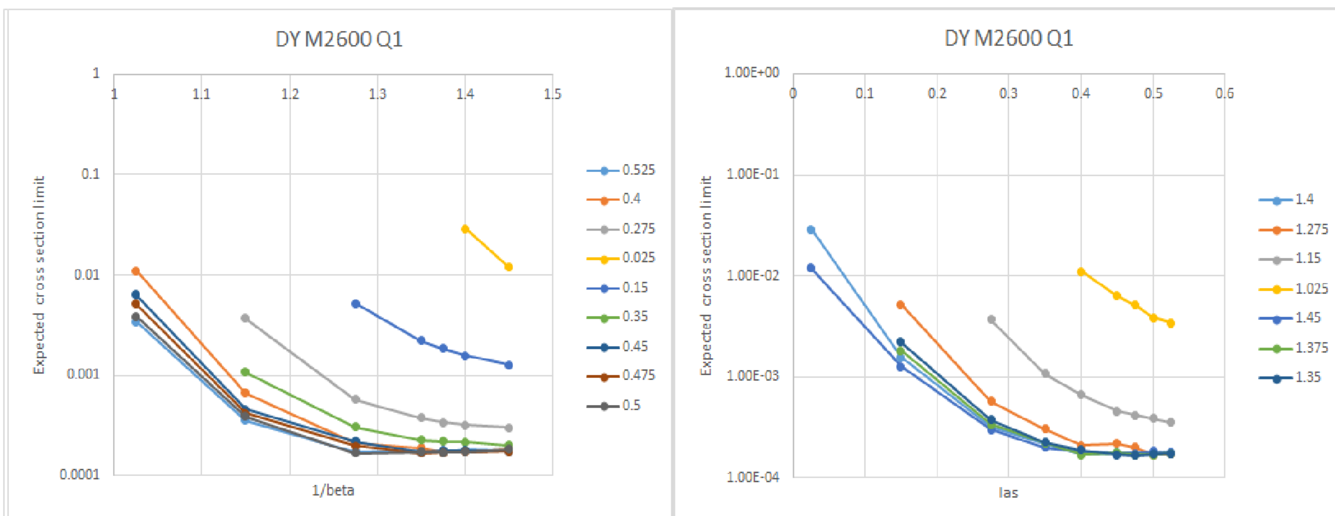


Figure 22: The plot on the right shows the expected cross section limits versus produced by different cuts of $I_{as}$ with the different lines corresponding to different values of $\frac{1}{\beta}$. The plot on the left shows the expected cross section at different $\frac{1}{\beta}$ with the different lines corresponding to different values of $I_{as}$ both for a Drell-Yan signal with mass of 2600 $GeV/c^2$ and charge $Q = 1e$.

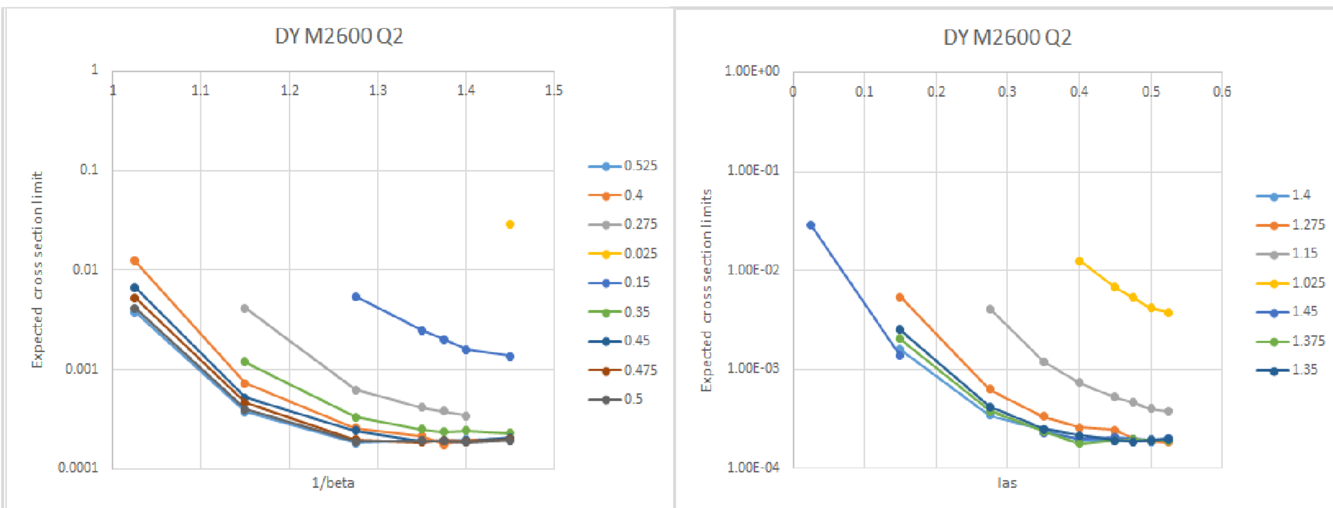


Figure 23: The plot on the left shows the expected cross section limits versus produced by different cuts of $\frac{1}{\beta}$ with the different lines corresponding to different values of $I_{as}$. The plot on the right shows the expected cross section at different $\frac{1}{\beta}$ with the different lines corresponding to different values of $I_{as}$ both for a Drell-Yan signal with mass of 2600 $GeV/c^2$ and charge $Q = 2e$.

## B.2 GMStau plots

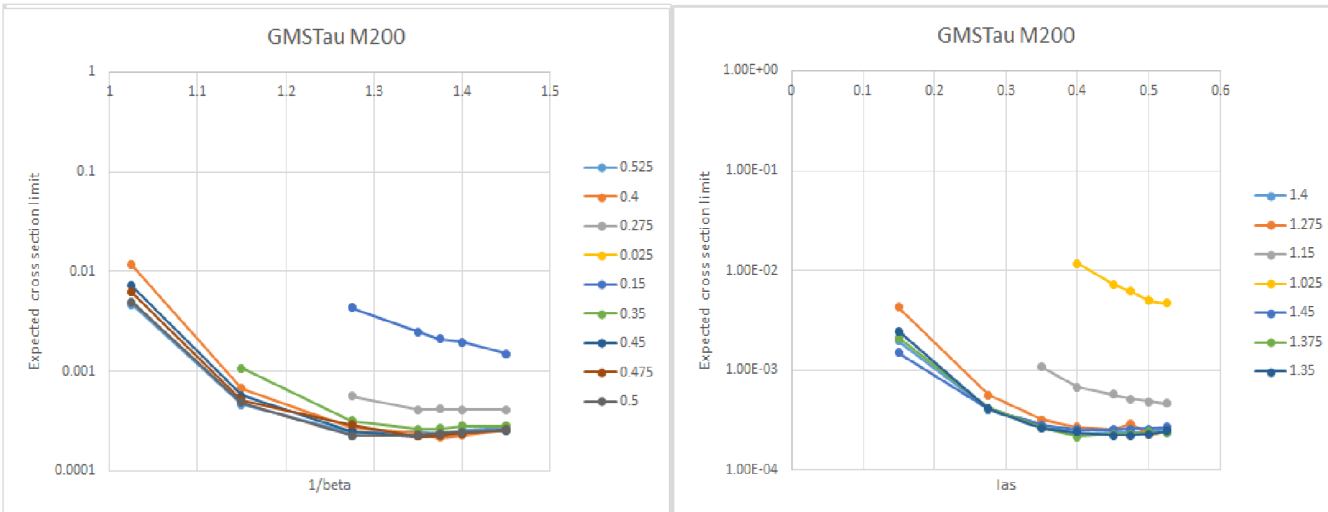


Figure 24: The plot on the left shows the expected cross section limits versus produced by different cuts of $\frac{1}{\beta}$ with the different lines corresponding to different values of $I_{as}$. The plot on the right shows the expected cross section at different $\frac{1}{\beta}$ with the different lines corresponding to different values of $I_{as}$ both for a GMStau signal with mass of 200 $GeV/c^2$.

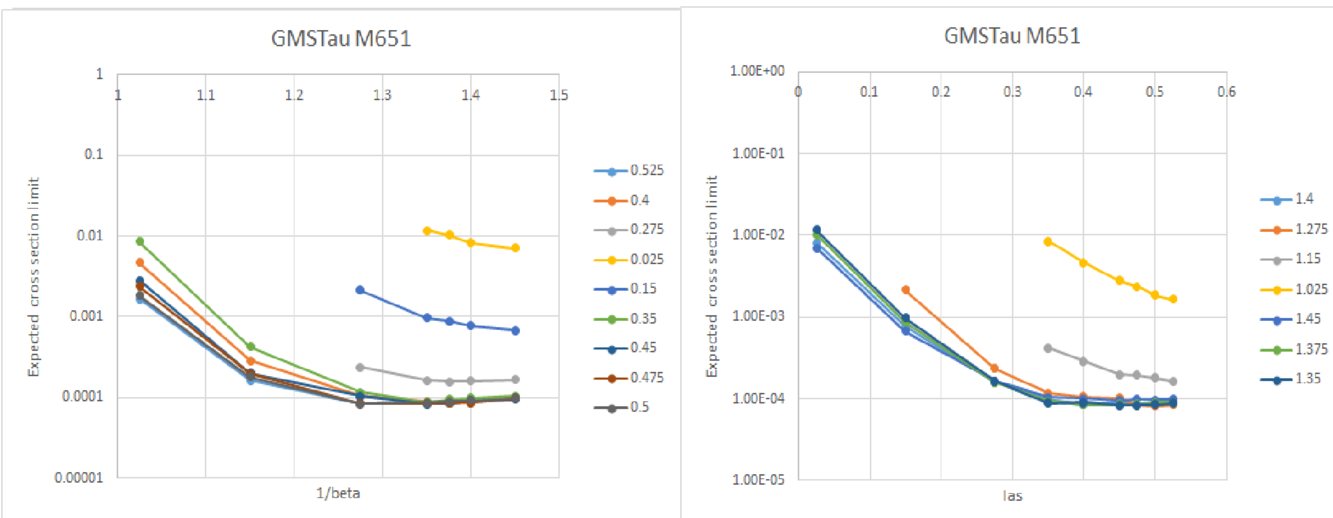


Figure 25: The plot on the left shows the expected cross section limits versus produced by different cuts of $\frac{1}{\beta}$ with the different lines corresponding to different values of $I_{as}$. The plot on the right shows the expected cross section at different $\frac{1}{\beta}$ with the different lines corresponding to different values of $I_{as}$ both for a GMStau signal with mass of 651 $GeV/c^2$.

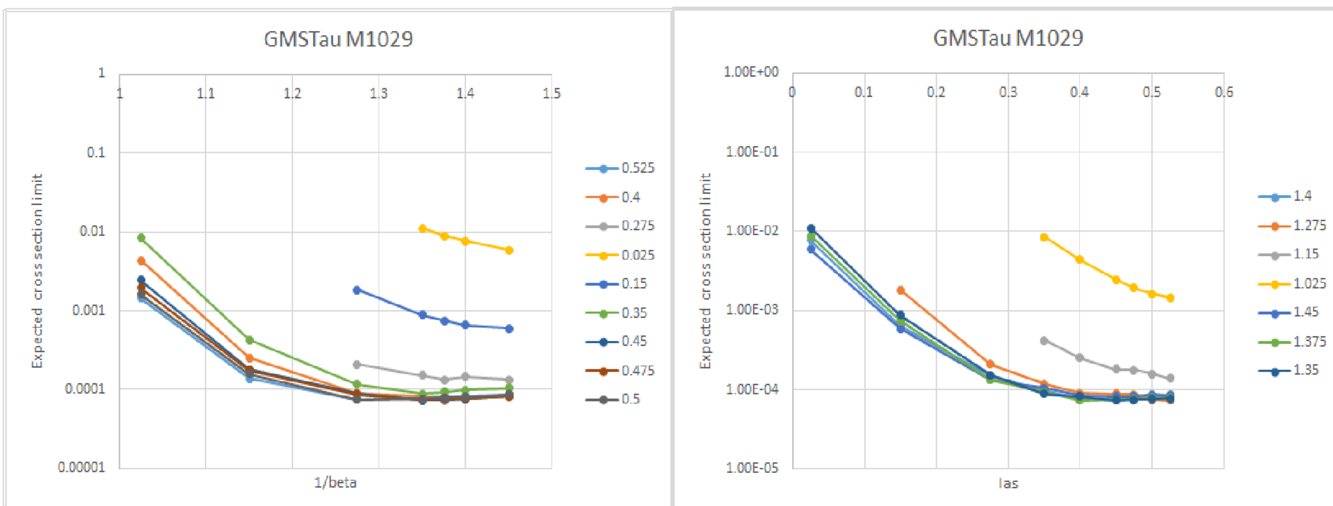


Figure 26: The plot on the left shows the expected cross section limits versus produced by different cuts of $\frac{1}{\beta}$ with the different lines corresponding to different values of $I_{as}$. The plot on the right shows the expected cross section at different $\frac{1}{\beta}$ with the different lines corresponding to different values of $I_{as}$ both for a GMStau signal with mass of 1029 $GeV/c^2$.

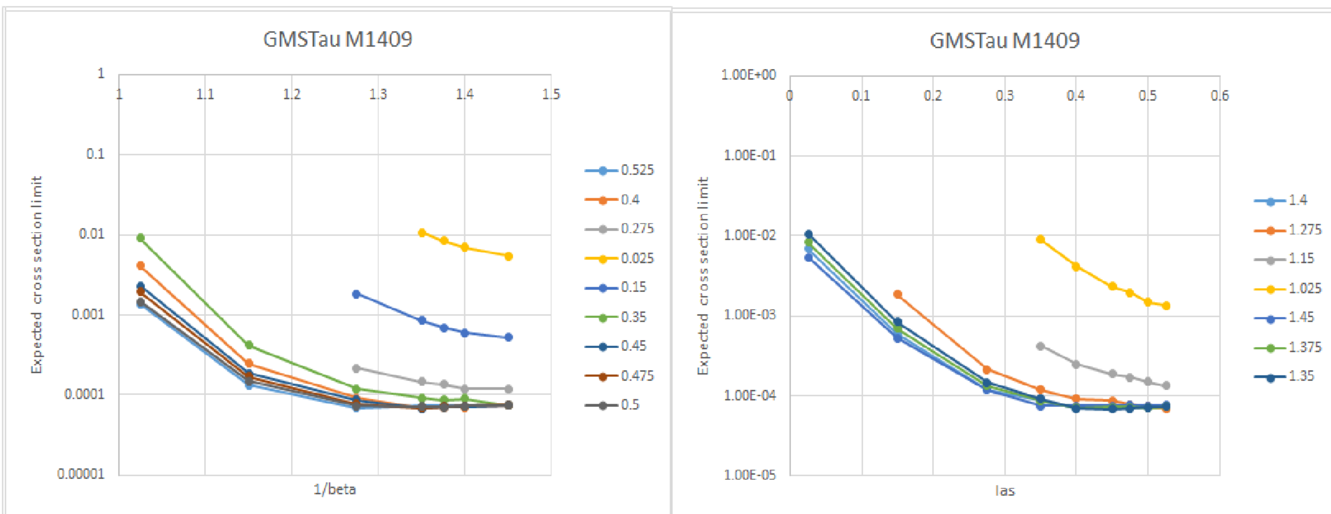


Figure 27: The plot on the left shows the expected cross section limits versus produced by different cuts of $\frac{1}{\beta}$ with the different lines corresponding to different values of $I_{as}$. The plot on the right shows the expected cross section at different $\frac{1}{\beta}$ with the different lines corresponding to different values of $I_{as}$ both for a GMStau signal with mass of 1409 $GeV/c^2$.

## B.3 Gluino plots

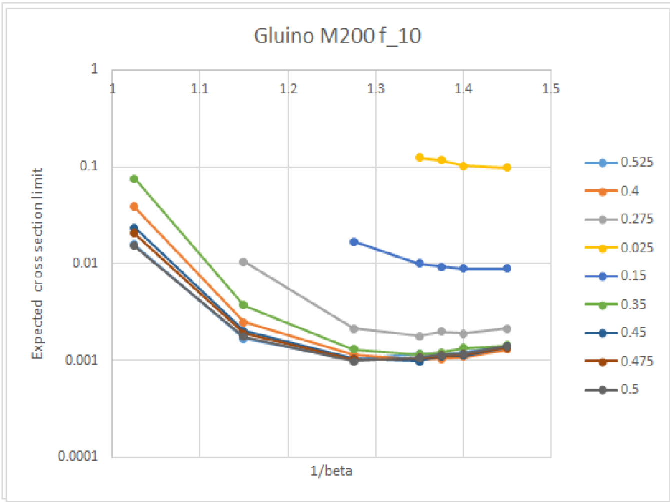


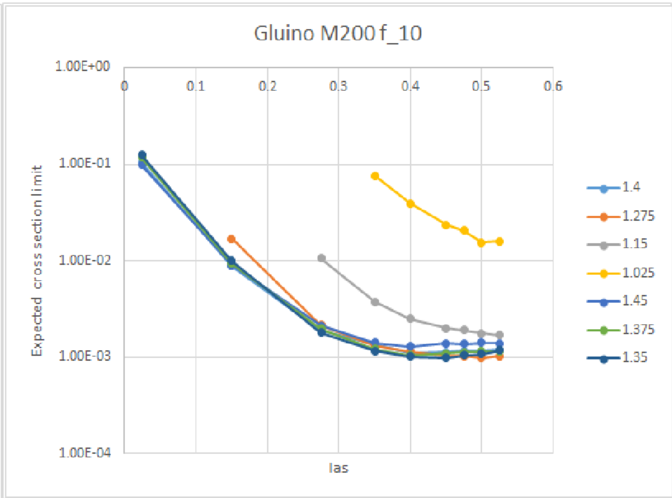


Figure 28: The plot on the left shows the expected cross section limits versus produced by different cuts of $\frac{1}{\beta}$ with the different lines corresponding to different values of $I_{as}$. The plot on the right shows the expected cross section at different $\frac{1}{\beta}$ with the different lines corresponding to different values of $I_{as}$ both for a gluino signal with mass of 200 $GeV/c^2$ and a mass ratio of ten percent.

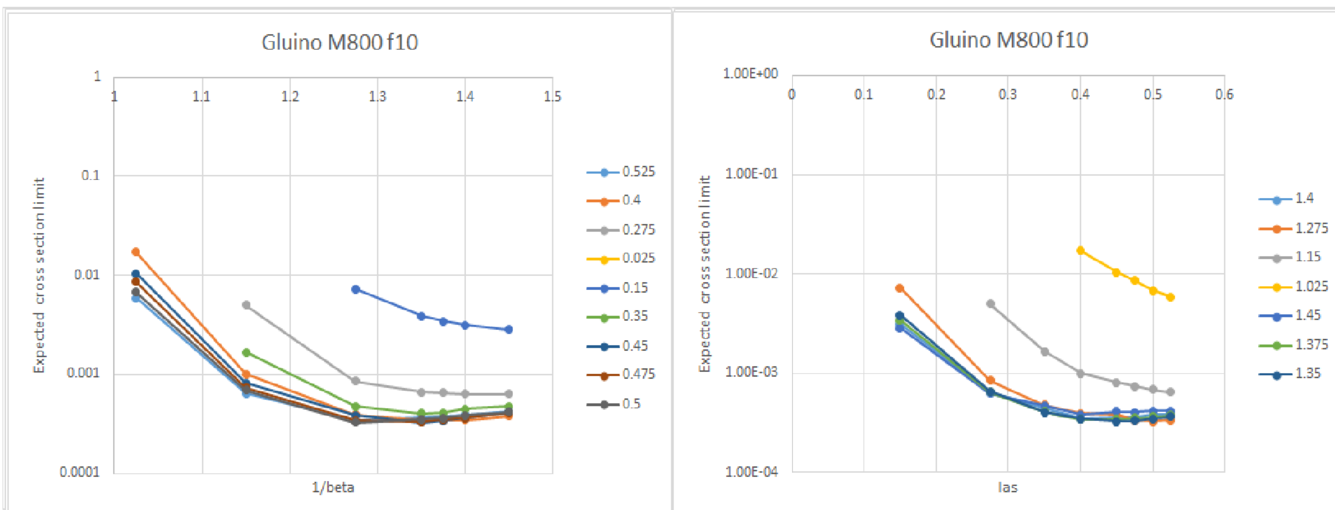


Figure 29: The plot on the left shows the expected cross section limits versus produced by different cuts of $\frac{1}{\beta}$ with the different lines corresponding to different values of $I_{as}$. The plot on the right shows the expected cross section at different $\frac{1}{\beta}$ with the different lines corresponding to different values of $I_{as}$ both for a gluino signal with mass of 800 $GeV/c^2$ and a mass ratio of ten percent.

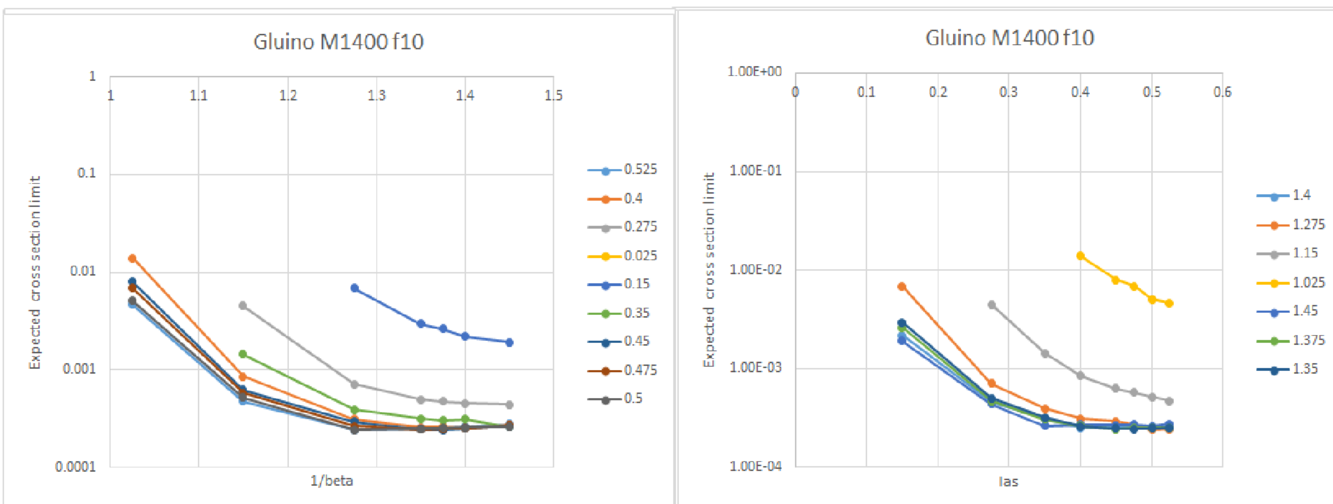


Figure 30: The plot on the left shows the expected cross section limits versus produced by different cuts of $\frac{1}{\beta}$ with the different lines corresponding to different values of $I_{as}$. The plot on the right shows the expected cross section at different $\frac{1}{\beta}$ with the different lines corresponding to different values of $I_{as}$ both for a gluino signal with mass of 1400 $GeV/c^2$ and a mass ratio of ten percent.

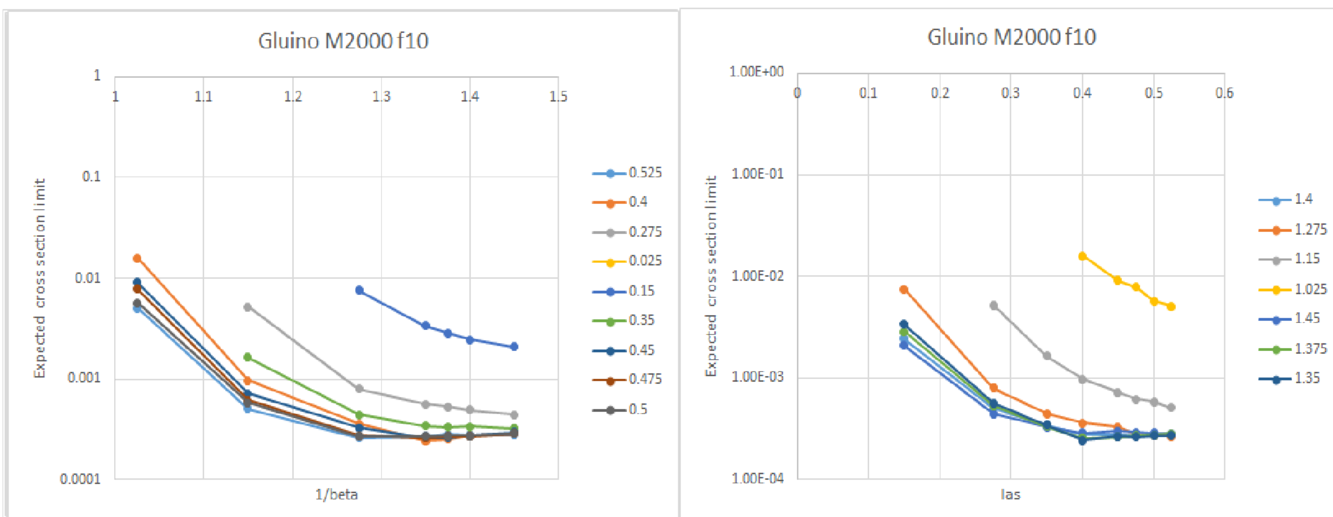


Figure 31: The plot on the left shows the expected cross section limits versus produced by different cuts of $\frac{1}{\beta}$ with the different lines corresponding to different values of $I_{as}$. The plot on the right shows the expected cross section at different $\frac{1}{\beta}$ with the different lines corresponding to different values of $I_{as}$ both for a gluino signal with mass of 2000 $GeV/c^2$ and a mass ratio of ten percent.

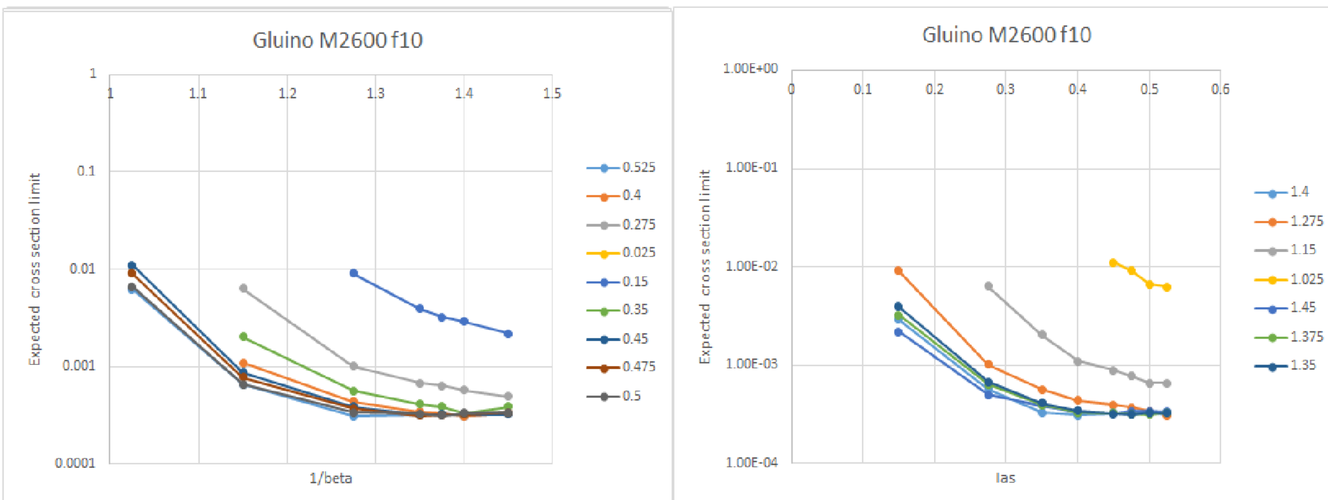


Figure 32: The plot on the left shows the expected cross section limits versus produced by different cuts of $\frac{1}{\beta}$ with the different lines corresponding to different values of $I_{as}$. The plot on the right shows the expected cross section at different $\frac{1}{\beta}$ with the different lines corresponding to different values of $I_{as}$ both for a gluino signal with mass of 2600 $GeV/c^2$ and a mass ratio of ten percent.

## B.4 PPStau

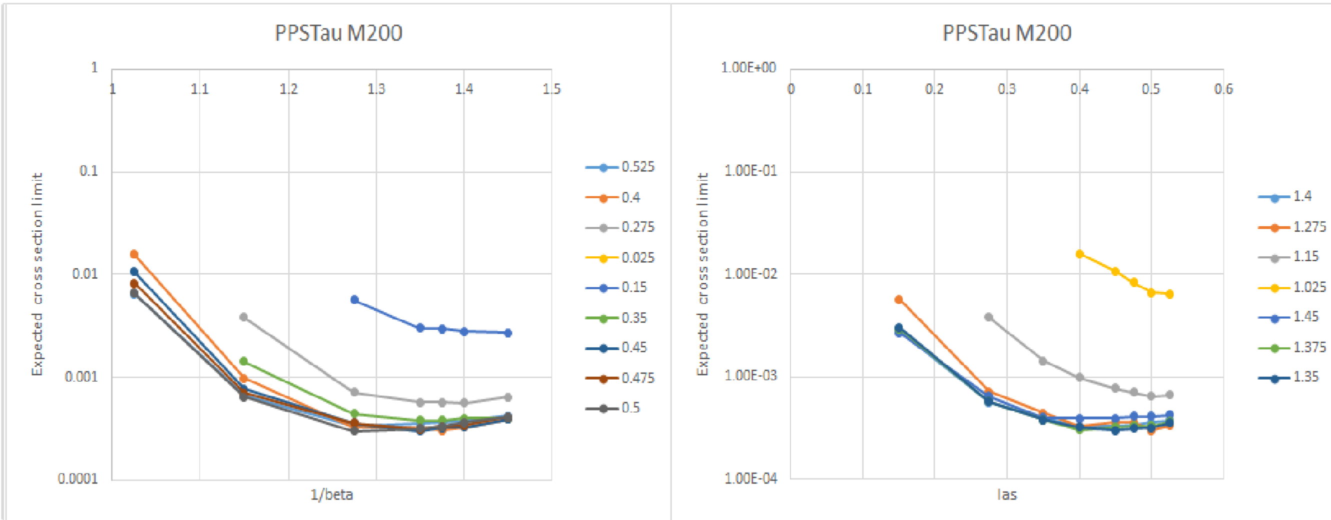


Figure 33: The plot on the left shows the expected cross section limits versus produced by different cuts of $\frac{1}{\beta}$ with the different lines corresponding to different values of $I_{as}$. The plot on the right shows the expected cross section at different $\frac{1}{\beta}$ with the different lines corresponding to different values of $I_{as}$ both for a PPStau signal with mass of 200 $GeV/c^2$.

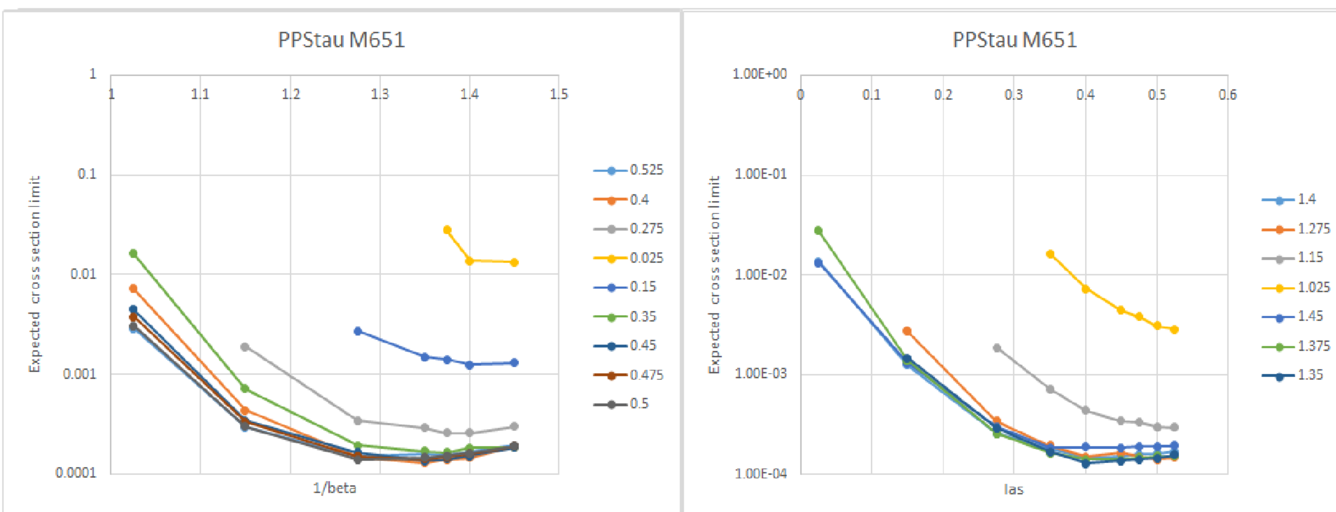


Figure 34: The plot on the left shows the expected cross section limits versus produced by different cuts of $\frac{1}{\beta}$ with the different lines corresponding to different values of $I_{as}$. The plot on the right shows the expected cross section at different $\frac{1}{\beta}$ with the different lines corresponding to different values of $I_{as}$ both for a PPStau signal with mass of 651 $GeV/c^2$.

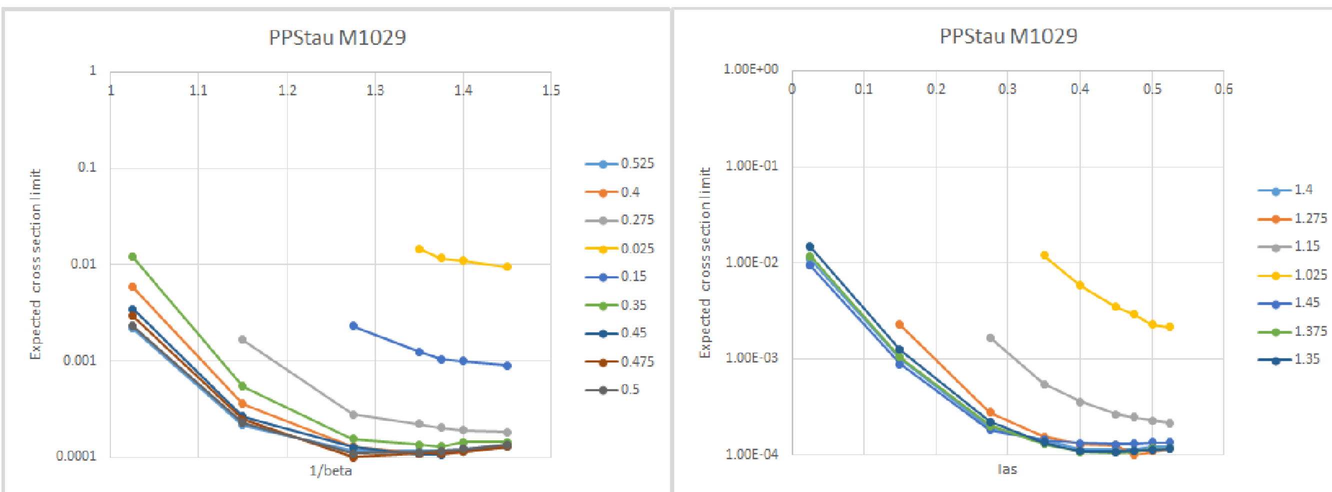


Figure 35: The plot on the left shows the expected cross section limits versus produced by different cuts of $\frac{1}{\beta}$ with the different lines corresponding to different values of $I_{as}$. The plot on the right shows the expected cross section at different $\frac{1}{\beta}$ with the different lines corresponding to different values of $I_{as}$ both for a PPStau signal with mass of 1029 $GeV/c^2$.

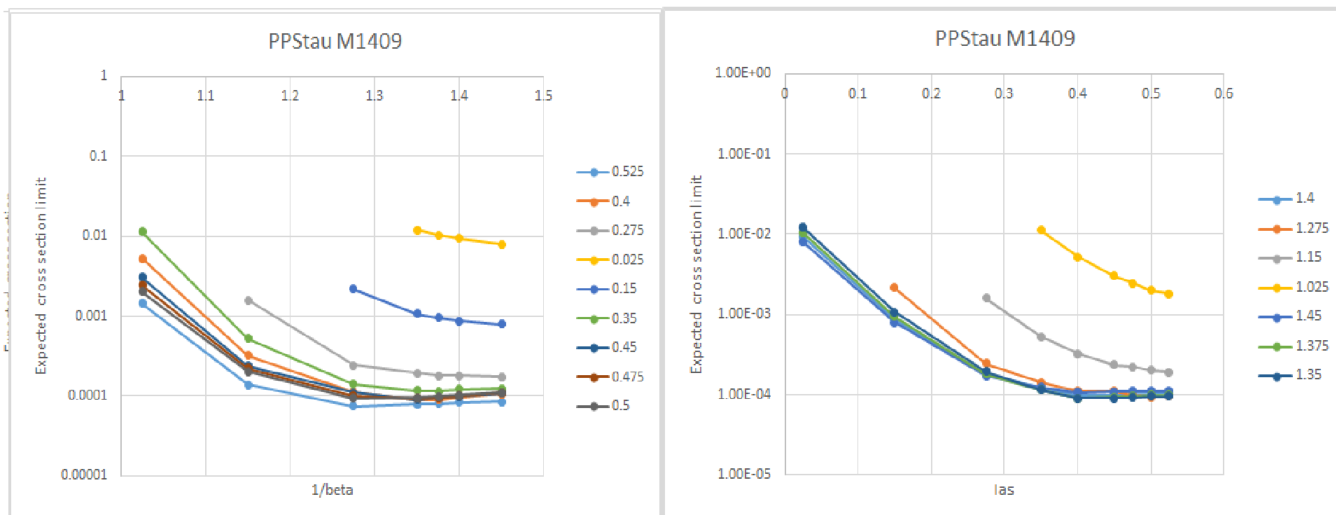


Figure 36: The plot on the left shows the expected cross section limits versus produced by different cuts of $\frac{1}{\beta}$ with the different lines corresponding to different values of $I_{as}$. The plot on the right shows the expected cross section at different $\frac{1}{\beta}$ with the different lines corresponding to different values of $I_{as}$ both for a PPStau signal with mass of 1409 $GeV/c^2$.

## B.5 Stop Plots

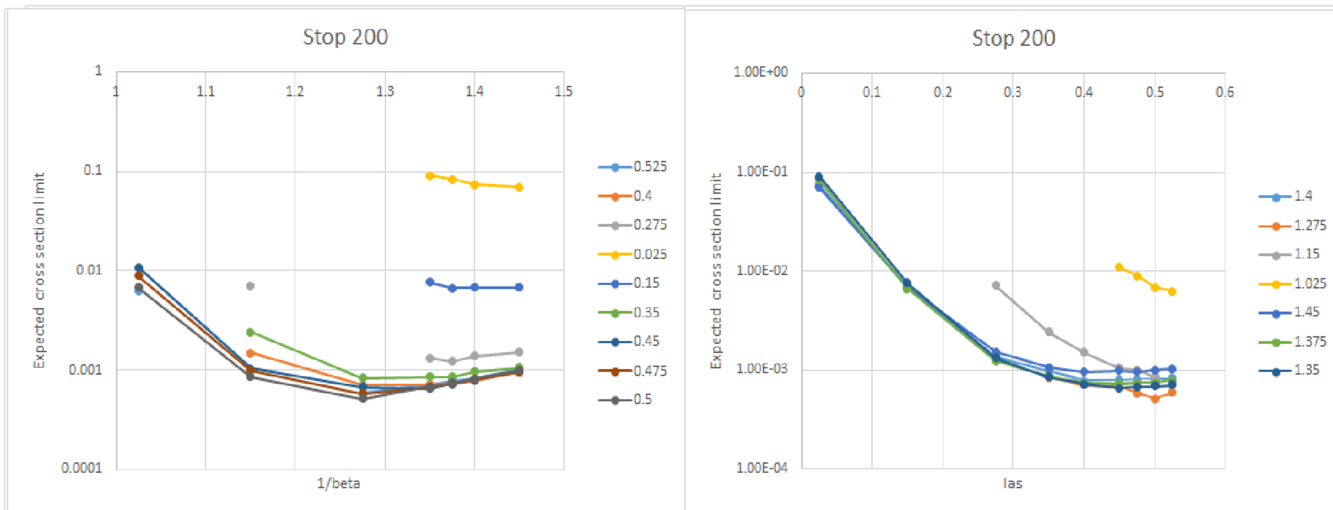


Figure 37: The plot on the left shows the expected cross section limits versus produced by different cuts of $\frac{1}{\beta}$ with the different lines corresponding to different values of $I_{as}$. The plot on the right shows the expected cross section at different $\frac{1}{\beta}$ with the different lines corresponding to different values of $I_{as}$ both for a Stop signal with mass of 200 $GeV/c^2$.

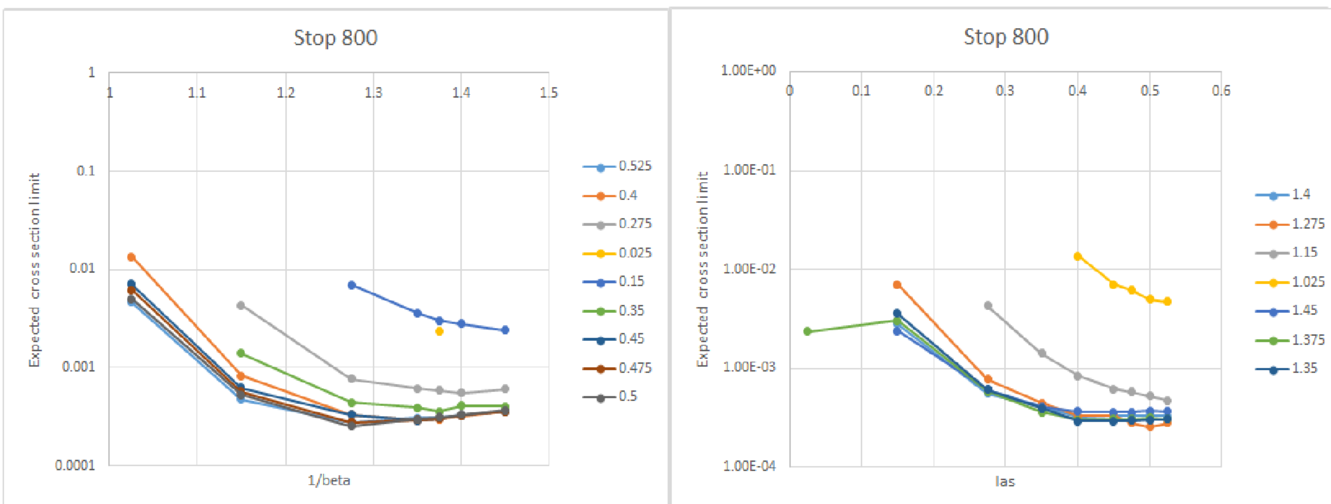


Figure 38: The plot on the left shows the expected cross section limits versus produced by different cuts of $\frac{1}{\beta}$ with the different lines corresponding to different values of $I_{as}$. The plot on the right shows the expected cross section at different $\frac{1}{\beta}$ with the different lines corresponding to different values of $I_{as}$ both for a Stop signal with mass of 800 $GeV/c^2$.

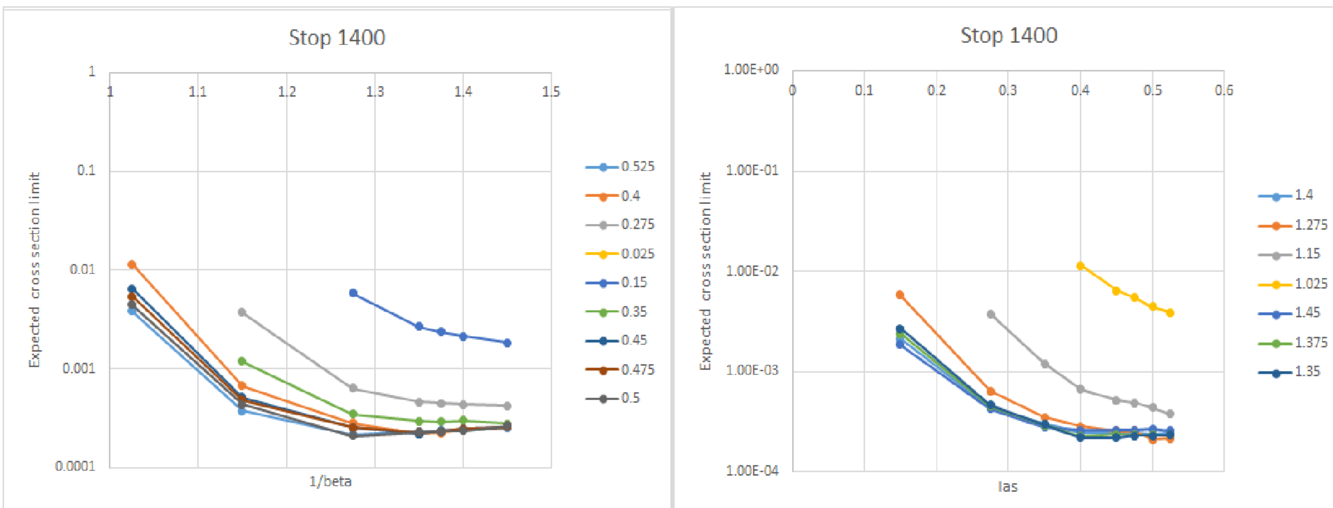


Figure 39: The plot on the left shows the expected cross section limits versus produced by different cuts of $\frac{1}{\beta}$ with the different lines corresponding to different values of $I_{as}$. The plot on the right shows the expected cross section at different $\frac{1}{\beta}$ with the different lines corresponding to different values of $I_{as}$ both for a Stop signal with mass of 1400 $GeV/c^2$.

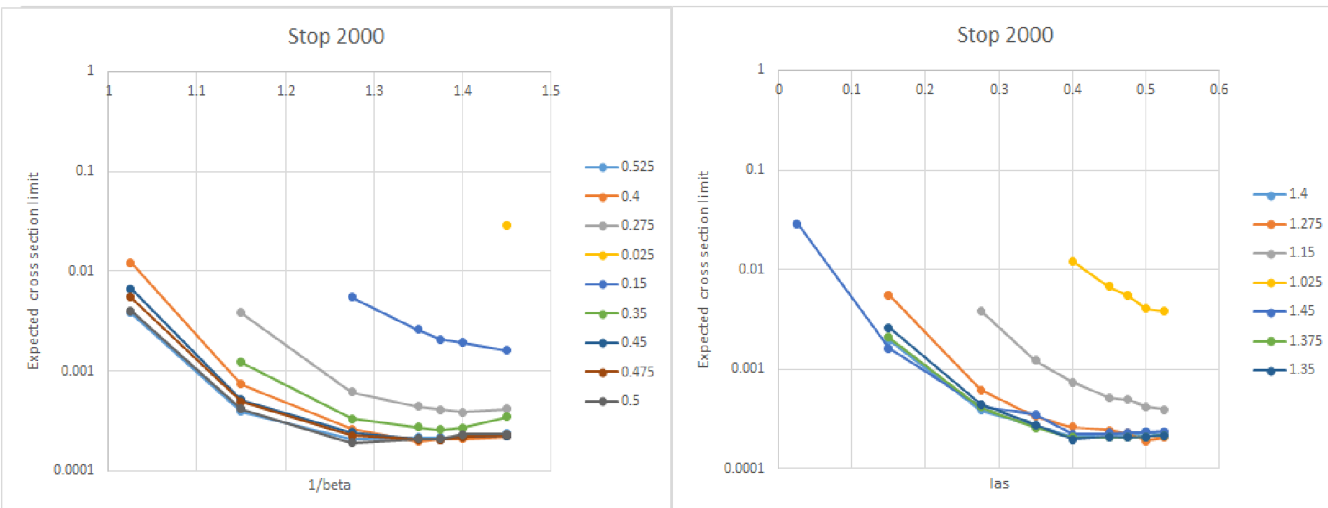


Figure 40: The plot on the left shows the expected cross section limits versus produced by different cuts of $\frac{1}{\beta}$ with the different lines corresponding to different values of $I_{as}$. The plot on the right shows the expected cross section at different $\frac{1}{\beta}$ with the different lines corresponding to different values of $I_{as}$ both for a Stop signal with mass of 2000 $GeV/c^2$.

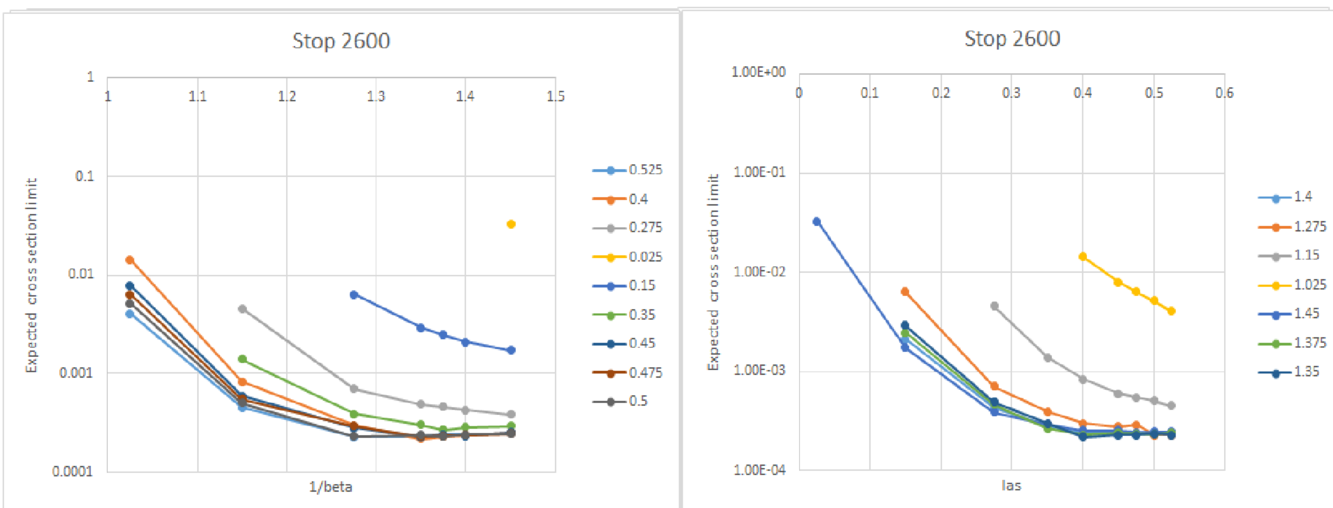


Figure 41: The plot on the left shows the expected cross section limits versus produced by different cuts of $\frac{1}{\beta}$ with the different lines corresponding to different values of $I_{as}$. The plot on the right shows the expected cross section at different $\frac{1}{\beta}$ with the different lines corresponding to different values of $I_{as}$ both for a Stop signal with mass of 2600 $GeV/c^2$.

# C Bibliography

## References

[1] Lee Buescher. Atomic structure timeline. URL: https://atomictimeline.net/

[2] Pauline ‘ Gagnon. The standard model: a beautiful but flawed theory. URL: https://www.quantumdiaries.org/2014/03/14/the-standard-model-a-beautiful-but-flawed-theory/

[3] Rabindra N. Mohapatra. Supersymmetry and R-parity: an overview, 2015.

[4] Philippe Mermod, George Alverson, Pran Nath, and Brent Nelson. Discovery potential of r-hadrons with the ATLAS detector at the LHC. 2010.

[5] Sidney R. Coleman. Q Balls. *Nucl. Phys. B*, 262:263, 1985. [Erratum: Nucl.Phys.B 269, 744 (1986)].

[6] CMS collaboration. Search for supersymmetry in the multijet and missing transverse momentum final state in pp collisions at 13 TeV. 2016.

[7] LHC Machine. *JINST*, 3:S08001, 2008.

[8] Esma Mobs. The CERN accelerator complex. Complexe des accélérateurs du CERN. Jul 2016. General Photo.

[9] Maryam Zeinali, Jorgen DHondt, and Mansour Haghighat. Measurement of the jet energy scale in the CMS experiment with the first LHC proton collisions. presented September 2011

[10] CMS Collaboration, CMS Warsaw, Krzysztof Pozniak, G.Kasprowicz, Ryszard Romaniuk, and Wojciech Zabolotny. Boson with a mass of 125 GeV observed in the CMS. *Science*, 338:1569–1575, 12 2012.

[11] Cheuk-Yin Wong. *Introduction to High-Energy Heavy-Ion Collisions*. WORLD SCIENTIFIC, 1994.

[12] Artur Kalinowski and Jan Krolikowski. Search for the heavy, neutral mssm higgs particles in the $h/a- > \tau\tau- > \mu + x$ channel in the CMS detector at the LHC. 04 2020.

[13] Pisana Placidi. Alignment of the CMS tracker with LHC and cosmic ray data. *Journal of Instrumentation*, 9:1–55, 06 2014.

[14] Silicon strips. URL: https://CMS.cern/detector/identifying-tracks/silicon-strips.

[15] A. Giammanco. Particle identification with energy loss in the CMS silicon strip tracker. 6 2007.

[16] Manfred Krammer. The silicon sensors for the Inner Tracker of the Compact Muon Solenoid experiment. *Nucl. Instrum. Methods Phys. Res., A*, 531:238–245, 2004.

[17] Erik Butz. *Calibration, alignment and long-term performance of the CMS silicon tracking detector*. PhD thesis, Hamburg U., 2009.

[18] CMS Collaboration. The CMS experiment at the CERN LHC. The Compact Muon Solenoid experiment. *JINST*, 3:S08004. 361 p, 2008. Also published by CERN Geneva in 2010.

[19] CMS Collaboration. The Phase-2 Upgrade of the CMS Tracker. Technical Report CERN-LHCC-2017-009. CMS-TDR-014, CERN, Geneva, Jun 2017.

[20] *The CMS hadron calorimeter project: Technical Design Report*. Technical Design Report CMS. CERN, Geneva, 1997.

[21] CMS collaboration *The CMS muon project: Technical Design Report*. Technical Design Report CMS. CERN, Geneva, 1997.

[22] Supratik Mukhopadhyay. Studies on the upgrade of the muon system in the forward region of the CMS experiment at LHC with gems. *Journal of Instrumentation*, 9, 01 2014.

[23] Et Collaboration, Krzysztof Pozniak, Ryszard Romaniuk, and Wojciech Zabolotny. Calibration of the CMS drift tube chambers and measurement of the drift velocity with cosmic rays. *Journal of Instrumentation*, 5:1–39, 03 2009.

[24] Frederick James. *Statistical Methods in Experimental Physics*. WORLD SCIENTIFIC, 2nd edition, 2006.

[25] Venkatesh Veeraraghavan. Search for multiply charged Heavy Stable Charged Particles in data collected with the CMS detector., 2013. presented December 2013.

[26] Loïc Quertenmont. Search for Heavy Stable Charged Particles with the CMS detector at the LHC, 2010. presented Oct 2010.

[27] J. Beringer et al. Review of Particle Physics (RPP). *Phys. Rev. D*, 86:010001, 2012.

[28] M. Drees and X. Tata. Signals for heavy exotics at hadron colliders and supercolliders. *Physics Letters B*, 252:695–702, 12 1990.

[29] The CMS collaboration. Performance of CMS muon reconstruction in pp collision events at $\sqrt{s} = 7$ TeV. *Journal of Instrumentation*, 7(10):P10002–P10002, oct 2012. ds.

[30] Pythia 6.4 physics and manual. *Journal of High Energy Physics*, 2006(05):026–026, May 2006. Jan 2008.

[31] S. Agostinelli et al. GEANT4: A simulation toolkit". *Nucl. Instrum. Meth.* A506 (2003), pp. 250-303. DOI: 10.1016/S0168-9002(03)01368

[32] Austin Skeeters A Search for Multi-Charged Heavy Stable Particles at $\sqrt{s}$=13 TeV, 2016 presented April 2016

[33] Han, Jiyeon The Differential cross section distribution of Drell-Yan dielectron pairs in the z boson mass region DOI: 10.2172/945409 Jan (2008)